Petrophysical Studies on Woodford Shale in Oklahoma and Wolfcamp Shale in Texas: A Multiple-Approach Methodology

By

CHEN ZHAO

Presented to the Faculty of the Graduate School of

The University of Texas at Arlington in Partial Fulfillment

of the Requirements

for the Degree of

DOCTOR OF PHILOSOPHY

THE UNIVERSITY OF TEXAS AT ARLINGTON

MAY 2022

Supervising Committee:

Qinhong Hu, Ph.D. Supervising Professor
John S. Wickham, Ph.D.
Majie Fan, Ph.D.
Jiechao Jiang, Ph.D.
Erika La Plante, Ph.D.

Abstract

Petrophysical Studies on Woodford Shale in Oklahoma and Wolfcamp Shale in Texas: A Multiple-Approach Methodology

Chen Zhao, Ph.D

The University of Texas at Arlington, 2022

Supervising Professor: Qinhong Hu

The successful development of oil and gas from unconventional reservoirs in the United States proves the high petroleum potential that shale rock reserves. Petrophysical studies on shale rocks are an important part of reservoir characterization. Petrophysical studies investigate the basic properties and pore structures of the shale rock, including porosity, density, pore size distribution, specific surface area, wettability, pore connectivity, and permeability, to understand the storage and movement of oil and gas in shale rocks. Multiple experimental approaches were applied onto both outcrop and well-core samples from several U.S. shale plays. A range of complementary methodologies of X-ray diffraction, polarized optical microscopy, mercury intrusion porosimetry, gas physisorption, small-angle X-ray scattering, liquid immersion porosimetry, scanning electronic microscopy, and tracer gas diffusion were designed to measure the basic properties and pore structure of these shale samples. This Ph.D. dissertation is divided into three chapters for three different but coherent projects: 1) The first one is by applying multiple approaches mentioned above on Woodford Shale outcrop samples to study the limitations of each approach and find a good combination for pore structure studies; the fluid-rock interactions and pore structures

were also investigated in this project; 2) The second one is by using mercury intrusion porosimetry, gas physisorption, small angle X-ray scattering, scanning electronic microscopy, and spontaneous imbibition to study the effects of sedimentary features and mineralogy on pore structure and fluid-rock interaction of Wolfcamp Shale core samples; and 3) The third is to measure the porosity of granular rock samples by using a modified bulk density method for obtaining size-dependent effective porosity in conjunction with particle density analyses. In summary, this dissertation aims to understand and assess the limitations of laboratory experimental approaches, the effect of mineralogy on pore structure, and fluid-rock interaction on shale.

ACKNOWLEDGEMENTS

I would like to thank my advisor, Dr. Qinhong Hu, for his patience and support in my graduate program so I can have the opportunity to continue my study in geology. Because of him, I was able to gain experimental experience, get access to many resources, and succussed in my research. I greatly appreciate the help and assistance of all other committee members Drs. Wickham, Fan, Jiang, and La Plante. I am indebted to Dr. Jiang for the help in his Center that helped me execute my experiments in the best way, and I am grateful to Dr. Fan for providing me invaluable rock samples.

I would like to acknowledge all my professors at the University of Texas at Arlington for instructing me and helping me in many ways. I am very grateful to all my colleagues and visiting scholars in the department, and it was my pleasure to work with them. I would also like to thank my beloved ones, Fengxiang Hou and Qiming Wang, for being the light in my life.

TABLE OF CONTENT

LIST OF FIGURES

Chapter II

Chapter III

Chapter IV

LIST OF TABLES

Chapter II

Chapter III

Chapter IV

Chapter I: Introduction

Because of the increasing production of hydrocarbons in unconventional shale and the focus on carbon capture, utilization, and storage which use shale as caprock, more and more researchers focus on the pore structures of shale rock (Ameen, 2022). Pore structure characterization could help understand the petroleum storage and movement mechanisms (Ross and Bustin, 2009; Cao et al., 2015; Liu and Ostadhassan, 2019). The low porosity and extremely low permeability of shale make the characterization of its pore structure difficult with fine-grained matrix composition. Lots of laboratory experiments have been developed to probe the shale pore structure, including porosity, pore size distribution, specific surface area, wettability, and permeability (Parker et al., 2009; Chalmers et al., 2012; Wang et al., 2016; Gao and Hu, 2018). Every experiment operates on different principles and could only test different parts of pore structures, and no single approach could thoroughly investigate the pore structures for a wide pore spectrum of nm-μm in diameters. Meanwhile, nano-sized pores and complex properties in shale pores increase the difficulties of the characterization. Therefore, a combination of multiple approaches is necessary to obtain a comprehensive characterization of pore structure for shale.

The commonly applied laboratory experiments can be separated into four categories: fluid immersion approach, radioactive approach, visualization approach, and fluid flow approach. The fluid immersion approach uses fluids to intrude into pores to indirectly measure the pores that are connected to the sample surface, including liquid immersion porosimetry (LIP), mercury intrusion porosimetry (MIP), and gas physisorption (GP) (Flint and Flint, 2002; Labani et al., 2013; Kuila et al., 2014; Hu, 2018). The radiation approach uses X-rays and neutron to scan the porous media to obtain the pore structure data (both isolated and connected pores), including small-

angle X-ray scattering and small-angle neutron scattering (Barre, 2016; Anovitz and Cole, 2018; Peng et al., 2020). The visualization approach uses different microscopies, such as polarized microscopy and scanning electronic microscope (SEM), to investigate the pores visually (Slatt and O'Brien, 2011; Jiang et al., 2016; Sui et al., 2018). The fluid flow approach uses dynamic monitoring to test the fluid-rock interaction, including spontaneous imbibition and tracer gas diffusion (Hu and Wang, 2001; Peng et al., 2012; Gao and Hu, 2018). Most researchers choose one or two approaches to test the shale samples, but seldomly apply many complementary approaches and discuss the difference in the pore structures characterized by each approach.

The choice of experimental approaches is not the only factor that could affect the pore structure characterization, so do the sample dimensions. Sample dimensions could be very different in each approach. For example, 1-cm^3 cubes with a side length of 1 cm are commonly used for MIP (though it can accommodate the sample sizes from μm-sized grains to 1-in plugs), 1-inch diameter core plugs in different heights for LIP and tracer gas diffusion, and granular samples with diameters between 500-840 μm for GP. These different dimensions of samples could be generated from large-sized chunks, and thus the sample size reduction process could potentially cause property changes, such as effective porosity. Data on coal and shale samples prove the changes in porosity for different granular samples (Davudov and Moghanloo, 2016; Chen et al., 2018). However, existing experiment methods could seldomly and efficiently measure porosity on granular samples with diameters smaller than 800 μm. A modified bulk density approach was worked out in this dissertation to measure porosities for granular samples.

Porosity could be calculated from bulk density and particle density by the equation: porosity =1- $\frac{\rho_{bulk}}{\rho_{particle}}$. Particle density could be measured by helium

pycnometry with a wide range of sample dimensions from 10s μm to 10 cm. We used a modified GeoPyc 1365 bulk density approach for bulk density measurement. GeoPyc 1365 uses uncompressible silicon spheres to cover the granular samples and uses volumes different before and after the sample compaction to calculate the bulk volume. By combing with the sample weight, the bulk density could be calculated and used in porosity calculation (Forsmo, 2005; Zhao et al., 2021).

Using multiple experimental approaches for different shale samples, this dissertation aims to: 1) compare the application of different approaches for petrophysical characterization; 2) study the pore structure and find the effect of sedimentary and mineralogical features on pore structure; and 3) characterize the heterogeinity of shale rocks with complementary and integrated approaches. Chapter II uses three laboratory approaches to test the Woodford Shale outcrop samples to compare the pros and cons of each approach and find a good experimental combination. Pore structure and mineralogy effects of the Woodford Shale were also characterized and synthesized in Chapter II. Chapter III provides a case study of pore structure characterization and fluid-rock interaction of Wolfcamp Shale core samples. Chapter IV presents a modified method of porosity measurement for a wide range of sample sizes, especially grains smaller than 800 μm in diameters by using the bulk density approach, for several natural rocks including shale.

Reference:

Ameen, N. (2022, February 17). U.S. Energy Information Administration [Webinar]. https://www.eia.gov/todayinenergy/detail.php?id=51319

Anovitz, L. M., & Cole, D. R. (2018). Analysis of the pore structures of shale using neutron and X - ray small angle scattering. Geological Carbon Storage: Subsurface Seals and Caprock Integrity, 71-118.

Barré, L. (2016). Contribution of small-angle x-ray and neutron scattering (saxs and sans) to the characterization of natural nanomaterials. In X-ray and Neutron Techniques for Nanomaterials Characterization (pp. 665-716). Springer, Berlin, Heidelberg.

Chen, Y., Qin, Y., Wei, C., Huang, L., Shi, Q., Wu, C., & Zhang, X. (2018). Porosity

changes in progressively pulverized anthracite subsamples: Implications for the study of closed pore distribution in coals. Fuel, 225, 612-622.

Cao, T., Song, Z., Wang, S., & Xia, J. (2015). A comparative study of the specific surface area and pore structure of different shales and their kerogens. Science China Earth Sciences, 58(4), 510-522.

Chalmers, G. R., Bustin, R. M., & Power, I. M. (2012). Characterization of gas shale pore systems by porosimetry, pycnometry, surface area, and field emission scanning electron microscopy/transmission electron microscopy image analyses: Examples from the Barnett, Woodford, Haynesville, Marcellus, and Doig units Characterization of Gas Shale Pore Systems. AAPG Bulletin, 96(6), 1099-1119.

Davudov, D., Moghanloo, R. G. (2016). Upscaling of pore connectivity results from lab-scale to well-scale for Barnett and Haynesville Shale Plays. In SPE Annual Technical Conference and Exhibition. Society of Petroleum Engineers.

Flint, A. L., Flint, L. E. (2002). Particle Density. Methods of Soil Analysis: Part 4 Physical Methods, 5, 229-240, Soil Science Society of America, Madison, WI.

Forsmo, S. P. E., & Vuori, J. P. (2005). The determination of porosity in iron ore green pellets by packing in silica sand. Powder Technology, 159(2), 71-77.

Gao, Z., & Hu, Q. (2018). Pore structure and spontaneous imbibition characteristics of marine and continental shales in China. AAPG Bulletin, 102(10), 1941-1961.

Hu, M. Q., Persoff, P., & Wang, J. S. (2001). Laboratory measurement of water imbibition into low-permeability welded tuff. Journal of Hydrology, 242(1-2), 64-78.

Hu, Q. (2018). Quantifying effective porosity of oil and gas reservoirs. In 2018 AAPG International Conference and Exhibition. AAPG Search and Discovery Article #70376, 5 pages. DOI:10.1306/70376Hu2018.

Jiang, W., Lin, M., Yi, Z., Li, H., & Wu, S. (2017). Parameter determination using 3D FIB-SEM images for development of effective model of shale gas flow in nanoscale pore clusters. Transport in Porous Media, 117(1), 5-25.

Kuila, U., McCarty, D. K., Derkowski, A., Fischer, T. B., & Prasad, M. (2014). Total porosity measurement in gas shales by the water immersion porosimetry (WIP) method. Fuel, 117, 1115-1129.

Labani, M. M., Rezaee, R., Saeedi, A., & Al Hinai, A. (2013). Evaluation of pore size spectrum of gas shale reservoirs using low pressure nitrogen adsorption, gas expansion and mercury porosimetry: A case study from the Perth and Canning Basins, Western Australia. Journal of Petroleum Science and Engineering, 112, 7-16.

Liu, K., & Ostadhassan, M. (2019). The impact of pore size distribution data presentation format on pore structure interpretation of shales. Advances in Geo-Energy Research, 3(2), 187-197.

Peng, S., Hu, Q., & Hamamoto, S. (2012). Diffusivity of rocks: Gas diffusion measurements and correlation to porosity and pore size distribution. Water Resources Research, 48(2).

Peng, L., Chen, B., & Zhao, Y. (2020). Quantitative characterization and comparsion of bentonite microstructure by small angle X-ray scattering and nitrogen adsorption. Construction and Building Materials, 262, 120863.

Slatt, R. M., & O'Brien, N. R. (2011). Pore types in the Barnett and Woodford gas shales: Contribution to understanding gas storage and migration pathways in fine-grained rocks. AAPG Bulletin, 95(12), 2017-2030.

Sui, W., Tian, Y., & Yao, C., (2018). Investigation of microscopic pore structure

variations of shale due to hydration effects through SEM fixed-point observation experiments. Petroleum Exploration and Development, 45(5), 955-962.

Zhao, C., Zhou, W., Hu, Q. H., Xu, H., & Zhang, C. (2021). Porosity measurement of granular rock samples by modified bulk density analyses with particle envelopment. Marine and Petroleum Geology, 133, 105273.

Chapter II

Petrophysical studies of Woodford Shale in Oklahoma: Comparison of laboratory experiments and lithologic effects on pore systems

Chen Zhao[1], Qinhong Hu[1], Qiming Wang[1], Jing Zhang[2], Jiechao Jiang[3], and Ian Ilavsky[4]

[1]Department of Earth and Environment Sciences, The University of Texas at Arlington, 500 Yates Street, Arlington, TX, 76019, USA

[2]British Petroleum Company PLC, Houston, TX 77079, USA.

[3] Department of Materials, The University of Texas at Arlington, 500 Yates Street, Arlington, TX, 76019, USA

[4] X-ray Science Division, Advanced Photon Source, Argonne National Laboratory, Lemont, IL 60439, USA.

Abstract

Laboratory-scale pore structure characterization of unconventional reservoirs is a hot topic with the fast development of oil and gas from unconventional resources such as shale. Commonly used experiments include liquid or gas intrusion to characterize the pore systems indirectly, such as liquid immersion porosimetry (LIP), mercury intrusion porosimetry (MIP), and gas physisorption (GP). Other approaches such as radiation, visualization, and fluid flow, including small-angle X-ray scattering (SAXS), scanning electronic microscopy (SEM), and spontaneous imbibition, are also applied in a laboratory setting. These experiments have different measurement principles, measurable ranges, and data reduction assumptions and practices. In this dissertation, we take Woodford Shale outcrop samples as the object to compare the results and effects in pore structure characterization by using several of these approaches, including fluid immersion, radiation, visualization, and fluid flow. The results indicate that 1) The Woodford Shale outcrop samples are dominated by slit-shaped macropores at 0.1-1 μm in diameters; 2) mineral composition could affect the porosity; 3) weathering could partially dissolve minerals and cements; 4) mercury intrusion porosimetry, gas physisorption, and scanning electronic microscopy could be a good combination for a holistic characterization of pore structure for shale.

1. Introduction

Low porosity and extremely low permeability make the fluid flow difficult in shale formations with fine-grained matrix composition. In order to understand the fluid-matrix interaction in unconventional reservoirs, pore structure characterization of shale has been carried out in recent decades. As the key properties in reservoir characterization and fluid flow in shale, pore size distribution (PSD), pore types, and

pore connectivity are the focal points (Parker et al., 2009; Wang et al., 2016; Gao and Hu, 2018; Wang et al., 2021). The pore sizes can be divided into three categories: macropores (> 50 nm in diameters), mesopores (2-50 nm), and micropores (< 2 nm) (IUPAC, 1994). As for the pore types, most researchers have divided them into interparticle, intraparticle, and organic matter-hosted pores (Slatt and O'Brien, 2011; Milliken et al., 2013; Liu et al., 2021; Wang et al., 2021; Zheng et al., 2022).

Highly productive Barnett, Haynesville, and Horn River unconventional reservoirs have been well studied (Dong et al., 2015; Heller et al., 2014; Jarvie et al., 2007; Loucks and Ruppel, 2007; Wang et al., 2021). Late Devonian to Early Mississippian Woodford Shale is widely distributed in the Midwest USA, including west Texas, southeastern New Mexico, and southern Oklahoma (Comer, 1991; Romero and Philp, 2011). With Type II kerogen, oil- and gas-prone Woodford Shale in Oklahoma enjoys large reserves with more than 644 billion cubic feet of gas and 460 million barrels of oil (Cardott, 2005; 2017). Like most unconventional reservoirs, the low permeability and other petrophysical characteristics lead to a very fast decline of petroleum production in Woodford Shale and make economic development difficult to achieve. However, the Woodford Shale did not attract much attention, and only a few research focuses on the pore characterization by multiple methods and fluid-rock interaction experiments (Cullen et al., 2020; Ojha et al., 2018; Slatt and O'Brien, 2011; Kibria et al., 2018). In this work, we propose to investigate the pore structure and its resultant effects on fluid-rock interaction for the Woodford Shale outcrop samples collected from Oklahoma using fluid immersion, visualization, advanced radiation, and fluid flow approaches. A comparison of results from different approaches will also be conducted. The primary hypotheses are that: 1) quartz and feldspar may affect the shale porosity; and 2) the fluid properties may affect the behavior of fluid-rock interactions.

As an important unconventional source rock in Oklahoma, Woodford Shale has been examined by multiple methods, including X-ray diffraction (XRD), pyrolysis, gas physisorption (GP), mercury intrusion porosimetry (MIP), scanning electron microscopy (SEM), and small-angle scattering (SAS) in previous studies (Cardott, 2012; Cullen et al., 2020; Kibria et al., Ko et al., 2018; 2018; Slatt et al., 2011). Three pore types are identified by SEM imaging, and the interparticle pores in clay floccules form interconnected pathways (Slatt and O'Brien, 2011; Chalmer et al., 2012a; Clarkson et al., 2013). The effects of wettability and thermal maturity on Woodford Shale investigated by several researchers (Curtis et al., 2012; Hu et al., 2015; Kibria et al., 2018) concluded that the oil-wet Woodford Shale has a greater possibility to have more organic matter-hosted pores under higher thermal maturity. With a thermal treatment, Ko et al. (2017) reported that the converted hydrocarbon fluids were trapped in the pores, and the Woodford Shale has a low permeability compared with Barnett and Eagle Ford Shale.

Late Devonian-Early Mississippian Woodford Shale in Oklahoma is distributed mainly in Anadarko Basin, Arkoma Basin, Ardmore Basin, and Marietta Basin (Cardott, 2017). Our samples were collected from the outcrop in McAlister Cemetery quarry, west part of the Ardmore Basin in the south of the city Ardmore near the exit of Interstate 35 (Bernal et al., 2012; Ekwunife et al., 2017). Ardmore Basin is the consequence of compression by a series of tectonic events in Pennsylvanian to Permian (Granath, 1989). Nine samples were collected from the 100 m-thick section from the bottom to the top. Underlaying carbonate Hunton Group and overlaying Sycamore Limestone unconformably contact the Woodford Shale (Fig. 1) (Comer, 2008; Ekwunife et al., 2017). The Woodford Shale was unofficially subdivided into three units: Lower, Middle, and Upper Woodford. Lower and Middle Woodford Shale were

deposited by transgression, and the Upper Woodford Shale was formed by regression or a highstand system (Bernal et al., 2012). A total of eight samples were collected, with three samples from Middle Woodford Shale and five samples from Upper Woodford Shale. In previous studies, Woodford Shale in Ardmore Basin was defined as a quartz-rich dark-color marine shale associated with dolomite, phosphate, pyrite, and clays (Comer, 1991; Kirkland et al., 1992; Bernal et al., 2012; Cardott, 2017). Overall, the Woodford Shale has been proven an important hydrocarbon shale with Type II kerogen and high TOC values (Cardott, 2017).

Figure 1. Woodford Shale outcrop location and sampling locations (modified after Ekwunife et al., 2017).

2. Methodologies

2.1 Sample preparation and experimental methods

A total of eight samples were collected from the Woodford Shale (WFD) outcrop in McAlister Cemetery quarry, west corner of the Ardmore Basin, OK. Samples WFD-4, WFD-5, and WFD-6 were collected from Middle Woodford, WFD-7, WFD-8, WFD-9, WFD-11, and WFD-328 from the Upper Woodford (Fig. 1). No samples come from Lower Woodford because the rocks in Lower Woodford are fragile and hard to collect. Samples were processed into various dimensions for different laboratory experiments. For total organic carbon (TOC) & X-ray diffraction (XRD) analyses,

samples were milled into powders (<75 μm) by SPEX SamplePrep 8000M for 5 minutes. Cubic samples at a side length of 1 cm were the sample dimensions for MIP and spontaneous imbibition (SI).

Additionally for SI experiments, four sides of the cubes were coated with epoxy, and only the top and the bottom surfaces that contact with the fluid were open. Gas physisorption (GP) uses crushed samples with granular diameters between 500-840 μm. For SEM and contact angle analyses, polished slabs (~1 cm across and 0.3 cm in thickness) with parallel top and bottom surfaces were applied. The slabs for SEM imaging were polished by sandpapers with grid of 400, 800, 1200, 2400, and 3000 in sequence. Samples for (ultra) small-angle X-ray scattering [(U)SAXS] were of thin slabs in shape at 1 cm across and a thickness of ~0.8 mm measured for data reduction. Before all these experiments, samples were oven-dried at 60°C for 48 hours to remove the moisture in the connected pore space.

2.2 Basic Properties

2.2.1 XRD & pyrolysis

Mineral weight percentage measurements were performed by Shimadzu MAXima X XRD-7000 X-ray Diffractometer with the 2θ from 2° to 70°. The mineralogical compositions were calculated in weight percent with the uncertainty of ±10% approximately (Moore and Reynolds, 1989). Organic content and thermal maturity were conducted by GeoMark Research Ltd with Leco TOC and HAWK pyrolysis & TOC instruments. Total organic carbon, calculated R_o%, T_{max}, and other geochemical data were obtained and calculated from these measurements (Lewan et al., 2017; Gorynski et al., 2017).

2.2.2 Contact angle

When a drop of water falls on a flat rock surface, the water drop will spread or bead up due to the interfacial tension. The angle between the rock surface and the tangent line at the three-phase point (water-air-rock) is the contact angle (θ). Contact angle can be used to assess the wettability of a shale rock (Craig, 1971). Cosθ >0 means the rock is water wet; cosθ =0 means the rock is neutrally wet; and cosθ <0 means the rock is oil wet (Tiab, 2015). Deionized water (DIW) was applied as the fluid, and pictures were taken by Dino-Lite USB microscope camera. Contact angle was obtained from captured images by the software package of Drop Shale Analysis carried in ImageJ with an uncertainty of ±2° (Stalder et al., 2006; 2010; Extrand, 2016).

2.3 Fluid Immersion Approach

2.3.1 Liquid Immersion Porosimetry (LIP)

LIP is carried out after vacuum pulling to evacuate the air from connected pore space followed with an introduction of a liquid to ensure a full liquid saturation of samples. Samples were vacuumed under a pressure of 0.1 Torr for over 12 hours, after that samples were flushed with CO_2 for 30 min. The aim of CO_2 injection is to use CO_2 to replace the residual air to improve the water saturation since CO_2 is much easier to be dissolved in water than residual air in the pore space. Samples were evacuated again in the same vacuum pressure for 12 hours before the release of DIW into the sample/vacuum chamber to occupy the evacuated pore space. The water-saturated sample was then submerged under boiled and cooled DIW to obtain the bulk volume and pore volume by the Archimedes' principle (Hu et al., 2012; 2015; Kuila et al., 2014). The bulk volume is calculated from the sample weight (wt) in DIW by Eq. 1, and volume of pore space is converted from the weight of DIW contained in sample by Eq.

2. Porosity, bulk density, and particle density can be calculated from sample weight, bulk volume, and pore volume. The uncertainty in porosity analyses by LIP is ±0.22 porosity unit (Kuila et al., 2013).

$$V_{bulk} = \frac{wt\ in\ DIW}{\rho_{DIW}} \qquad \text{(Eq. 1)}$$

$$V_{pore} = \frac{wt\ of\ DIW\ contained}{\rho_{DIW}} \qquad \text{(Eq. 2)}$$

LIP was applied for both 1-cm^3 cubic and 1-inch diameter core plug samples (with different heights in several centimeters) in this work. Hydrophilic DIW and hydrophobic 2DT (a mixture of two parts of decane and one part of toluene) were the saturating fluid for 1-cm^3 cube samples after re-drying the DIW-saturated samples, and core plug samples were only saturated with DIW for a re-use in other experiments.

2.3.2 Mercury Intrusion Porosimetry (MIP)

MIP method uses non-wetting liquid mercury to invade into pores to measure the pore-throat size distribution. As a non-wetting liquid for most geological materials, mercury could only get into geologic materials with external pressures. Washburn equation describes the relationship between the applied pressure and pore throat size being intruded (Eq. 3)

$$\Delta P = \frac{-2\gamma \cos\theta}{r} \qquad \text{(Eq. 3)}$$

where ΔP is the applied pressure, γ is the surface tension of mercury, θ is the contact angle, and r is the radius of the pore throat (Washburn, 1921). The Washburn equation is the basic theory of MIP approach in converting the applied mercury pressure to pore-throat radius. The maximum pressure that a current MIP instrument could provide is 413 MPa corresponding to the pore radius of ~3 nm (Gao et al., 2018). In MIP, the pore shape is assumed as a cylinder for the derivation of the Washburn equation. The pore

radius that MIP provided is therefore actually the pore entrance radius, the throat. Pressure difference, surface tension, and contact angle will affect the pore-throat size results and cause the uncertainties. In laboratory experiments, the surface tension and contact angle are commonly selected as 0.485 Nm^{-1} and 130° or 140°, respectively (Baiker and Reithaar, 1982; Giesche, 2006). We use the modified Washburn equation to consider variable surface tension and contact angle of Wang et al. (2016). MIP was conducted by Micromeritics AutoPore IV 9520. In addition to pore size distribution, MIP results can be used to obtain porosity, pore volume, pore surface area, and permeability (Dieb and Hooton, 1994).

2.3.3 Gas physisorption (GP)

Gas molecules could attach to the solid pore surface by Van-der Waals forces as well as the long-range London dispersion forces and short-range intermolecular repulsion. The Langmuir equation expresses the relationship of adsorbed amount and the relative pressure of the nitrogen gas, through which pore surface area, pore size distribution, and pore shape could be interpreted (Bardestani et al., 2019). At the beginning of the adsorption process of GP, the gas molecules start to be attached onto the pore surface to form a monolayer in a low relative pressure. The specific surface area can be calculated based on a monolayer coverage of nitrogen molecules with Brunauer-Emmett-Teller (BET) equation (Lowell et al., 2012; Thommes, 2010). With the relative pressure of N_2 gas increases, the multilayer thickness reaches the critical value and the capillary condensation occurs at the center of the pores. After all the pores are filled with nitrogen, the maximum pressure, P_0, will be obtained and the adsorption process finishes. Isotherm plot can be obtained by plotting adsorption volume against relative pressure at a constant experimental temperature. During the desorption process,

the filled pores start to evaporate with a decreasing N_2 pressure. When plotting the adsorption and desorption isotherms together the hysteresis loop could exist due to the pore blocking and cavitation (Schlumberger and Thommes, 2021). As the basic theory for pore size distribution analysis in GP, Kelvin equation describes the relationship of the relative pressure of N_2 and pore radius (Eq. 4), where γ is the surface tension of the condensed liquid, $\bar{V}$ is the molecular volume of the liquid, r is the pore radius, R is the universal gas constant, and T is the temperature (Lowell, 2006; Yan and Zhang, 1979).

$$\ln\frac{P}{P_0} = \frac{-2\gamma\bar{V}}{rRT} \qquad \text{(Eq. 4)}$$

Gas physisorption was conducted by the Micromeritics ASPS 2460 system with a gradual introduction of nitrogen gas into the sample under a low temperature controlled by liquid nitrogen. Pore size distribution and specific surface area were calculated by BJH and BET methods, respectively (Brunauer et al., 1938; Barret et al., 1951). The uncertainties could be caused by temperature control, equilibrium monitoring such as the sensitivity of pressure transducers, sample mass, and other factors (Pendleton and Badalyan, 2005).

2.4 (Ultra) small-angle X-ray scattering

The advanced (U)SAXS radiation approach starts to be used in shale research. The incident X-ray beam passes through the sample, and the scattered beam will be projected to the detector which could measure the scattering/beam intensity. The scattering intensity ($I(q)$) is expressed by Eq. 5

$$I(q) = \frac{16\pi^2\Delta\rho^2}{9V}\sum_{p=1}^{n} N_p r_p^6 [F(q)]^2 \qquad \text{Eq. 5}$$

where V is the sample volume covered by the beam, $\Delta\rho$ is the difference of scattering length density, N_p is the number of scatterers, r_p is the pore radius, and $F(q)$ is the form factor (Hall et al., 1986). (U)SAXS experiments were performed at beamline 9-

ID of the Advanced Photon Source at Argonne National Laboratory in Illinois. The detectable pore size range is ~1 Å-6 μm, and the range of scattering vector Q is $8\times10^{-5}< Q < 6\ A^{-1}$. Four square spots with side length of 800 μm were scanned on each sample, and each spot was scanned by USAXS for 90 s and by SAXS for 10 s with an X-ray energy of 21 keV (Wang et al., 2021). Calibration and background subtraction are needed during experiments for consequent data reduction. The data was processed by Igo Pro following Ilavsky and Jemian (2009) and Ilavsky et al. (2018). The plots in Results section came from Spot 3 except for WFD-4 which comes from Spot 1, because Spot 1 result in WFD-4 is far from its average. Porosity, pore size distribution, and pore surface area were processed from the Igo Pro, and pore volume was calculated with bulk density from MIP. The uncertainties could be contributed from the X-ray wavelength and the calculation of scattering length intensity of the samples (Gleber et al., 2010).

2.5 Scanning electron microscopy (SEM)

Image generation in SEM depends on the signals from the interaction of the electron beam and the sample surface. Signals include X-rays, backscattered electrons, secondary electrons, and Auger electrons emitted from the sample surface. Backscattered electrons (BSE) and secondary electrons (SE) are two commonly used signals in SEM image generation. The BSE images reflect the atomic number differences of the sample, as the compositional difference can be shown as different gray scale in the images. Grains with heavy elements have bright colors, such as pyrite, and grains with light elements have dark colors, such as quartz. On the other hand, SE signals could produce visual information of sample surface topography (Wells and Joy, 2006).

Energy-dispersive X-ray spectroscopy (EDS) is a commonly used chemical analyzer associated with SEM. The X-ray emitting from the sample surface mentioned before will be used in EDS for elemental analyses. The X-ray can be transferred into electron pulse and the height of the pulse is interpreted into elements by the EDS (Ngo, 1999). Eight samples were first polished by sandpapers with a sequence of 400, 800, 1200, 2400, and 3000 grids. Hitachi S-4800 instrument was applied with 10 kV for SE, and Hitachi N-3000 was applied with 20 kV for SE and 25 kV for BSE & EDS detectors. Before scanning, all the samples were coated with metal (Pt) for 1 min with Hummer VI Sputtering System and oven-dries at 60°C for 48 hrs similarly for all other characterization methods.

2.6 Fluid Flow Approach

2.6.1 Spontaneous imbibition (SI)

Spontaneous imbibition could be applied to characterize the combined influence of capillarity and relative permeability on the extent and rate of fluid flow in porous media, and sample wettability when using different imbibing fluids. Wettability describes the property of a solid when its smooth surface is in contact with a drop of fluid (Abdallah et al., 1986). The capillary force-driven spontaneous imbibition is a process in which the wetting fluid, such as water, expel a non-wetting fluid (e.g., air or oil) in a water-wet material. In the liquid moving process from one end of the sample to the other end, sorptivity (S) is introduced to quantify the rate of imbibition. Philip (1957) defined sorptivity as the combined effect of capillary pressure and relative permeability. Eq. 6 describes the relationship between cumulative imbibed water and sorptivity:

$$I(t) = St^{0.5} + At \qquad \text{Eq. 6}$$

where $I(t)$ is the imbibed mass, S is the sorptivity, t is the imbibition time, and A is an empirical constant determined by the material characteristics (Philip, 1957). The experimental procedure for imbibition tests follows Hu et al. (2001), with 1-cm^3 cubic sample hanging under a bottom-weighing electronic balance with the bottom end contacting with the imbibing liquid. The uncertainties could be caused by the vapor adsorption onto the sample and holder, and a pre-conditioning of the sample holder minimize the uncertainties.

Eight samples were imbibed with hydrophilic DIW for 24 hours and hydrophobic 2DT for 4 hours. For DIW runs, stratified samples were tested at two testing directions of imbibition process, either transverse (T direction) or parallel (P direction) to the bedding plane of the shale samples. For 2DT, only T direction was conducted.

2.6.2 Tracer Gas Diffusion

Tracer gas diffusion uses Fick's law, Archie's law, and oxygen-nitrogen exchange rate to calculate the diffusion coefficient of the rock sample (Hu and Wang, 2003; Peng et al., 2012). Gas diffusivity (D'; dimensionless) is the ratio of gas diffusion coefficient in the porous media (D_p; m^2/s) and in the air (D_a; m^2/s), which relates to the porosity (Eq. 7):

$$D' = \frac{D_p}{D_a} = \tau\sigma\emptyset_a \qquad \text{(Eq. 7)}$$

where τ is the tortuosity factor to be defined by the squared ratio of straight-line distance and actual distance, σ is constrictivity factor that can be taken as 1 in this study when the pore size is >5 nm (Hu and Wang, 2003), and $\emptyset_a$ is the air-filled porosity of the porous media. Due to the difficulty of tortuosity factor measurement in geologic porous media, an empirical equation (Eq. 8) is applied:

$\tau = \emptyset_a^{m-1}$ (Eq. 8)

where m is an empirical exponent (Hu and Wang, 2003). Therefore, gas diffusivity can be expressed as Eq. 9.

$D' = \emptyset_a^m$ (Eq. 9)

In this study, we use oxygen as the tracer gas, with its concentration detected by an oxygen sensor. The gas sensor will record the oxygen concentration within the down-gradient chamber (Peng et al., 2012), and gas diffusivity could be calculated by:

$C_r = \frac{C_t - C_s}{C_0 - C_s}$ (Eq. 10)

where C_r is the relative concentration, C_s is the oxygen concentration in air, C_t and C_0 are the oxygen concentration at time zero and time t. D_p can be calculated from the ln plot of Eq. 10, and gas diffusivity can be calculated. The core plug samples were treated with three different levels water saturation: 60°C oven-dry, 99% moisture humidity chamber saturation for 30 days, and fully DIW saturated with vacuum pulling (the LIP approach). Gas leakage and fluid evaporation from core plugs over a long testing duration may cause the uncertainty in the measurement of D_p values.

3. Results

3.1 Basic Properties of Samples

The ternary plot of lithofacies prepared by normalized XRD data shows that WFD-7, WFD-9, and WFD-328 are dominated by “quartz + feldspar” (Fig. 2). WFD-4 and WFD-8 are dominated by carbonate, and WFD-5 and WFD-6 are dominated by “quartz + feldspar” and clay. The TOC varies between 0.060 wt.% to 15.7 wt.% with an average of 5.93 wt.%. The calculated R_o% is around 0.3 with T_{max} at around 451°C (Table 1). Type I and Type II kerogen dominate the samples, with only WFD-11 dominated by Type III kerogen.

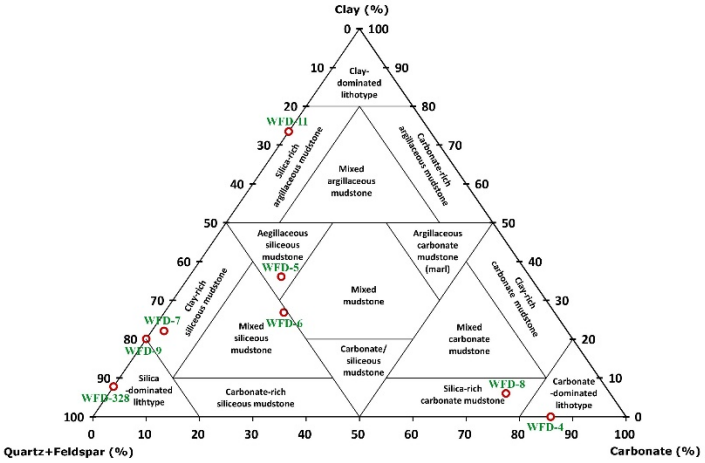

Figure 2. Ternary plot of lithofacies for the Woodford Shale

Table 1. XRD and TOC results of the Woodford Shale

Sample ID	Mineralogy (wt.%)						TOC (%)	R_o (%)	T_{max} (°C)
	Quartz	Feldspar	Dolomite	Gypsum	Clays	Pyrite			
WFD-4	13.7	0.30	84.9		0.00	1.50	4.05	0.29	414
WFD-5	25.8	14.6	15.0	11.5	31.3	1.70	7.40	0.22	410
WFD-6	40.8		18.0	12.3	21.6	7.30	10.6	0.18	408
WFD-7	75.6		2.30		22.1		0.07	0.00	374
WFD-8	17.9	1.2	72.8		5.90	0.20	8.35	0.27	413
WFD-9	68.1			13.5	17.1	1.40	15.7	0.49	425
WFD-11	26.5				73.5		0.06	0.29	414
WFD-328	92.2				7.80		1.21	0.31	415

3.2 Fluid Immersion Approaches

3.2.1 LIP results

Porosity measured by LIP with DIW varies from 1.96% to 41.1%, with an average of 19.5% in core plug samples. The results for smaller-sized cubic samples are higher than core plug samples, with an average of 21.5% in the range of 3.94% to 40.3%. The porosity of cubic samples measured with 2DT has similar values with DIW, and WFD-7, WFD-11, and WFD-328 have higher, and WFD-9 has lower values with DIW (Table 2).

Table 2. Porosity results from LIP, MIP, GP, and SAXS methods with different sample sizes and measurable pore side ranges

Sample ID	Porosity (%)				
	LIP			MIP	SAXS
	DIW		2DT		
	Core Plug	Cube	Cube		
WFD-4	2.24	3.94	3.49	3.72	3.64
WFD-5	16.4	19.5	20.2	16.9	8.63
WFD-6	17.5	18.0	18.4	16.5	5.26
WFD-7	41.1	40.3	39.1	50.37	7.88
WFD-8	1.96	7.96	8.46	6.64	2.88
WFD-9	9.44	13.8	14.7	13.2	4.51
WFD-11	36.8	37.1	35.9	43.2	6.94
WFD-328	30.5	31.1	29.6	33.0	9.32

3.2.2 MIP results

The average porosity from MIP is 22.9%, within the range of 3.72% to 50.3% (Table 2). The pore size distribution shows that most samples are dominated by mesopores and macropores (Fig. 3). For large porosity samples, such as WFD-7 and WFD-11, macropores at 1 μm and 1000 μm in diameters are the dominant pore-throat sizes. For samples with porosity smaller than 20%, mesopores at 20 nm is the major pore size. For small porosity samples, such as WFD-4 and WFD-8, mesopores at 10 nm are the primary pore size. Based on the above description, eight samples can be classified into two groups: Group 1 is dominated by pore sizes < 1 μm with WFD-4, WFD-5, WFD-6, WFD-8, and WFD-9; Group 2 is featured by large macropores > 1 μm with WFD-7, WFD-11, and WFD-328.

The cumulative pore volume varies from 0.070 cm^3/g to 0.584 cm^3/g with an average of 0.170 cm^3/g. The pore specific surface area (SSA) varies from 2.69 m^2/g to 26.2 m^2/g, with an average of 13.7 m^2/g (Fig. 4 and Table 3). Pores with sizes at 20 nm contribute to the SSA in most samples (Fig. 5). The results of SSA in WFD-4 and WFD-8 with porosities smaller than 7% are smaller than 10 m^2/g. WFD-4 only shows SSA domination at 3 nm, and WFD-8 has domination at 10 nm with minor contributions at

~50 nm. While for WFD-7, which has the largest porosity, has the minimum SSA with domination in ~1000 nm (Fig. 4).

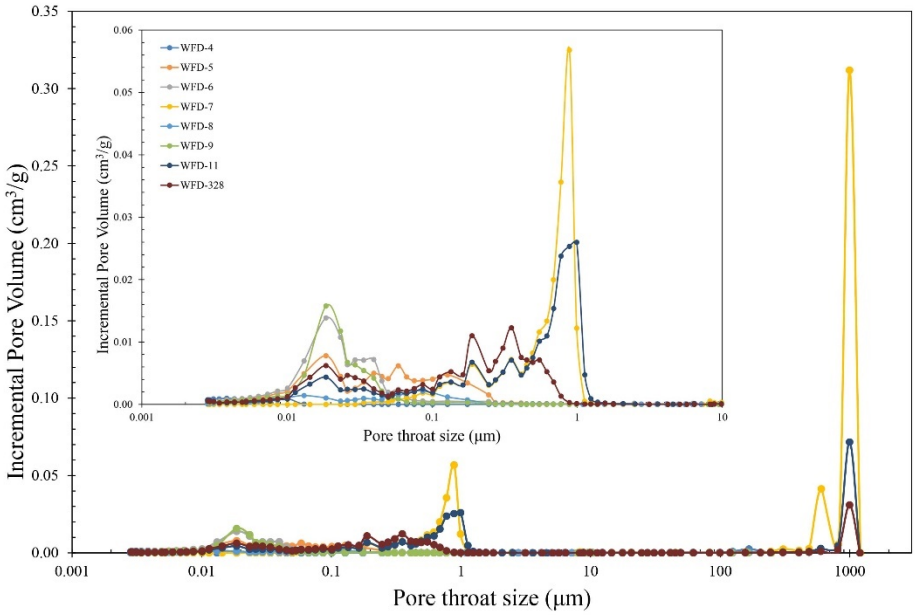

Figure 3. Incremental pore volume from MIP method

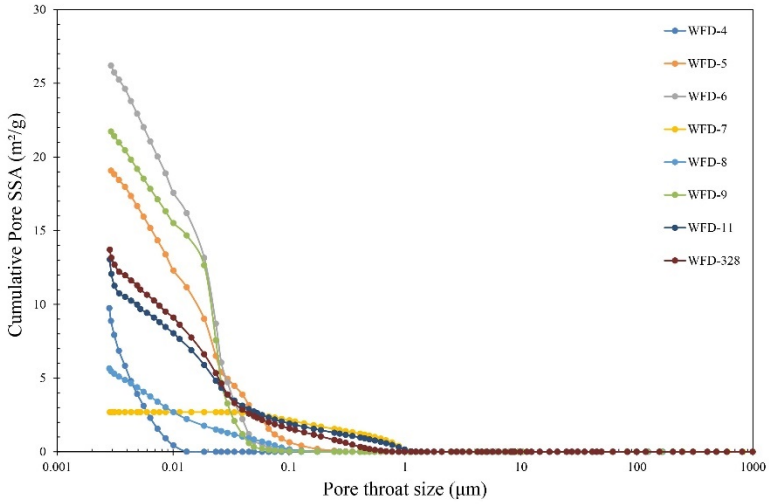

Figure 4. Cumulative pore specific surface area from MIP method

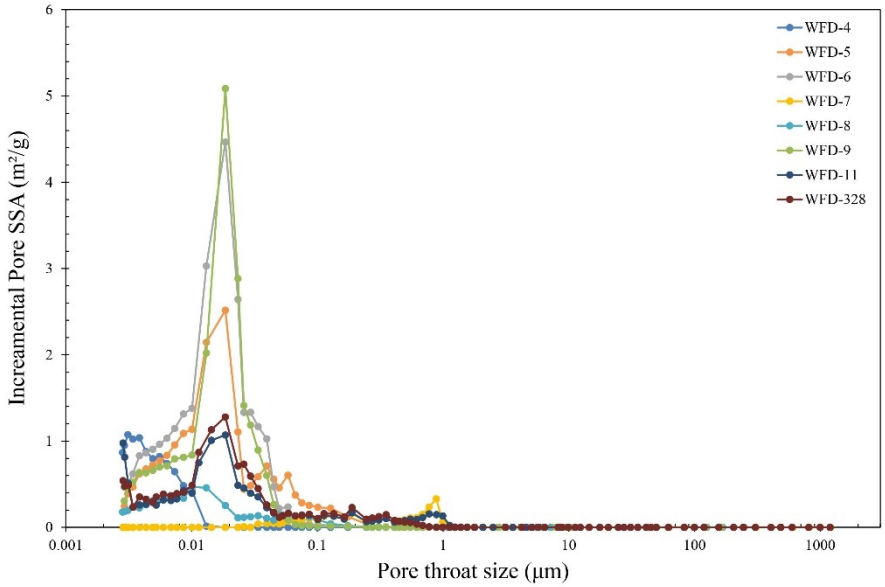

Figure 5. Incremental pore specific surface area from MIP method

Table 3. Comparison of pore volume and SSA obtained from MIP (measurable range of pore-throats from 2.8 nm-45 μm) and GP (measurable pore size diameters from 1-300 nm) methods

Sample ID	Porosity %	Cum Pore Volume (cm^3/g)		Cum pore surface area (m^2/g)	
	MIP	MIP	GP	MIP	GP (BET)
WFD-4	3.72	0.02	0.01	9.75	1.96
WFD-5	16.9	0.09	0.04	19.1	12.1
WFD-6	16.5	0.09	0.04	26.2	10.4
WFD-7	50.3	0.58	0.04	2.69	10.2
WFD-8	6.64	0.03	0.01	5.65	1.92
WFD-9	13.3	0.07	0.03	21.7	5.89
WFD-11	43.2	0.30	0.05	13.1	13.0
WFD-328	33.0	0.19	0.03	13.7	8.87

3.2.3 GP results

Pore volume and pore SSA were calculated by BJH and BET method for a measurable pore size range of 1-300 nm. In Fig. 6a, a unimodal distribution with a peak at 2-3 nm dominates the Woodford Shale samples except for sample WFD-9 which shows a wide domination peak at 15 nm. The cumulative pore volume varies from 0.009 cm^3/g to 0.048 cm^3/g with an average value of 0.031 cm^3/g. Over 50% of the cumulative pore volume is provided by mesopores. Fig. 6b shows the incremental SSA is a bimodal distribution with the domination of micropores in 1-2 nm and mesopore domination.

BET SSA is various with an average of 8.06 m^2/g in the range of 1.955 m^2/g to 12.994 m^2/g (Table 3). Eight samples have a similar hysteresis loop shape of type H3 (Fig. 7). The desorption isotherm overlaps with the adsorption isotherm at a P/P_0 of ~0.5.

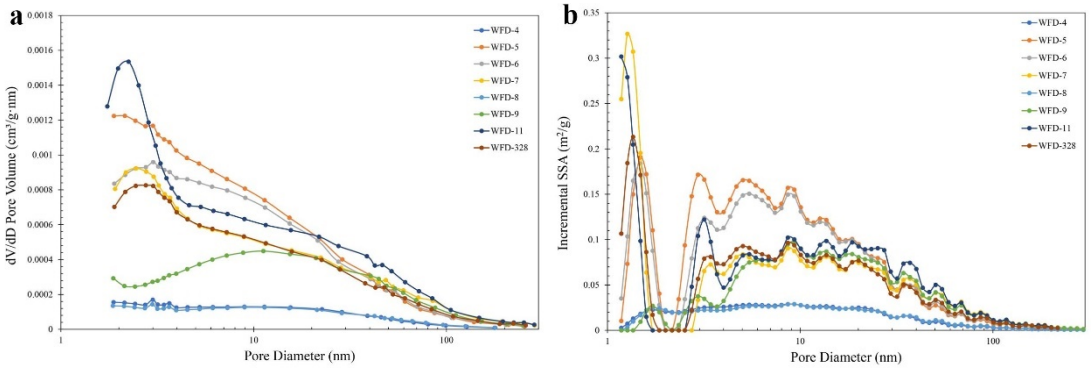

Figure 6. a) Pore size distribution and b) pore SSA distribution obtained from the GP method

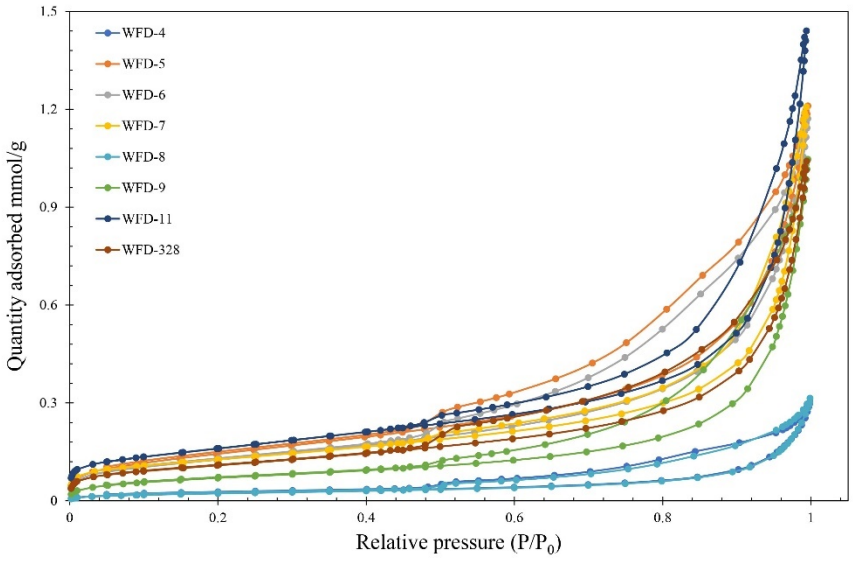

Figure 7. Nitrogen physisorption isotherms of Woodford Shale

3.3 (U)SAXS results

The porosity of eight samples measured by (U)SAXS varies from 2.88% to 9.32%, with an average of 6.13%. Plots of incremental porosity and pore volume show bimodal distributions with dominations of macropores at 50-100 nm and 400-500 nm (Fig. 8). Micropores in 2-3 nm in WFD-5 also contribute to the porosity. Pore diameters in 2-3 nm are the major contributor to the SSA (Fig. 9). There is almost no contribution

of SSA from pores greater than 100 nm. The cumulative SSA varies from 11.0 m^2/g to 42.4 m^2/g, with an average of 19.6 m^2/g.

Every sample was tested on four different measurement points except for WFD-4 with only three points. Porosity and SSA of four points in each sample are similar except for WFD-11, which has an extremely low porosity in Point 2 and WFD-328 which has extremely high SSA with similar porosity to other points (Table 4). The incremental porosity distributions of four spots except in micropores at 2-3 nm are very similar. Therefore, micropores in 2-3 nm could be the reason for the samples that show different porosity and SSA among these four points. For WFD-4, Point 3 has a higher incremental porosity at 2.5 nm, the same for WFD-11 and WFD-328 (Fig. 10).

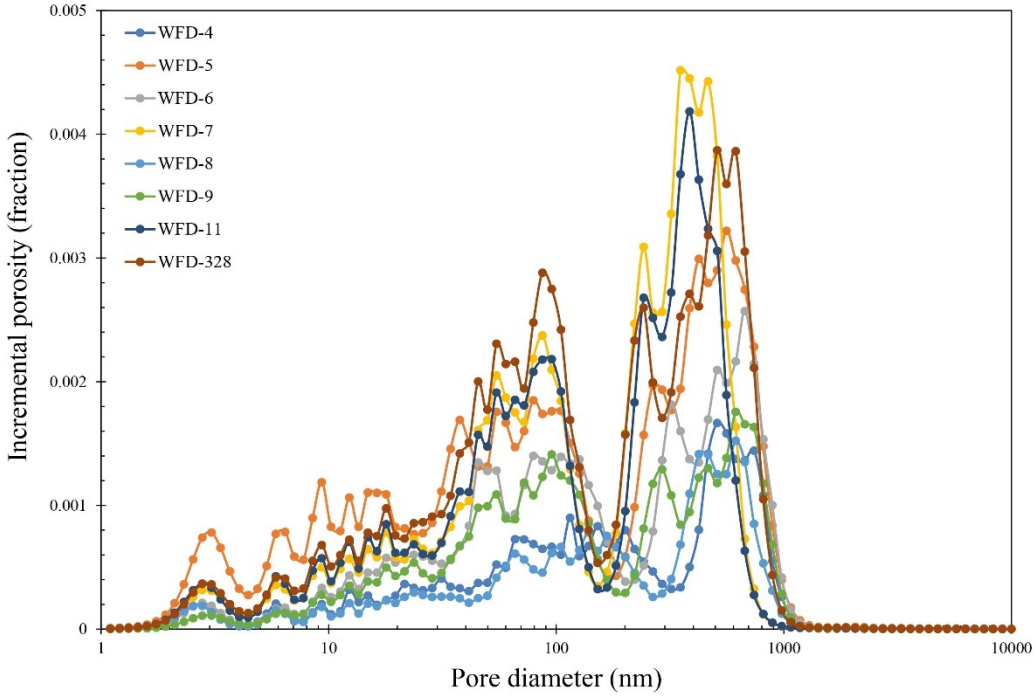

Figure 8. Incremental porosity of SAXS tests

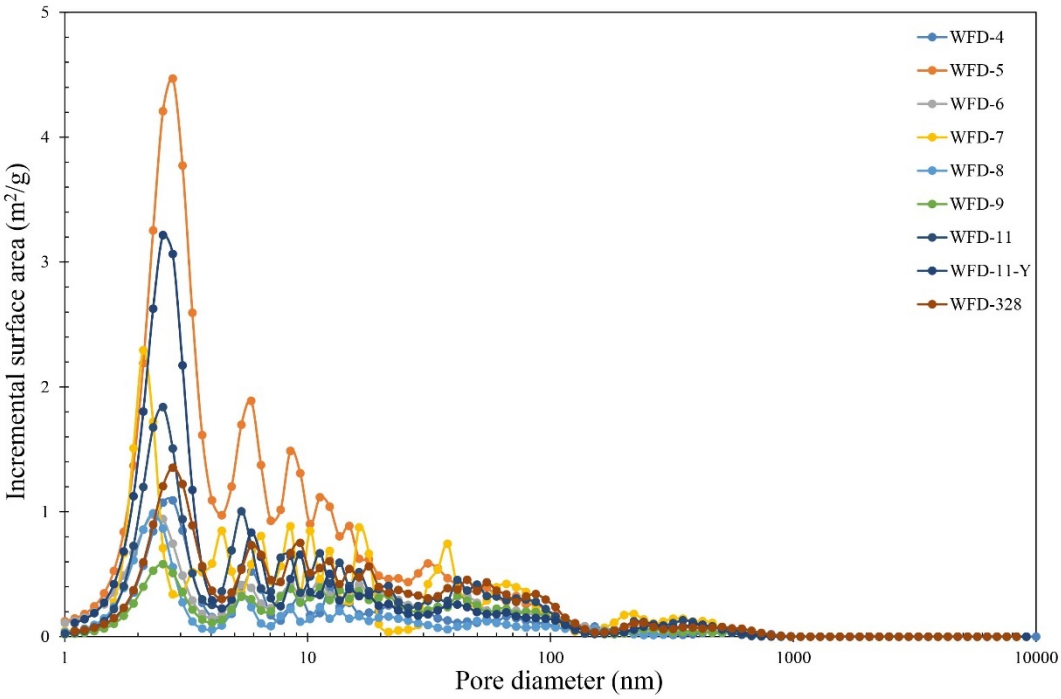

Figure 9. Incremental surface area of SAXS tests

Table 4. SAXS porosity of each measurement point

Sample ID	Porosity %				
	R1	R2	R3	R4	Average
WFD-4	3.24	3.31	4.36		3.64
WFD-5	8.66	8.65	8.42	8.79	8.63
WFD-6	5.21	4.55	5.44	5.84	5.26
WFD-7	7.86	7.44	8.07	8.16	7.88
WFD-8	2.84	2.91	2.84	2.88	2.88
WFD-9	4.56	4.10	4.35	5.04	4.51
WFD-11	6.79	0.621	7.37	6.65	6.94
WFD-328	8.59	9.57	8.93	10.2	9.32

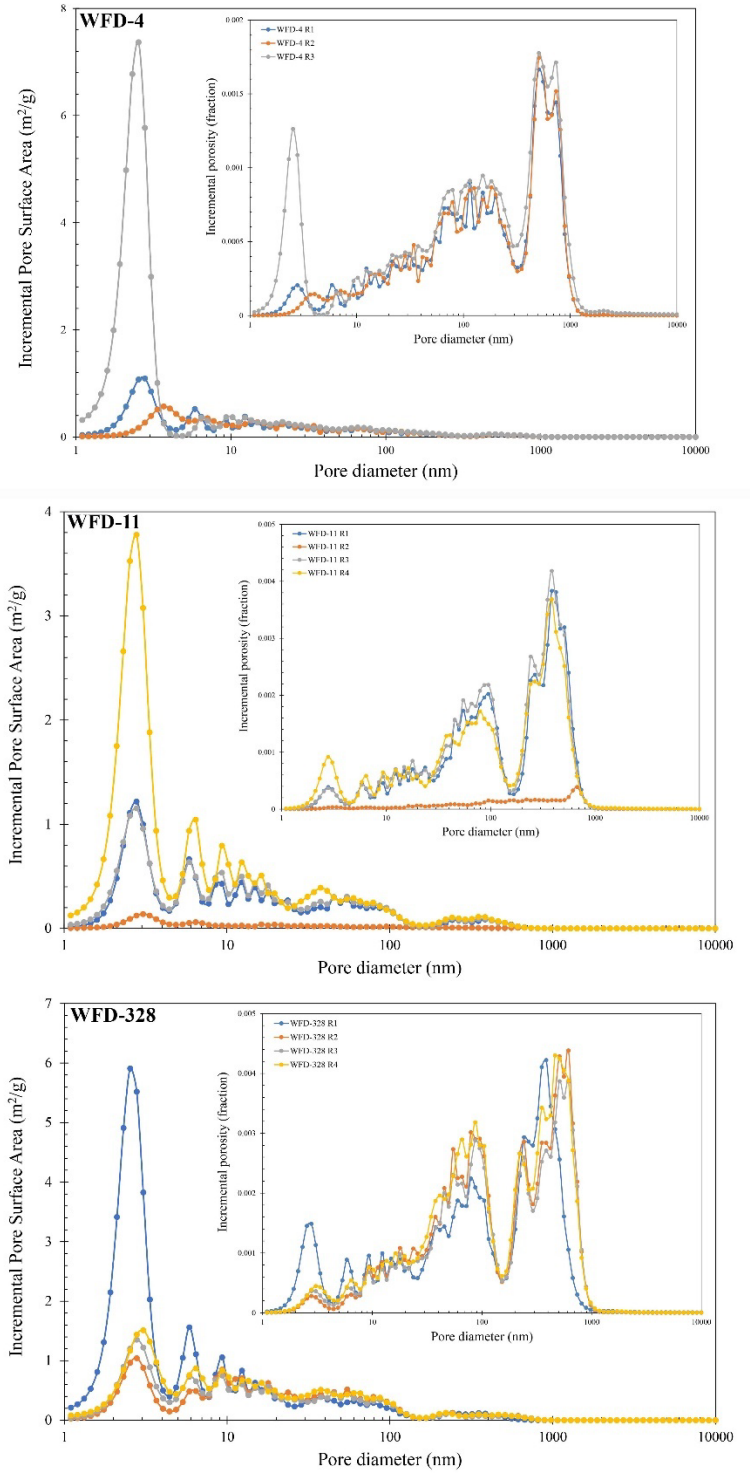

Figure 10. SAXS-derived incremental pore volume and SSA for samples of WFD-4, WFD-11, and WFD-328

3.4 SEM results

Eight samples were imaged by the SEM method under different magnifications. Interparticle pore, the pore space generated between individual particles, is the major pore type (Fig. 11c). Sheet-shaped clay minerals and gypsum contain intraparticle pores,

which are created inside of individual particles (Fig. 11d(1) pointed by the arrow). Dissolution and weathering processes could also create intraparticle pores, such as the intraparticle pores in gypsum in WFD-6 (Fig. 11e). OM pores, the pore space formed inside of organic matter, are also present in Woodford Shale samples. WFD-6 with a high TOC content has inter-connected OM pores (Fig. 11i). Most OM in Woodford Shale is shown as a covering paste on the surface of mineral particles.

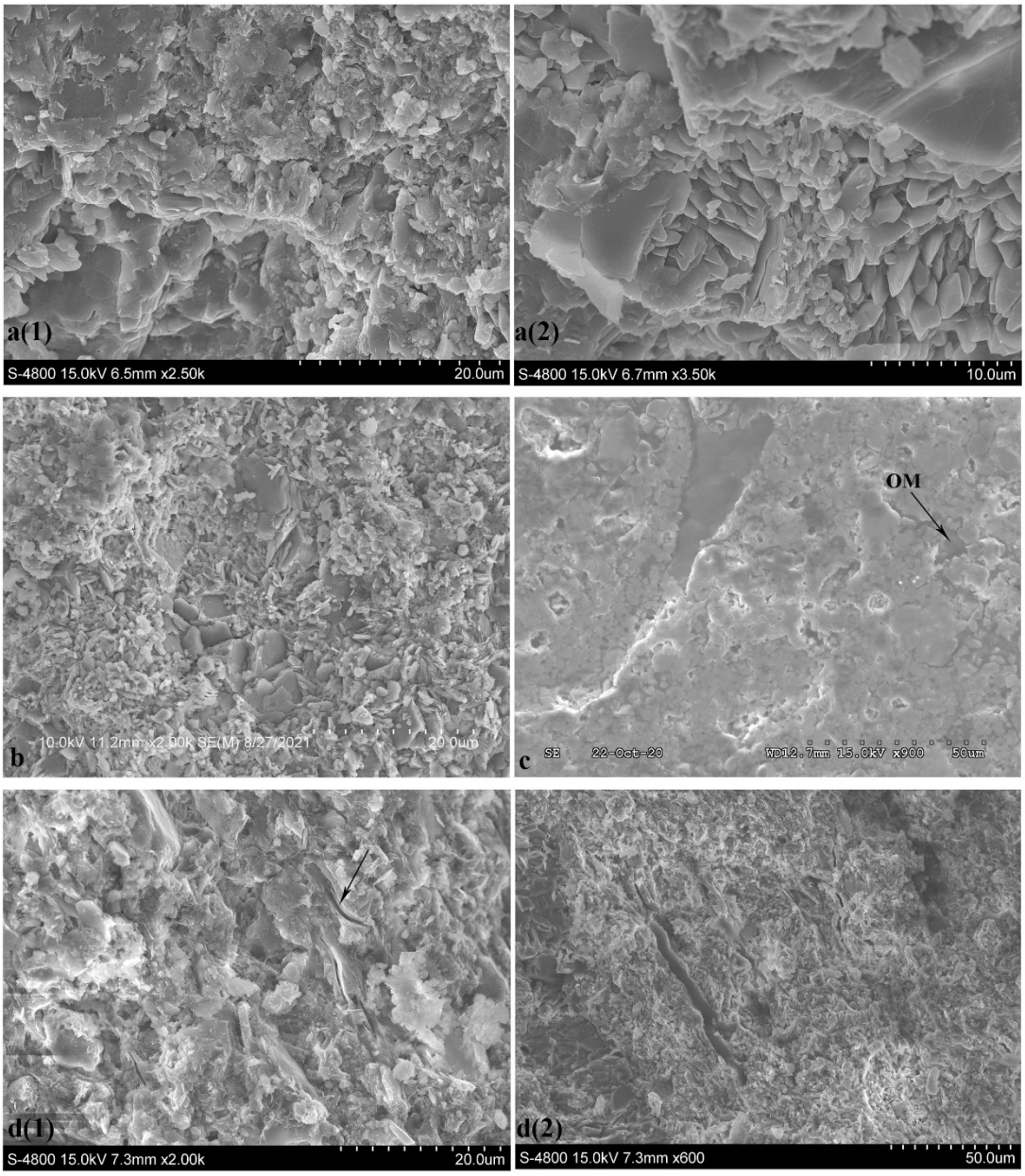

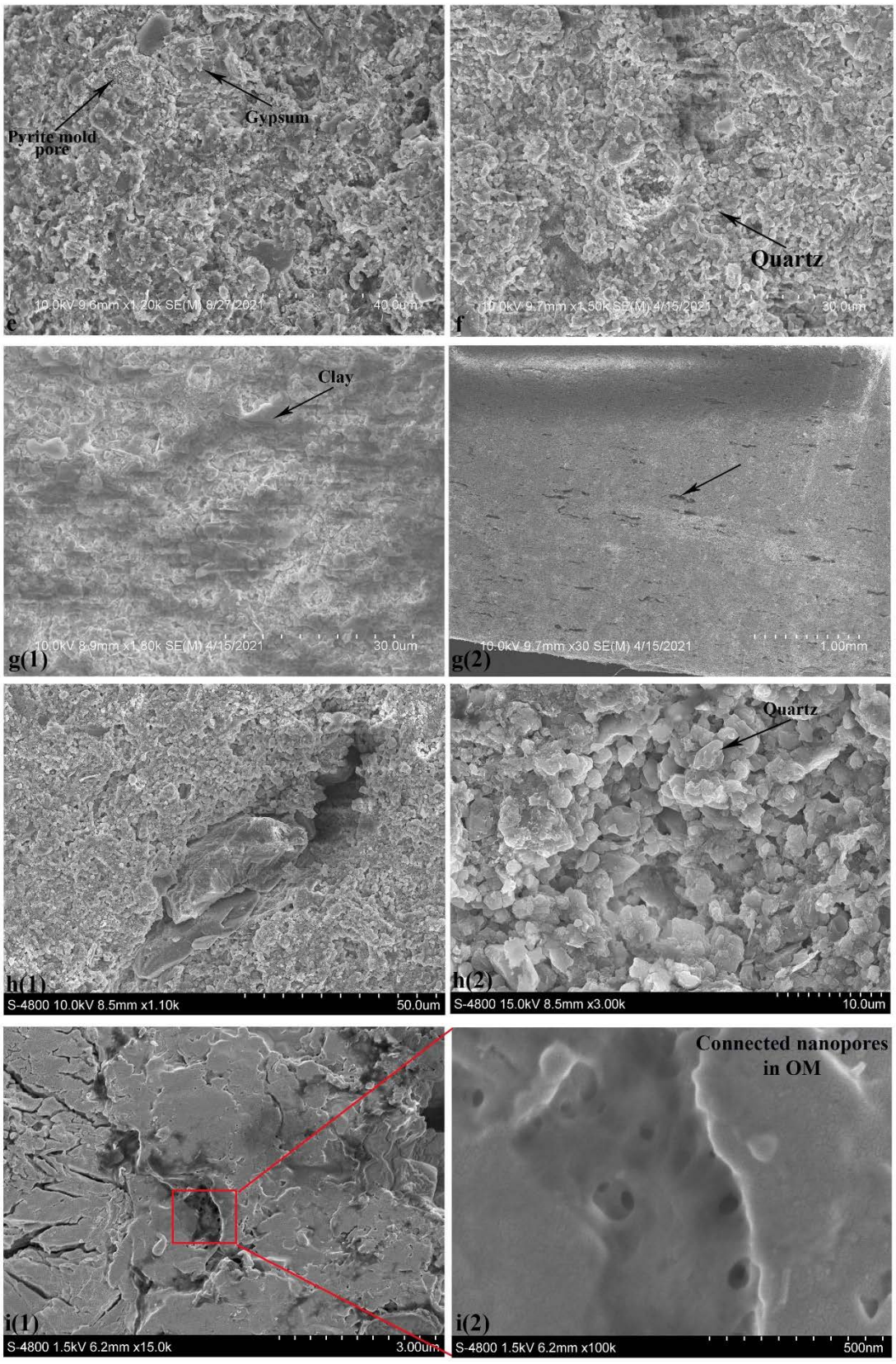

Figure 11. SEM images of Woodford Shale. a(1)(2): WFD-4; b: WFD-8; c: WFD-9; d(1)(2): WFD-5; e: WFD-6; f: WFD-7; g(1)(2): WFD-11; h(1)(2): WFD-328; i(1)(2): WFD-6.

3.3 Fluid Flow Approaches

3.3.1 SI results

In the plot of imbibition time against cumulative imbibition, eight samples in the T direction with 24 hr DIW can be separated into two groups based on the imbibition behaviors (Fig. 12). Group 1 has WFD-4, WFD-5, WFD-6, WFD-8, and WFD-9, which has no or very short plateau after 40 min of imbibition tests. Group 2 has WFD-7, WFD-11, and WFD-328 which has fast and large cumulative imbibition with a long plateau after 40 min of imbibition test. The fitting slopes in Group 1 vary from 0.105 to 0.382, and the slopes in Group 2 vary from 0.520 to 0.628 (Table 5). Samples WFD-4, WFD-5, WFD-6, WFD-8, and WFD-9 are stratified. The volumes of imbibed DIW vary from 0.032 cm^3 to 0.452 cm^3. The plotting of P direction in 24 hr DIW in these five samples has not plateau at the end of the imbibition test of 24 hr (Fig. 12a-b). The fitting slopes of these five samples vary from 0.258 to 0.471, and the imbibed DIW volumes vary from 0.017 cm^3 to 0.149 cm^3 (Table 5).

SI behaviors in 4 hr 2DT in the T direction are similar to the behavior of DIW tests. Samples WFD-7, WFD-11, and WFD-328 can be grouped as Group 1 for their high cumulative imbibition and long plateau after 20 min of imbibition (Fig. 12c). The rest of the five Woodford Shale samples are in Group 2. Samples WFD-4, WFD-5, WFD-6, and WFD-9 imbibe fast, and WFD-4 has a short plateau after 20 min of the imbibition test. Sample WFD-8 has the lowest slope among these eight samples. The imbibition slope values of eight samples with 2DT tests are all over 0.5. The imbibed 2DT volumes vary from 0.005 cm^3 to 0.431 cm^3.

The combination of imbibed volume ratio of DIW & 2DT and contact angle could classify the samples' wettability (Wang et al., 2020). The contact angles of eight samples at DIW-air-rock systems vary from 0 to 70°. The plot shows that half of these

eight samples are mix-wet and another half are water-wet with a slight preference of oil-wet (Fig. 13).

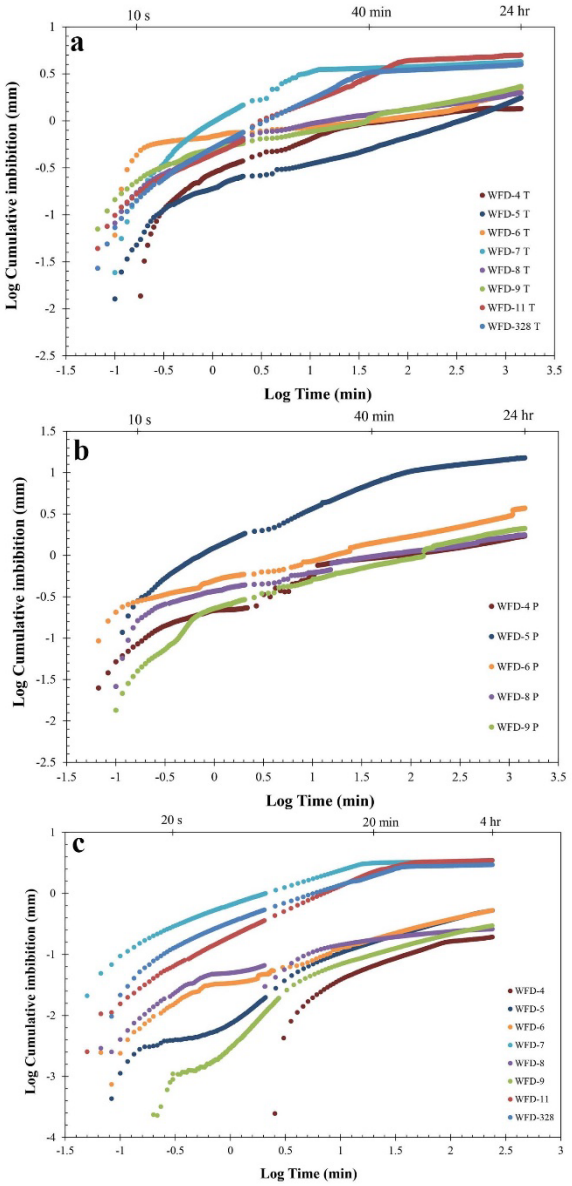

Figure 12. a. SI plot with DIW in 24 hr in T direction; b. SI plot with DIW in 24 hr in P direction; c. SI plot with 2DT in 4 hr in T direction.

Table 5. Fitted imbibition slope and imbibed liquid volume

Sample ID	Imbibition slope			Imbibed liquid volume (cm^3)		
	DIW 24 hr		2DT 4 hr	DIW 24 hr		2DT 4 hr
	T	P	T	T	P	T
WFD-4	0.382	0.353	0.563	0.032	0.017	0.005
WFD-5	0.260	0.471	0.539	0.127	0.142	0.056
WFD-6	0.105	0.272	0.543	0.082	0.149	0.068
WFD-7	0.585		0.589	0.329		0.311
WFD-8	0.181	0.258	0.499	0.042	0.067	0.022
WFD-9	0.210	0.310	0.500	0.077	0.085	0.031
WFD-11	0.520		0.867	0.452		0.431
WFD-328	0.541		0.590	0.293		0.291

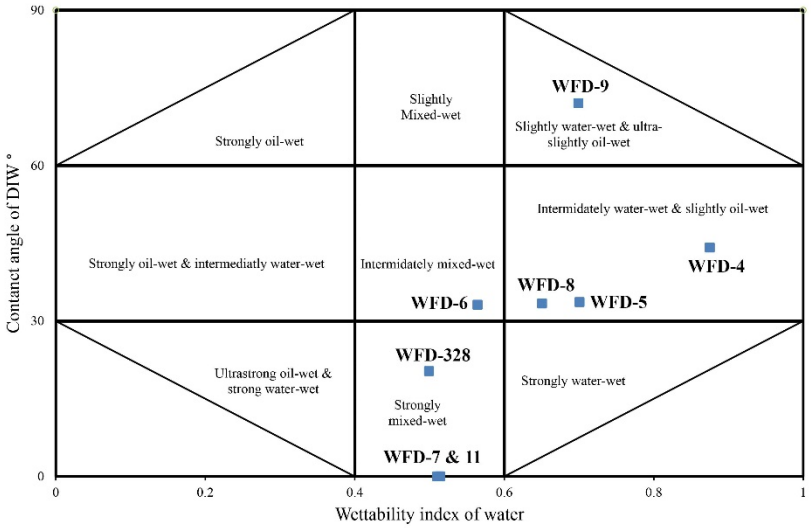

Figure 13. Wettability classification of Woodford Shale

3.3.2 Tracer gas diffusion

Three groups of D_p were measured under three different initial water saturation conditions. In oven-dry status, the D_p varies from 1.38×10^{-7} m^2/s to 9.80×10^{-7} m^2/s with an average of 3.85×10^{-7} m^2/s (Table 6). In moist (partially-wet) status with samples initially equilibrated inside a chamber with 99% relative humidity for a month with periodic monitoring of weights, the water saturations vary from 22.8% to 122% (weight gains divided by porosity obtained by using LIP for 1 cm-cubic sample sizes?) with D_p varies from 1.39×10^{-7} m^2/s to 8.21×10^{-7} m^2/s. In fully-saturated status, the water saturations vary from 65.7% to 103% with D_p varying from 3.65×10^{-8} m^2/s to 3.34×10^{-7} m^2/s.

Table 6. Gas diffusivity at three different initial moisture status of the Woodford Shale

Sample ID	Porosity, % (from LIP)	Dp (m^2/s)			Water saturation (%)	
		Oven-dry	Moist	Fully-saturated	Moist	Fully-saturated
WFD-4	2.24	1.544×10^{-7}	1.393×10^{-7}	1.380×10^{-7}	121.7	102.6
WFD-5	16.4	1.383×10^{-7}	2.764×10^{-7}	3.345×10^{-7}	58.0	96.2
WFD-6	17.5	2.061×10^{-7}	7.868×10^{-7}	2.027×10^{-7}	43.5	97.7
WFD-7	41.1	9.796×10^{-7}	8.206×10^{-7}	9.412×10^{-8}	12.8	99.1
WFD-8	1.96	1.009×10^{-7}	3.578×10^{-7}	1.021×10^{-7}	110.2	69.1
WFD-9	9.44	5.026×10^{-7}	5.152×10^{-7}	1.967×10^{-7}	85.2	90.7
WFD-11	36.8	5.074×10^{-7}	4.229×10^{-7}	1.039×10^{-7}	19.8	97.1
WFD-328	30.5	4.882×10^{-7}	3.829×10^{-7}	3.654×10^{-8}	22.8	65.7

4. Discussion

4.1 Fluid Intrusion Approaches

4.1.1 Porosity comparison among LIP and MIP

Porosities of eight Woodford Shale samples were measured in LIP and MIP (Table 2). LIP-derived porosities of samples WFD-5, WFD-8, and WFD-9 from 1-inch diameter core plugs are lower than the 1-cm^3 cubes with DIW as the saturating fluid. A decrease in sample dimensions may make more “isolated” pores connected to the sample surface and consequently increase the effective porosity (Davudov and Moghanloo, 2016; Chen et al., 2018; Zhao et al., 2021). By comparing the porosity measured by different fluids of DIW and 2DT, samples have higher TOC tend to have higher porosity by 2DT, such as WFD-5, WFD-6, WFD-8, and WFD-9, which indicates the OM-hosted pores could contribute to the pore volume in samples with TOC over 7 wt.% and more oil-wet for 2DT fluid. The porosities from LIP with 1-cm^3 cube by DIW and MIP are similar, which proves the reliability of both methods. A comparison of porosities in two methods points out the reliability of LIP and MIP and the underestimation of porosity in macropores in GP. Porosities by MIP will also be discussed in the following section.

4.1.2 Pore structure and its comparison between MIP and GP

Samples with more “quartz + feldspar” or more clays tend to have higher porosity (Fig. 1). In MIP incremental pore volume plot, macropores in 0.1-1 μm contribute to the cumulative pore volume in “quartz + feldspar” or clays dominated samples, such as for Samples WFD-7, WFD-328, and WFD-11 (Fig. 2). For samples with less “quartz + feldspar” dominations, such as Sample WFD-5, WFD-6, and WFD-8, mesopores in 10-20 nm are the major pore volume contributor. From SEM images, cement in large-porosity samples are rare, such as WFD-328 (Fig. 11h(1)). This observation is different from samples collected from well cores. The data published by Kibria et al. (2018) shows that samples dominated with “quartz + feldspar” and clays have low porosities and mesopore dominance. Severe physical and chemical weathering of the outcrop could be the reason that the outcrop samples have large porosity and macropores dominations (Jin et al., 2013). The samples with large porosities do not have large pore SSA (Fig. 3). Mesopores at 20 nm are the major contributor to pore SSA, such as WFD-6, which is dominated by mesopores and has the maximum cumulative pore SSA (Fig. 4). In summary, in “quartz + feldspar” or clays dominated samples, macropores are the major pore volume contributor. For samples with porosities of 10-30%, the mesopores contribute both to the pore volume and pore SSA.

From GP results, mesopores contribute both to the pore volume and SSA at a measurable range of 1-300 nm in pore diameters, though micropores at 1-2 nm show peaks in the pore SSA incremental plot (Fig. 6b). Around 70%-80% of the pore surface area was provided by mesopores associated with 20-30% from micropores (Table 7). The hysteresis loop in isotherm plots proves the dominance of mesopores in shale samples (Thommes et al., 2015) (Fig. 6). Type B hysteresis loop indicates that most

pores in eight samples have slit-shape based on the classification of De Boer (1958) (Labani et al., 2013) (Fig. 14). The sudden decrease in desorption before the overlapping at P/P_0 of ~0.5 indicates the ink-bottle pores cavitation (Chandra, 2020).

The shape of the hysteresis loops can be classified into two groups. Group 1 includes samples WFD-4, WFD-5, WFD-6, WFD-8, and WFD-9. The adsorption branch in Group 1 shows a fast increase at saturation vapor pressure, and the desorption branches are relatively gentle when P/P_0 values are 0.7-1, with a step-down decrease at the closure of the hysteresis loops. The hysteresis loop in Group 1 has features from

Table 7. SSA percentage at different pore sizes obtained from SAXS and GP methods

Sample ID	Measure points	SAXS SSA Percentage %					GP SSA percentage (%)		
		1-2 nm	2-50 nm	50-100 nm	0.1-1 μm	> 1 um	1-2 nm	2-50 nm	50-300 nm
WFD-4	R1	6.59	73.7	6.49	7.48	5.77	9.29	84.1	6.64
	R2	1.34	73.0	8.34	10.04	7.30			
	R3	18.5	74.2	2.33	2.82	2.16			
WFD-5	R1	4.48	82.5	4.11	3.49	5.39	13.9	82.5	3.60
	R2	5.08	80.9	4.43	3.72	5.82			
	R3	4.46	81.2	4.58	3.87	5.93			
	R4	4.54	81.1	4.57	3.84	5.91			
WFD-6	R1	9.31	65.9	8.06	7.95	8.76	15.3	80.3	4.39
	R2	4.74	69.1	8.75	8.56	8.81			
	R3	4.65	68.1	8.87	8.69	9.71			
	R4	6.29	68.1	8.42	7.96	9.22			
WFD-7	R1	4.96	68.7	8.73	8.21	9.37	29.0	63.0	7.96
	R2	3.79	69.9	9.32	8.47	8.48			
	R3	4.31	69.1	9.75	8.44	8.37			
	R4	3.18	69.6	9.67	8.04	9.55			
WFD-8	R1	9.44	71.4	6.36	8.16	4.59	9.05	83.3	7.69
	R2	9.36	71.2	6.42	8.28	4.74			
	R3	9.03	72.2	6.12	7.96	4.67			
	R4	6.67	73.5	6.36	8.43	5.08			
WFD-9	R1	3.33	65.7	10.9	9.04	11.1	2.68	86.9	10.4
	R2	3.96	64.0	11.3	9.69	11.1			
	R3	3.00	65.7	11.0	9.16	11.2			
	R4	2.97	65.9	11.1	8.66	11.4			
WFD-11	R1	3.60	73.2	8.69	6.93	7.57	21.0	71.4	7.66
	R2	3.53	74.7	5.73	9.05	6.95			
	R3	4.91	71.3	8.94	6.87	7.94			
	R4	3.65	70.8	9.36	7.30	8.90			
WFD-328	R1	11.0	78.1	3.74	3.26	3.90	21.3	72.3	6.37
	R2	3.32	66.7	11.3	8.26	10.4			
	R3	4.12	70.3	9.59	7.10	8.94			
	R4	4.32	70.1	9.41	6.77	9.36			

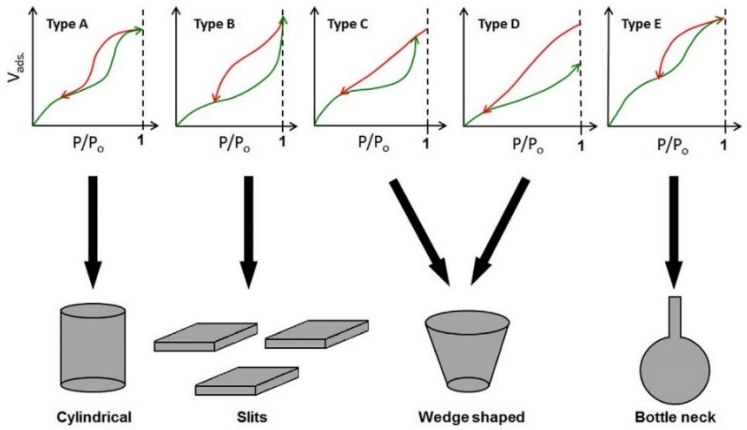

Figure 14. Hysteresis loop types and corresponding pore shapes (modified from Labani et al., 2013).

both Type B and Type D, which indicate the slit shapes and wedge shapes, respectively. This kind of pore shape could be generated by both parallel and in-parallel plate-shape minerals (Yan and Zhang, 1979; Thommes et al., 2015). Group 2 includes samples WFD-7, WFD-11, and WFD-328. Compared with Group 1, Group 2 has obvious features of Type B, which indicates the slit-shaped pores. The decreasing speed of desorption branches in samples WFD-5 and WFD-6 are slower compared to other samples (straight line in desorption branch). This slow desorption speed may be related to the continuous pore size distribution of these two samples. In Fig. 6, samples WFD-5 and WFD-6 show a gentle decrease in pore volume with pore diameters which indicates the existence of continuous pore diameters in these two samples.

Compared with MIP, the GP method could only cover pore diameters of 1-300 nm. MIP could measure pore-throat size distribution, pore volume, and SSA in a wide range from 2.8 nm to several hundreds of microns. GP could provide similar data with MIP but in a narrower range of 1-300 nm. The pores with ink-bottle shapes and distortion of pores under high pressure could cause some deviation in nano-scaled pores in MIP (Wardlaw and McKellar, 1981; Gao et al., 2018b). In Fig. 6a, the incremental pore volume decreases dramatically after 10 nm indicating that the pore detection ability of GP may decrease with pore size increase. The Kelvin equation applied in the

data reduction of GP method could underestimate the pore size for pores diameter under 10 nm (Schlumberger and Thommes, 2021; Takei et al., 1997; Thommes, 2004). Therefore, pore volume and cumulative SSA in MIP are greater than in GP (Table 3). In Figs. 3 & 6, MIP shows more pore volume distributions in 10-300 nm and GP shows more pore distributions in 1-10 nm. Using GP as supplement of MIP could offset the deficiency of MIP in 1-10 nm pores and improve the interpretation of pore shape and pore size distribution.

In summary, the combined MIP and GP data point out that the Woodford Shale is dominated by slit-shaped macropores with a continuous pore size distribution. Though LIP, MIP, and GP methods could only measure pores that are connected to the sample's surface, MIP could provide more pore structure data than other approaches. Making MIP the primary approach associated with GP and LIP will be a good combination in pore structure studies.

4.2 (U)SAXS

Unlike the fluid intrusion approach, (U)SAXS could measure both connected and isolated pores from 1-1000 nm in pore diameters. The bimodal distribution with peaks at ~100 nm and ~500 nm in Fig. 7 shows the dominance of macropores and mesopores in pore volume for these eight samples, which is similar to the data of MIP in 0.1-1μm. Table 7 shows that over 70% of SSA comes from mesopores, which is consistent with the data from the GP method. In Fig. 8, SSA tends to increase with porosity, which indicates that mesopores may also contribute to porosity for pores smaller than 1 μm. By comparing with MIP data at the same measurable range of 1 nm to 1 μm, (U)SAXS shows smaller porosity in most samples. The inaccuracy of (U)SAXS for samples with porosities over 10% may be the reason. The small

dimension of (U)SAXS measuring points (0.8 mm × 0.8 mm× ~0.8 mm in a sampling volume) and the representative elementary volume (REV) of samples could be the reason for the porosity difference between (U)SAXS and MIP (Vik et al., 2013). REV means the smallest volume from which the measurement data could be used to represent the whole sample. If the measuring point is smaller than the sample's REV, the data of these four points from one sample may be different. Compared with the GP method, (U)SAXS has greater SSA. GP and (U)SAXS have similar incremental SSA distribution modes, but (U)SAXS has a higher increment on each pore size (Table 8; Figs. 5b & 8). The pore SSA from the isolated micropores and mesopores may be the reason for the greater surface area in (U)SAXS. However, the data from isolated pores cannot be separated from (U)SAXS data, while this can be achieved by a contrast matching technique using small-angle neutron scattering (Clarkson et al., 2013).

The data of four sampling points in each sample from (U)SAXS method is similar in porosity, except for WFD-11. Spot 2 in WFD-11 has extremely low porosity, which may be caused by measurement error during the experiment (Table 7). The incremental porosity and incremental surface area plots of each sample share similar distribution models with a slight difference in micropores-mesopores of 1-3 nm (Fig. 10). This phenomenon indicates that the distributions of micropores and small-sized mesopores may be the reason for heterogeneity in these shale rocks.

In summary, (U)SAXS could give similar results with the fluid immersion approach. Unlike the MIP method, the sample will not be salvaged for safety reasons in (U)SAXS and can be re-used for follow-up experiments. The detection of isolated and connected pores in (U)SAXS could give us more data on the pore structure characterization of shale rocks. However, the limited detectable pore range up to 1 μm, sample thickness of ~0.8 mm, and the less availability make the (U)SAXS not as

popular as MIP method.

Table 8. Comparison of porosity and SSA from SAXS and GP methods at 1-300 nm pore diameters

Sample ID	1-300 nm	
	Cum SSA m^2/g	
	SAXS	GP
WFD-4	13.8	1.96
WFD-5	47.0	12.1
WFD-6	14.5	10.4
WFD-7	18.7	10.2
WFD-8	11.4	1.92
WFD-9	11.3	5.89
WFD-11	16.6	13.0
WFD-328	24.2	8.87

4.3 SEM imaging for pore types

Relationships in particle arrangement, mineralogy, and porosity could be shown from SEM imaging. The lowest clay content and tightly arranged dolomite grains with sizes of 2-4 μm create the lowest porosity in sample WFD-4 (Fig. 10a). Pore space induced by clays is shown obviously in WFD-5 (Fig. 11d(1) pointed by the arrow). The elongated intraparticle pores between clay sheets in WFD-5 are also orientated. However, clays are not the only factor that affects porosity. Samples WFD-7 and WFD-11 have the two highest porosity values. WFD-11 has a higher clays content but smaller porosity compared with WFD-7. The reason may be the clay compaction in WFD-11, which reduce porosity. WFD-11 has only 26.5% of quartz which makes WFD-11 much easier to be compacted than WFD-7. More quartz percentage in WFD-7 creates a rigid framework to prevent pore diminishing from compaction (Fig. 10f). From Fig. 10c, pores in WFD-9 always appear inside pyrite framboids and between elongate particles (gypsum), and OM with no pores is fully filled between quartz particles which may be the reason of porosity reduction. In WFD-6, intraparticle mesopores exist in OM (Fig. 10i). Samples with high TOC values tend to have more mesopores, such as samples

WFD-5, 6, & 8. It is speculated that OM may block macropores and provide more OM mesopores. In WFD-328, the contents of clays and TOC are relatively low, and the quartz percentage is the greatest in eight samples. No materials could fill the space between the mutually supported quartz grains. Therefore, WFD-328 has a higher porosity than WFD-9 (Fig. 10h). In summary, the combination of clay content, quartz percentage, TOC, and particle arrangement could affect the porosity of shale rocks. Along with SEM images, the analyses of pore structure could be more comprehensive.

4.4 Fluid Flow Approaches

In SI, five stratified samples (WFD-4, WFD-5, WFD-6, WFD-8, and WFD-9) show more DIW volume being imbibed in P direction. In WFD-4 and WFD-8, the differences in two directions are not obvious, which could be caused by the low pore volumes in these two samples. The fitted imbibition slopes in the P direction are higher than in the T direction (Table 5). The inter-layer pathway in stratified samples may help in faster imbibition in the T direction (Backberg et al., 2017). The fitting slope could indicate the pore connectivity based on the classification by Hu et al. (2002). The slope ~0.26 indicates poor pore connectivity, and the slope ~0.5 indicates good pore connectivity. The slopes with 24-hr DIW imbibition tests show different pore connectivity in eight samples. WFD-4 and WFD-5 have intermediate pore connectivity, WFD-6 and WFD-8 have poor pore connectivity, and WFD-11 and WFD-328 have good pore connectivity. For WFD-9, it shows poor connectivity in the T direction and intermediate pore connectivity in the P direction.

The slopes from 4-hr 2DT imbibition tests indicate that all the samples have better pore connectivity with a hydrophobic fluid of 2DT than a hydrophilic one of DIW. The imbibed 2DT volume increased with sample porosity. However, there is no obvious

relationship between 2DT imbibed volume and TOC & mineral percentage. The mixed wettability with slightly oil preference in the samples could be the reason of faster imbibition for the hydrophobic liquid.

According to the results of tracer gas diffusion, samples WFD-7, WFD-9, WFD-11, and WFD-328 in oven-dry status have high D_p values. Samples with large pores, small tortuosity, and good pore connectivity in pore systems could have higher D_p values (Peng et al., 2012). Therefore, the high gas diffusivities indicate the good pore connectivity in these four samples, and the rest of the samples have relatively poor pore connectivity. The data from fluid intrusion approach and SI also support this interpretation. With water content increasing from oven-dry to moist status, the D_p changings are not impressive. With water saturation increases from moist to fully-saturated conditions, the values of D_p decrease for most samples. Compared with the normal pressure in moist status, under vacuum pulling pressure water molecules block more pores and more gas passway and decrease the gas diffusivities. The decrease was dramatic in WFD-7 and WFD-328, which are dominated by large macropores at 1 μm. For samples dominated by mesopores, such as WFD-5 and WFD-6, the D_p changes between moist and fully-saturated status are not very different. In summary, water molecules could block partial mesopores and micropores but not macropores which control the pore connectivity of the Woodford Shale outcrop samples.

5. Summary

Four different approaches, including fluid immersion, radiation of (U)SAXS, visualization SEM, and fluid flow with either liquid imbibition or gas diffusion, were applied to eight Woodford Shale outcrop samples. Every approach could reflect a partial picture of the complex pore structure characteristics of shale. The data from the

fluid intrusion approach with liquid mercury and nitrogen gas indicates the dominance of slit-shaped macropores and mesopores in pore volume and pore surface area. The data from radiation (U)SAXS indicates the contribution of mesopores in surface area and the strong ability of (U)SAXS in mesopore and micropore measurement. SEM images show grain arrangement, grain orientation, and pore type, including primary interparticle pores, OM pores, and intraparticle pores. The data from the fluid flow approach indicates that the pore connectivity in Woodford Shale is intermediate to good connectivity towards hydrophilic DIW. The results also indicate that quartz or feldspar content has positive relationship with porosity.

By comparing these four approaches, the MIP method of fluid intrusion approach has advantages of pore size distribution, pore volume, and surface area measurement within a wide measurable range of nm-μm. The information gathered from GP and SEM methods could provide more details in pore shape and pore arrangements for better pore structure characterization. Therefore, taking MIP as the major experiment in association with GP and SEM methods could be a good combination in pore structure studies.

Acknowledgment

We thank the financial support from the Nuclear Energy University Program managed by the Office of Nuclear Energy at U.S. Department of Energy (award number DE-NE0008797). The X-ray scattering data were collected at the X-ray Science Division beamline of 9-ID, a resource of the Advanced Photon Source, a U.S. Department of Energy (DOE) Office of Science User Facility operated for the DOE Office of Science by Argonne National Laboratory under Contract No. DE-AC02-06CH11357.

References

Baiker, A., & Reithaar, A. (1982). Contact angle of mercury against catalyst materials for use in intrusion porosimetry. Industrial & Engineering Chemistry Product Research and Development, 21(4), 590-591.

Bardestani, R., Patience, G. S., & Kaliaguine, S. (2019). Experimental methods in chemical engineering: specific surface area and pore size distribution measurements—BET, BJH, and DFT. The Canadian Journal of Chemical Engineering, 97(11), 2781-2791.

Barrett, E. P., Joyner, L. G., & Halenda, P. P. (1951). The determination of pore volume and area distributions in porous substances. I. Computations from nitrogen isotherms. Journal of the American Chemical society, 73(1), 373-380.

Bernal, A. S., Mayorga, L. C., Prada, A. G., & Slatt, R. M. (2012). Geological characterization of the Woodford Shale, McAlester Cemetery quarry, Oklahoma. Oklahoma: Shale Shaker, v. 63, p. 202-213.

Brunauer, S., Emmett, P. H., & Teller, E. (1938). Adsorption of gases in multimolecular layers. Journal of the American Chemical Society, 60(2), 309-319.

Cardott, B. J. (2005). Overview of unconventional energy resources of Oklahoma. In Unconventional energy resources in the southern mid-continent. 2004 Symposium Oklahoma Geological Survey Circular, Vol. 110, pp. 7-18.

Cardott, B. J. (2012). Thermal maturity of Woodford Shale gas and oil plays, Oklahoma, USA. International Journal of Coal Geology, 103, 109-119.

Cardott, B. J. (2017). Oklahoma Shale Resource Plays. Oklahoma Geology Notes, 76(2), 21-30.

Chalmers, G. R., Bustin, R. M., & Power, I. M. (2012). Characterization of gas shale pore systems by porosimetry, pycnometry, surface area, and field emission scanning electron microscopy/transmission electron microscopy image analyses: Examples from the Barnett, Woodford, Haynesville, Marcellus, and Doig units Characterization of Gas Shale Pore Systems. AAPG Bulletin, 96(6), 1099-1119.

Chen, Y., Qin, Y., Wei, C., Huang, L., Shi, Q., Wu, C., & Zhang, X. (2018). Porosity changes in progressively pulverized anthracite subsamples: Implications for the study of closed pore distribution in coals. Fuel, 225, 612-622.

Clarkson, C. R., Solano, N., Bustin, R. M., Bustin, A. M. M., Chalmers, G. R. L., He, L., Melnichenko, Y. B., Radlinski, A. P., Blach, T. P., (2013). Pore structure characterization of North American shale gas reservoirs using USANS/SANS, gas adsorption, and mercury intrusion. Fuel, 103, 606-616.

Comer, J. B. (1991). Stratigraphic analysis of the upper Devonian Woodford formation, Permian basin, west Texas and southeastern New Mexico (Vol. 201). Bureau of Economic Geology, University of Texas at Austin.

Comer, J. B. (2008). Distribution and source-rock characteristics of Woodford Shale and age-equivalent strata. In Poster Panel Presented at 2008 AAPG Annual Convention held in San Antonio, Texas, USA.

Craig, Jr., F. F., 1971, The reservoir engineering aspects of waterflooding. Richardson, Texas, SPE Monograph Series 3, 12–44.

Curtis, M. E., Cardott, B. J., Sondergeld, C. H., & Rai, C. S. (2012). Development of organic porosity in the Woodford Shale with increasing thermal maturity. International Journal of Coal Geology, 103, 26-31.

Cullen, A. (2020). Woodford shale mercury anomalies from the McAlister Cemetery Quarry, Oklahoma: A North American test of the volcanic-trigger hypothesis for Late Devonian mass extinctions. Shale Shaker Vol 71, No 5 September-October.

Davudov, D., Moghanloo, R. G. (2016). Upscaling of pore connectivity results from lab-scale to well-scale for Barnett and Haynesville Shale Plays. SPE Annual Technical Conference and Exhibition, Society of Petroleum Engineers.

De Boer, J. H., 1958, The shape of capillaries, in D. H. Evertt and R. H. Ottewill, eds., The structure and properties of porous materials. London, Butterworths, p. 68–94.

Dong, T., Harris, N. B., Ayranci, K., Twemlow, C. E., & Nassichuk, B. R. (2015). Porosity characteristics of the Devonian Horn River shale, Canada: Insights from lithofacies classification and shale composition. International Journal of Coal Geology, 141, 74-90.

Ekwunife, I. C. (2017). Assessing Mudrock Characteristics, High-resolution Chemostratigraphy, and Sequence Stratigraphy of the Woodford Shale in the McAlister Cemetery Quarry, Ardmore Basin, Oklahoma, Master Thesis, University of Oklahoma.

El-Dieb, A. S., & Hooton, R. D. (1994). Evaluation of the Katz-Thompson model for estimating the water permeability of cement-based materials from mercury intrusion porosimetry data. Cement and Concrete Research, 24(3), 443-455.

Extrand, C. W. (2016). Uncertainty in contact angle measurements from the tangent method. Journal of Adhesion Science and Technology, 30(15), 1597-1601.

Gao, Z., & Hu, Q. (2018). Pore structure and spontaneous imbibition characteristics of marine and continental shales in China. AAPG Bulletin, 102(10), 1941-1961.

Gao, Z., Hu, Q., & Hamamoto, S. (2018b). Using multicycle mercury intrusion porosimetry to investigate hysteresis phenomenon of different porous media. Journal of Porous Media, 21(7).

Giesche, H. (2006). Mercury porosimetry: A general (practical) overview. Particle & Particle Systems Characterization, 23(1), 9-19.

Gleber, G., Cibik, L., Haas, S., Hoell, A., Müller, P., & Krumrey, M. (2010, October). Traceable size determination of PMMA nanoparticles based on Small Angle X-ray Scattering (SAXS). In Journal of Physics: Conference Series (Vol. 247, No. 1, p. 012027). IOP Publishing.

Gorynski, K. E., Tobey, M., Enriquez, D., Smagala, T., Dreger, J., & Newhart, R. (2017). Quantification and characterization of hydrocarbon-filled porosity in liquid-rich shales using basic programed thermal extraction and pyrolysis, LECO-TOC, Archimedes bulk density, and helium pycnometry measurements. In SPE/AAPG/SEG Unconventional Resources Technology Conference. OnePetro.

Granath, J. W. (1989). Structural evolution of the Ardmore Basin, Oklahoma: Progressive deformation in the foreland of the Ouachita collision. Tectonics, 8(5), 1015-1036.

Hall, P. L., Mildner, D. F., & Borst, R. L. (1986). Small-angle scattering studies of the pore spaces of shaly rocks. Journal of Geophysical Research: Solid Earth, 91(B2), 2183-2192.

Heller, R., Vermylen, J., & Zoback, M. (2014). Experimental investigation of matrix permeability of gas shales. AAPG Bulletin, 98(5), 975-995.

Hu, M. Q., Persoff, P., & Wang, J. S. (2001). Laboratory measurement of water imbibition into low-permeability welded tuff. Journal of Hydrology, 242(1-2), 64-78.

Hu, Q., Ewing, R. P., & Dultz, S. (2012). Low pore connectivity in natural rock. Journal of Contaminant Hydrology, 133, 76-83.

Hu, H., Zhang, T., Wiggins-Camacho, J. D., Ellis, G. S., Lewan, M. D., & Zhang, X.

(2015). Experimental investigation of changes in methane adsorption of bitumen-free Woodford Shale with thermal maturation induced by hydrous pyrolysis. Marine and Petroleum Geology, 59, 114-128.

Hu, Q., & Wang, J. S. (2003). Aqueous-phase diffusion in unsaturated geologic media: A review. Critical Reviews in Environmental Science and Technology, 33(3): 275-297

Ilavsky, J., & Jemian, P. R. (2009). Irena: tool suite for modeling and analysis of small-angle scattering. Journal of Applied Crystallography, 42(2), 347-353.

Ilavsky, J., Zhang, F., Andrews, R. N., Kuzmenko, I., Jemian, P. R., Levine, L. E., & Allen, A. J. (2018). Development of combined microstructure and structure characterization facility for in situ and operando studies at the Advanced Photon Source. Journal of Applied Crystallography, 51(3), 867-882.

Jarvie, D. M., Hill, R. J., Ruble, T. E., & Pollastro, R. M. (2007). Unconventional shale-gas systems: The Mississippian Barnett Shale of north-central Texas as one model for thermogenic shale-gas assessment. AAPG Bulletin, 91(4), 475-499.

Jin, L., Mathur, R., Rother, G., Cole, D., Bazilevskaya, E., Williams, J., Carone, A & Brantley, S. (2013). Evolution of porosity and geochemistry in Marcellus Formation black shale during weathering. Chemical Geology, 356, 50-63.

Kibria, M. G., Hu, Q., Liu, H., Zhang, Y., & Kang, J. (2018). Pore structure, wettability, and spontaneous imbibition of Woodford shale, Permian Basin, West Texas. Marine and Petroleum Geology, 91, 735-748.

Kirkland, D. W., Denison, R. E., Summers, D. M., Gormly, J. R., Johnson, K. S., & Cardott, B. J. (1992). Geology and organic geochemistry of the Woodford Shale in the Criner Hills and western Arbuckle Mountains, Oklahoma. Oklahoma Geological Survey Circular, 93, 38-69

Ko, L. T., Ruppel, S. C., Loucks, R. G., Hackley, P. C., Zhang, T., & Shao, D. (2018). Pore-types and pore-network evolution in Upper Devonian-Lower Mississippian Woodford and Mississippian Barnett mudstones: Insights from laboratory thermal maturation and organic petrology. International Journal of Coal Geology, 190, 3-28.

Kuila, U., McCarty, D. K., Derkowski, A., Fischer, T. B., & Prasad, M. (2014). Total porosity measurement in gas shales by the water immersion porosimetry (WIP) method. Fuel, 117, 1115-1129.

Labani, M. M., Rezaee, R., Saeedi, A., & Al Hinai, A. (2013). Evaluation of pore size spectrum of gas shale reservoirs using low pressure nitrogen adsorption, gas expansion and mercury porosimetry: A case study from the Perth and Canning Basins, Western Australia. Journal of Petroleum Science and Engineering, 112, 7-16.

Lewan, M. D., & Sonnenfeld, M. D. (2017, September). Determining quantity and quality of retained oil in mature marly chalk and marlstone of the Cretaceous Niobrara Formation by low-temperature hydrous pyrolysis. In Unconventional Resources Technology Conference, Austin, Texas, 24-26 July 2017 (pp. 1308-1315). Society of Exploration Geophysicists, American Association of Petroleum Geologists, Society of Petroleum Engineers.

Liu, B., Teng, J., Mastalerz, M., Schieber, J., Schimmelmann, A., & Bish, D. (2021). Compositional control on shale pore structure characteristics across a maturation gradient: Insights from the Devonian New Albany Shale and Marcellus Shale in the eastern United States. Energy & Fuels, 35(9), 7913-7929.

Loucks, R. G., & Ruppel, S. C. (2007). Mississippian Barnett Shale: Lithofacies and depositional setting of a deep-water shale-gas succession in the Fort Worth

Basin, Texas. AAPG Bulletin, 91(4), 579-601.
Lowell, S., Shields, J. E., Thomas, M. A., & Thommes, M. (2012). Characterization of porous solids and powders: Surface area, pore size and density (Vol. 16). Springer Science & Business Media, New York City, USA.
Milliken, K. L., Rudnicki, M., Awwiller, D. N., & Zhang, T. (2013). Organic matter–hosted pore system, Marcellus formation (Devonian), Pennsylvania. AAPG Bulletin, 97(2), 177-200.
Moore, D. M., & Reynolds, R. C. (1997). X-ray Diffraction and the Identification and Analysis of Clay Minerals. 2nd Edition, Oxford University Press, New York.
Muller, P. (1994). Glossary of terms used in physical organic chemistry (IUPAC Recommendations 1994). Pure and Applied Chemistry, 66(5), 1077-1184.
Ngo, P. D. (1999). Energy dispersive spectroscopy. In Failure Analysis of Integrated Circuits (pp. 205-215). Springer, Boston, MA.
Ojha, S. P., Misra, S., Sinha, A., Dang, S., Tinni, A., Sondergeld, C., & Rai, C. (2018). Relative permeability and production-performance estimations for Bakken, Wolfcamp, Eagle Ford, and Woodford shale formations. SPE Reservoir Evaluation & Engineering, 21(02), 307-324.
Parker, M. A., Buller, D., Petre, J. E., & Dreher, D. T. (2009). Haynesville shale-petrophysical evaluation. SPE Rocky Mountain Petroleum Technology Conference. OnePetro.
Peng, S., Hu, QH., and Hamamoto, S., (2012). Diffusivity of rocks: Gas diffusion measurements and correlation to porosity and pore size distribution. Water Resources Research 48, no. 2.
Pendleton, P., & Badalyan, A. (2005). Gas adsorption data uncertainty and propagation analyses. Adsorption, 11(1), 61-66.
Philip, J. R. (1957). The theory of infiltration: 4. Sorptivity and algebraic infiltration equations. Soil Science, 84(3), 257-264.
Romero, M. A., & Philp, R. P. (2012). Organic geochemistry of the Woodford Shale, southeastern Oklahoma: How variable can shales be. AAPG Bulletin, 96(3), 493-517.
Slatt, R. M., & O'Brien, N. R. (2011). Pore types in the Barnett and Woodford gas shales: Contribution to understanding gas storage and migration pathways in fine-grained rocks. AAPG Bulletin, 95(12), 2017-2030.
Stalder, A. F., Kulik, G., Sage, D., Barbieri, L., & Hoffmann, P. (2006). A snake-based approach to accurate determination of both contact points and contact angles. Colloids and Surfaces A: Physicochemical and Engineering Aspects, 286(1-3), 92-103.
Stalder, A. F., Melchior, T., Müller, M., Sage, D., Blu, T., & Unser, M. (2010). Low-bond axisymmetric drop shape analysis for surface tension and contact angle measurements of sessile drops. Colloids and Surfaces A: Physicochemical and Engineering Aspects, 364(1-3), 72-81.
Schlumberger, C., & Thommes, M. (2021). Characterization of hierarchically ordered porous materials by physisorption and mercury porosimetry—A tutorial review. Advanced Materials Interfaces, 8(4), 2002181.
Takei, T., Chikazawa, M., & Kanazawa, T. (1997). Validity of the Kelvin equation in estimation of small pore size by nitrogen adsorption. Colloid and Polymer Science, 275(12), 1156-1161.
Tiab, D., & Donaldson, E. C. (2015). Petrophysics: Theory and Practice of Measuring Reservoir Rock and Fluid Transport Properties. Gulf Professional Publishing, Houston, TX, USA.

Thommes, M. (2004). Physical adsorption characterization of ordered and amorphous mesoporous materials. In Nanoporous Materials: Science and Engineering (pp. 317-364).

Thommes, M., Kaneko, K., Neimark, A. V., Olivier, J. P., Rodriguez-Reinoso, F., Rouquerol, J., & Sing, K. S. (2015). Physisorption of gases, with special reference to the evaluation of surface area and pore size distribution (IUPAC Technical Report). Pure and Applied Chemistry, 87(9-10), 1051-1069.

Wang, P., Jiang, Z., Chen, L., Yin, L., Li, Z., Zhang, C., Tang, X. & Wang, G.. (2016). Pore structure characterization for the Longmaxi and Niutitang shales in the Upper Yangtze Platform, South China: Evidence from focused ion beam–He ion microscopy, nano-computerized tomography and gas adsorption analysis. Marine and Petroleum Geology, 77, 1323-1337.

Wang, Q., Zhou, W., Hu, Q., Xu, H., Meendsen, F., Shu, Y., & Qiao, H. (2020). Pore geometry characteristics and fluid–rock interaction in the Haynesville Shale, East Texas, United States. Energy & Fuels, 35(1), 237-250.

Wang, Q., Hu, Q., Ning, X., Ilavsky, J., Kuzmenko, I., & Tom, T. (2021). Spatial heterogeneity analyses of pore structure and mineral composition of Barnett Shale using X-ray scattering techniques. Marine and Petroleum Geology, 134, 105354.

Wang, Q., Hu, Q., Larsen, C., Zhao, C., Sun, M., Zhang, Y., & Zhang, T. (2021). Microfracture-pore structure characterization and water-rock interaction in three lithofacies of the Lower Eagle Ford Formation. Engineering Geology, 292, 106276.

Wang, T. Y., Tian, S. C., Liu, Q. L., Li, G. S., Sheng, M., Ren, W. X., & Zhang, P. P. (2021). Pore structure characterization and its effect on methane adsorption in shale kerogen. Petroleum Science, 18(2), 565-578.

Wardlaw, N. C., & McKellar, M. (1981). Mercury porosimetry and the interpretation of pore geometry in sedimentary rocks and artificial models. Powder Technology, 29(1), 127-143.

Washburn, E. W. (1921). Note on a method of determining the distribution of pore sizes in a porous material. Proceedings of the National Academy of Sciences of the United States of America, 7(4), 115.

Wells, O. C., & Joy, D. C. (2006). The early history and future of the SEM. Surface and Interface Analysis, 38(12‐13), 1738-1742

Yan, J., Zhang, Q., & Gao, J. C. (1979). Adsorption and Condensation-the Surface and Pore of Solid. Scientific Press, Beijing, 118-124 pp.

Zheng, H., Yang, F., Guo, Q., Pan, S., Jiang, S., & Wang, H. (2022). Multi-scale pore structure, pore network and pore connectivity of tight shale oil reservoir from Triassic Yanchang Formation, Ordos Basin. Journal of Petroleum Science and Engineering, 212, 110283.

Zhao, C., Zhou, W., Hu, Q. H., Xu, H., & Zhang, C. (2021). Porosity measurement of granular rock samples by modified bulk density analyses with particle envelopment. Marine and Petroleum Geology, 133, 105273.

Chapter III

Regional petrophysical studies on Wolfcamp Shale in Texas: Sedimentary features and mineralogy effects on pore systems

Chen Zhao[1], Qinhong Hu[1], Qiming Wang[1], Majie Fan[1], and Jan Ilavsky[2]

[1]Department of Earth and Environment Sciences, The University of Texas at Arlington, 500 Yates Street, Arlington, TX, 76019, USA

[2] X-ray Science Division, Advanced Photon Source, Argonne National Laboratory, Lemont, IL 60439, USA.

Abstract

A total of 13 Wolfcamp Shale core samples from six wells in Midland Basin of West Texas were measured by liquid immersion porosimetry, mercury intrusion porosimetry, gas physisorption, small angle X-ray scattering, polarized microscopy & scanning electronic microscopy, and spontaneous imbibition. The organic matter is composed of Type II and Type III kerogen with a low maturity in oil window. Lithofacies of mudstone and calcareous mudstone were identified from 13 samples with a hemiplegic depositional environment. Four main types of pores were classified to include slit-shaped mesopores, slit-shaped macropores, wedge-shaped mesopores, and wedge-shapes macropores. Diameters of 4-5 nm and 10 nm are the major pore size of mesopores, and 100 nm is the major pore size of macropores. A sandwich structure composed by quartz/feldspar grains and clay minerals is the primary structure in slit-shaped mesopore formation and fluid flow in Wolfcamp Shale. In addition, grain size has little effect on pore structure.

1. Introduction

As the 7th largest oil and gas basin in the world, Permian Basin in west Texas and southeast New Mexico has supplied over 35.6 billion barrels (bbl) of oil and 125 trillion cubic feet (tcf) of gas since 1920s to January 2020 (U.S. Energy Information Administration, 2020). Among dozens of plays in Permian Basin, Wolfcamp Shale becomes one of the largest petroleum plays in USA for its high production of crude oil from 2011 to 2021 and its large potential petroleum reserves with over 19 bbl of oil and 15 tcf of gas (U.S. Energy Information Administration, 2020a; 2020b). Studies of unconventional reservoirs and hydraulic fracturing enhance the demand for shale pore

structure research. As strong heterogeneity and low permeability are the features of unconventional shale reservoirs, therefore, multiple methods coupled with sedimentary and mineralogical studies are necessary in shale pore structure studies. Previous studies indicate that shale composition such as quartz, carbonate (calcite and dolomite), clays, and TOCs could significantly affect the pore structure of shales such as Wolfcamp Shale (Tang et al., 2015; Yang et al., 2017; Liu et al., 2017; Perry et al., 2017; Peng et al., 2019; Yuan et al., 2019; Colborne, 2020; Ramiro-Ramirez et al., 2020).

As the primary economic oil and gas target in the US, the Early Permian Wolfcamp Shale is distributed in both Delaware Basin and Midland Basin. Research on Wolfcamp Shale focuses a lot on sedimentology and petrophysics, including reservoir performance, wettability, pore structure, lithofacies, and permeability (Bangia, 1993; Li and Sheng, 2017; Casey et al., 2018; Ojha et al., 2018; Bhandari et al., 2019; Peng et al., 2019). However, most research in Wolfcamp Shale are from the Delaware Basin, and data from Midland Basin are limited; the pore structure of the Wolfcamp Shale in Midland Basin has not been well studied due to the limited core samples. In this dissertation, we intend to study the petrophysical properties of Wolfcamp Shale in Midland Basin with multiple well samples using multiple characterization methods. An elucidation of sedimentary and mineralogical impacts on Wolfcamp Shale and regional heterogeneity are the research goals in this chapter. The primary hypotheses are that: 1) sedimentary and deposition processes may control the clays and quartz percentage as well as their correlation to further control the pore size distribution and pore shape; and 2) Wolfcamp Shale in the Midland Basin is highly heterogeneous in terms of its petrophysical properties.

2. Geologic Settings

The Permian Basin, covering an area of more than 75,000 square miles, consists

of three sub-geologic components: Delaware Basin, Central Basin Platform, and Midland Basin (U.S. Energy Information Administration, 2018). The Midland Basin located at west of Texas covers an area with 250 miles wide and 300 miles long. In Early Paleozoic age (Early Ordovician to Late Mississippian), the Permian Basin was called Tobosa Basin which was an intracratonic subsidence on the Proterozoic basement. The Tobosa Basin lasted for 150 million years until a series of tectonic activities began, which was caused by the Ancestral Rock Mountain orogeny and the collision of Gondwana and Laurasia (Fairhurst et al., 2021). The sedimentary rocks in the Permian Basin are aged from Precambrian to Pennsylvanian with a maximum thickness over 29,000 ft in Delaware Basin (U.S. Energy Information Administration, 2018). The Wolfcamp Shale is deposited in all three sub-basins, and only the Midland Basin will be focused on in this dissertation. Siliceous and carbonate rock cycles caused by sea-level changes dominate the Wolfcamp Shale, and hemipelagic, sub-marine fan, and gravity flows are the common depositional systems (Hamlin and Baumardner, 2012; U.S. Energy Information Administration, 2020a, 2020b; Wilson et al., 2020). The Wolfcamp Shale has been stratified into four sections: Wolfcamp A, B, C, and D (Fig. 1) (U.S. Energy Information Administration, 2018; 2020a). Compared with Wolfcamp A & B with more petroleum reserves, Wolfcamp C & D have less important plays. Deep water and anoxic environment provided a good preservations for organic matters (OM) in Wolfcamp A & B, which made them as the hydrocarbon (HC) sources of many plays in the Midland Basin (Fairhurst et al., 2021).

3. Samples and Methodologies

A total of 14 core samples were retrieved from six wells near the west margin of the Midland Basin in Wolfcamp (A & B) (Fig. 2; Table 1). The depth range of the core samples is from 7600 ft to 10000 ft, and the linear dimensions of each irregularly-

sized core samples are 2-3 inches.

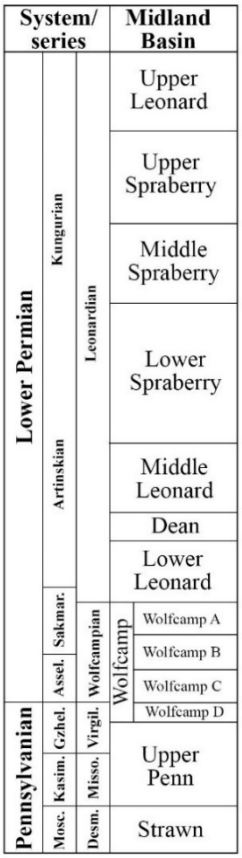

Figure 1. Stratigraphic column of Wolfcamp Shale

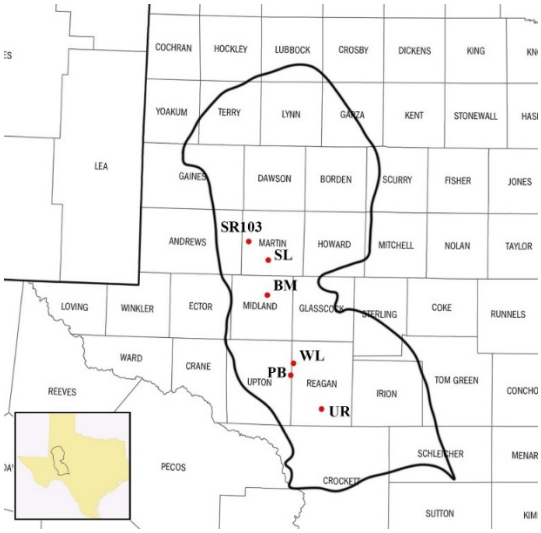

Figure 2. Location of six wells in the Midland Basin

The experimental methods on the Wolfcamp Shale are the same to the Woodford Shale which is shown in the Chapter II of this dissertation. Mineralogy and OM were tested by XRD and pyrolysis using the powder-sized samples. Thin section petrography and scanning electronic microscopy (SEM) were used in the observations

of lithofacies and grains. In SEM, energy-dispersive X-ray spectroscopy (EDS) mapping was also applied for elemental analyses. Wettability and fluid-rock interaction were tested by spontaneous imbibition and contact angle. The contact angle was measured on two polished surfaces, both parallel and transverse to the strata. Liquid immersion porosimetry (LIP) with DIW & 2DT, mercury intrusion porosimetry (MIP), gas physisorption (GP), and small angle X-ray scattering (SAXS) were used for pore structure characterization. Sample preparation and experimental settings are the same with the Woodford Shale. Spontaneous imbibition (SI) was performed in two different fluids of DIW and 2DT with two experimental durations of 24 hr and 8 hr. Three groups' experiments were performed, 24 hour in DIW, 8 hour in DIW, and 8 hours in 2DT, with both T and P directions tested in these groups. Sample SL-9449 is not included in SI because it is too fragile to be cut as cubes. In addition, SAXS was only tested for one spot per sample.

Table 1. Sample depth, TOC, and XRD mineralogy

Sample ID	Depth interval (ft)	Formation	TOC (wt.%)	Mineralogy (wt.%)				
				Quartz	Feldspar	Carbonate	Pyrite	Clays
BM-9403	9403.25-9403.6	A	3.00	29.2	2.3	46.4		22.1
BM-9675	9675.8-9676.1	B	3.39	48.3	11.3	12.2	5.6	3.1
PB-8668	8668.25-8668.6	A	1.01	11.3		71.6	0.6	16.4
PB-8780	8780-8780.25	B	3.96	54.8	10.3	20.7	4.2	13.7
PB-8889	8889.75-8890	B	3.33	70.9	10.6	0	2.2	16.3
PB-8907	8907.3-8907.63	B	2.38	39.9		29.1	3	28
SL-9268	9268.4-9268.75	A	1.52	67.6	12.6	10.2	4.8	4.8
SL-9449	9449.3-9449.7	B	2.91	17.6	3.0	0	5.0	70.2
SR103-9857	9857.3-9857.6	A	1.88	19.1	5.2	64.2		11.5
SR103-10003	10003.25-10003.5	B	1.07	35	13.1	3.9	3.8	44.2
UR-7630	7630.25-7630.52	A	1.12	33.5	16.3	3.7	3.5	43
UR-7872	7872-7872.25	B	2.03	27.8	17.1	30.3	1.3	23.5
WL-8649	8649.13-8649.42	A	1.08	14.0		83.9	1.0	1.1
WL-8839	8839.3-8839.67	B	3.73	38.2		9	6.2	38.2

4. Results

4.1. XRD and Pyrolysis

From XRD results, silicon (quartz and feldspar), carbonate and clays are the major mineral types in the Wolfcamp Shale. The ternary plot shows a wide clay percentage range in 13 samples from 0% to 73.8%, and most samples are silica-rich mudstones (Fig. 3). Samples from five out of six wells show an increase of quartz, feldspar, and clay percentages with depth, except for Well-UR which shows that the contents of quartz and clays decrease with depth.

The TOC values of 13 samples vary from 1.01 wt.% to 3.96 wt.% with an average of 2.32 wt.%, which is consistent with the data reported by Baumgardner et al (2014) (Table 2). The thermal maturity is not very high with $\%R_o$ varying from 0.760 to 0.958. T_{max} values are concentrated between 440°C to 451°C, and hydrogen index (HI) values vary from 35 to 245 mg HC/g TOC. The average of S1 is 1.34 mg HC/g sample in the range of 0.1-3.9 mg HC/g sample. S2 values are high with an average of 4.31 mg HC/g sample in the range of 0.39-8.15 mg HC/g sample, and the average of S3 is very low with 0.26 mg HC/g sample within 0.13-0.47 mg HC/g sample. The OM is composed of over 50% S2 and around 20% S1. These values of %Ro, T_{max}, and S1-S2-S3 values are similar to these reported by Zhang et al (2021).

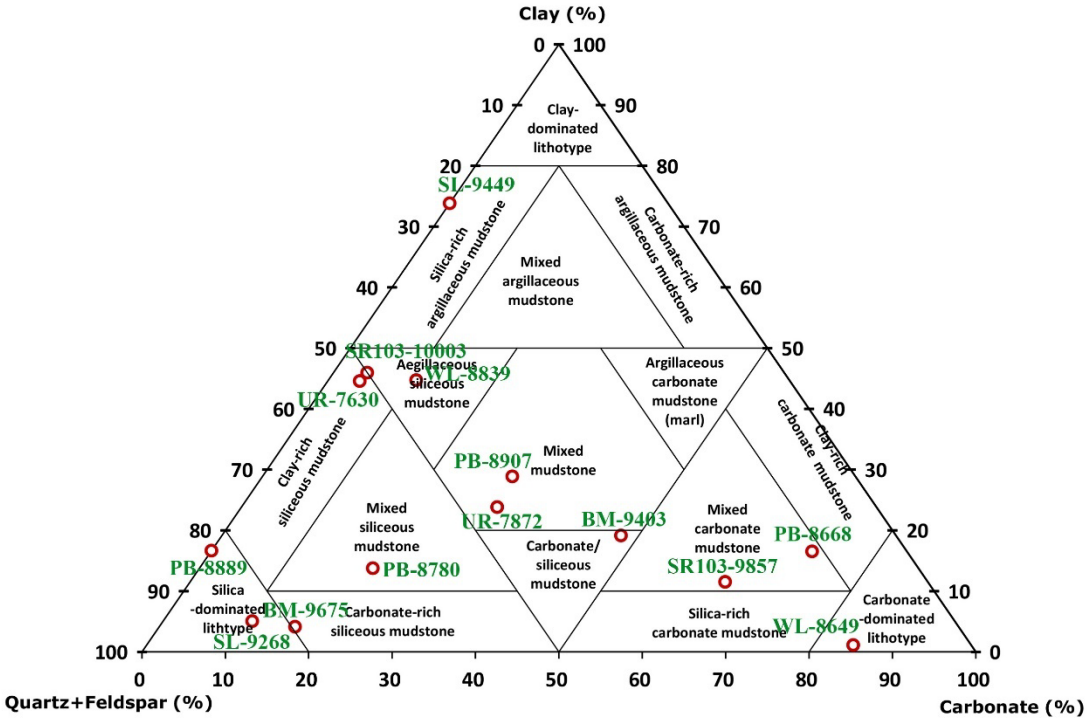

Figure 3. Ternary plot of lithofacies for the Wolfcamp Shale

Table 2. Pyrolysis results of the Wolfcamp Shale

Sample ID	TOC (wt.%)	R_o (%)	T_{max} (°C)	S1 (mg HC/g)	S2 (mg HC/g)	S3 (mg HC/g)
BM-9403	3.00	0.832	444	2	6.05	0.35
BM-9675	3.39	0.814	443	1.77	6.45	0.26
PB-8668	1.01	0.832	444	0.8	1.9	0.21
PB-8780	3.96	0.778	441	1.94	7.52	0.14
PB-8889	3.33	0.76	440	3.9	8.15	0.23
PB-8907	2.38	0.832	444	1.32	4.11	0.43
SL-9268	1.52	0.796	442	1.31	3.4	0.17
SL-9449	2.91	0.814	443	0.97	4.39	0.27
SR103-9857	1.88	0.832	444	0.89	3.76	0.28
SR103-10003	1.07	0.922	449	0.1	0.41	0.13
UR-7630	1.12	0.958	451	0.13	0.39	0.22
UR-7872	2.03	0.778	441	0.63	4.48	0.47
WL-8649	1.08	0.796	442	0.85	2.04	0.22
WL-8839	3.73	0.85	445	2.2	7.33	0.29

4.2. Thin section petrography and SEM

Calcite- and dolomite-replaced radiolarian is the common fossil in the Wolfcamp Shale (Wickard et al., 2016) (Fig. 4a, c, e, j & n). Some radiolarians are replaced by pyrite after the replacement of carbonate, as shown in thin section

petrography (Fig. 4). In five wells, except for Well-SL, fossils frequently appear are shallow depths. Quartz and feldspar grains which increase with depth pervasively exist in 13 samples with different clay contents. Quartz and feldspar grains have an average diameter of approximately 20 μm, except for SL-9268 which has the largest quartz/feldspar grain size with a diameter of 26 μm. In addition, layered structures are not obvious in thin section petrography.

In SEM images, clays, quartz, and carbonates, such as calcite and dolomite, are pervasively shown in the Wolfcamp Shale samples. Both interparticle and intraparticle pores are the common pore types, and OM pores are rare. The slit-shaped intraparticle pores in clay clusters are the most common intraparticle pores. However, the tight compaction in some samples, such as SL-9268, leads to compression and diminishing of the intraparticle pores in clay clusters (Fig. 5b). Carbonate grains and calcitic fossils are pervasive in the Wolfcamp Shale, and no pores exist inside of carbonate and quartz grains (Fig. 5g). Under SEM imaging, quartz grains from 13 samples roughly have two sizes, with the larger size at diameters of 10-30 μm and smaller one at 1-4 μm. The sheet-shaped clays are orientated and always exist around the calcitic fossils, carbonate grains, quartz, feldspar, and pyrite grains, forming “sandwich”-like structures (Fig. 5a, f, c, i, & k). Since clays are orientated, the layered structure could form in some samples, such as PB-8668 having clays-carbonate layered structures (Fig. 5c). Fractures are common in SEM images and often parallel with clay minerals (Fig. 5k). EDS elemental mapping in UR-7630 shows that elongate OM parallel with fracture (Fig. 5k). From BSE images, SR103-9857 shows OM dying at the end of one fracture (Fig. 5l).

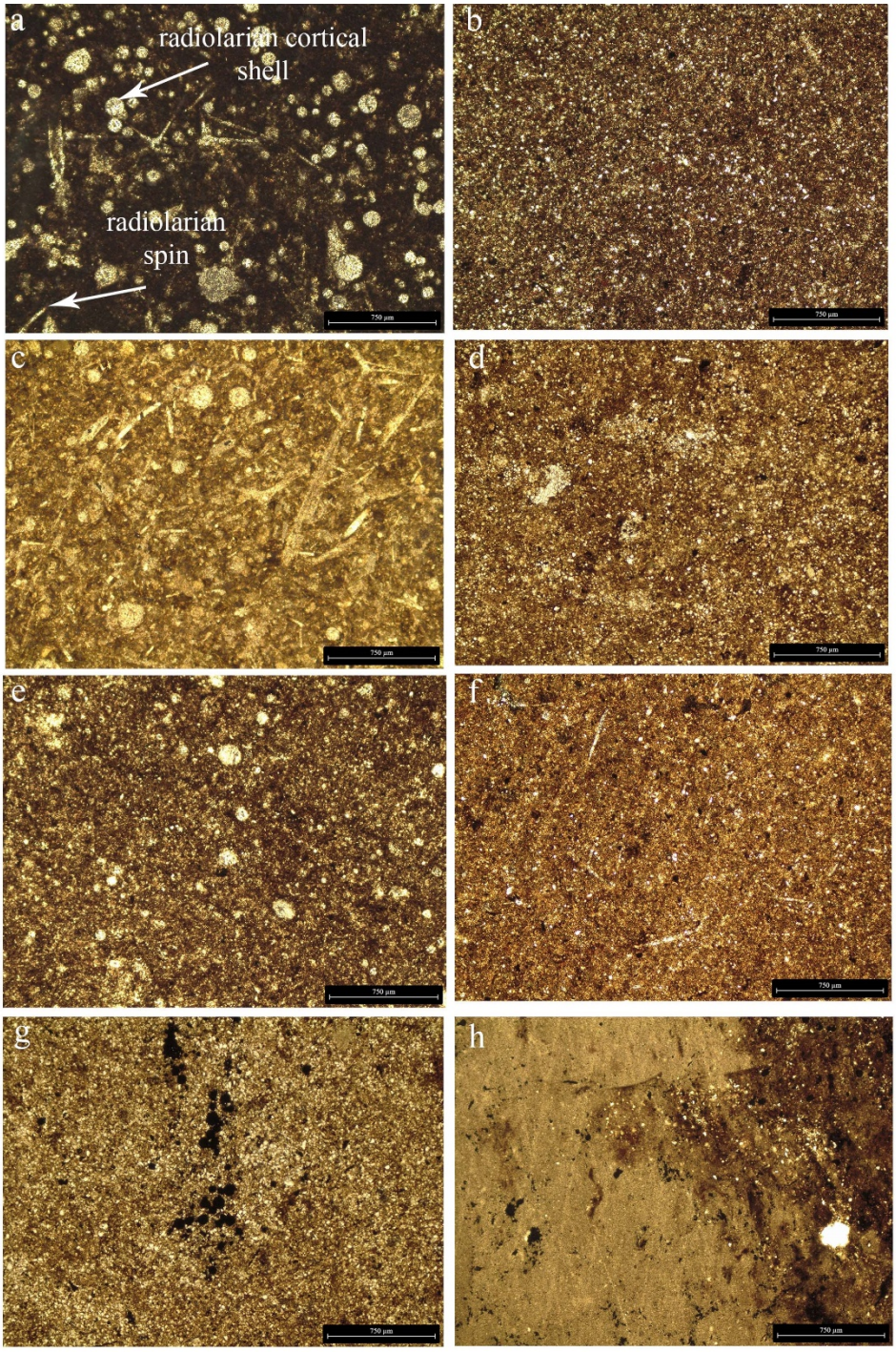
a
radiolarian cortical shell
radiolarian spin
b
c
d
e
f
g
h

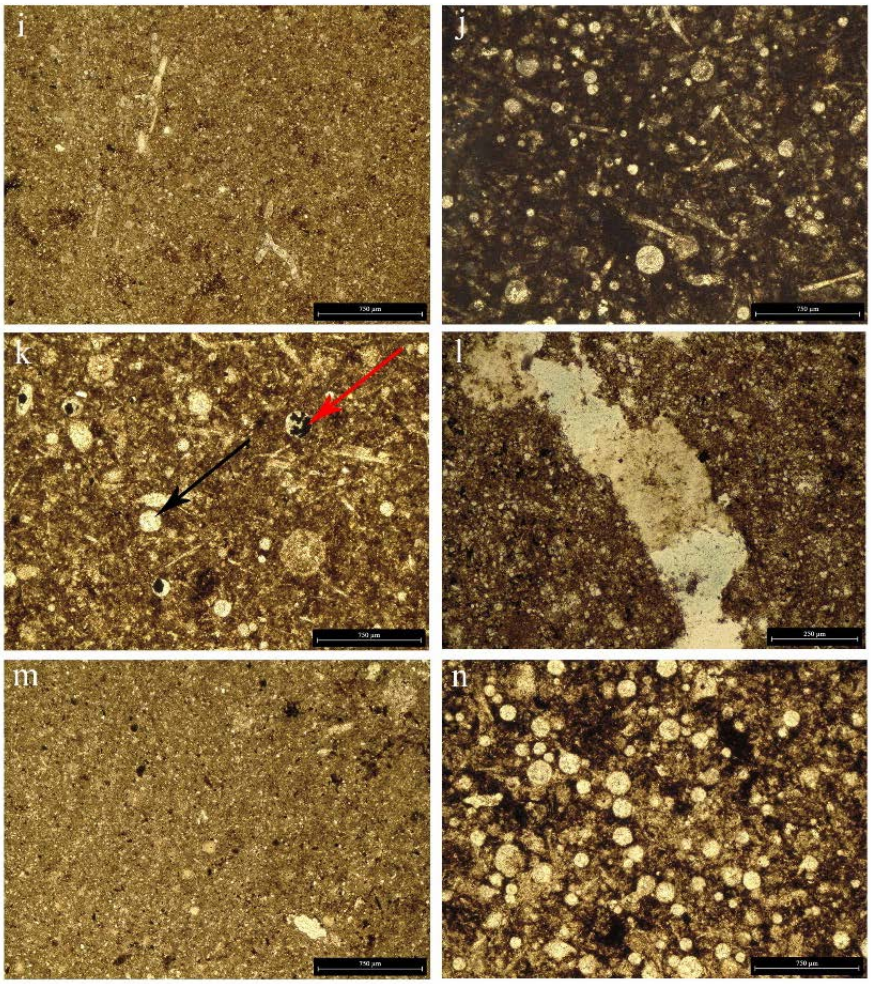

Figure 4. Thin sections of 13 Wolfcamp Shale samples; a. BM-9403; b. BM-9675; c. PB-8668; d. PB-8780; e. PB-8889; f. PB-8907; g. SL-9268; h. SL-9449; i. UR-7630; j. UR-7872; k. WL-8649; l. WL-8839; m. SR103-10003; n. SR103-9857.

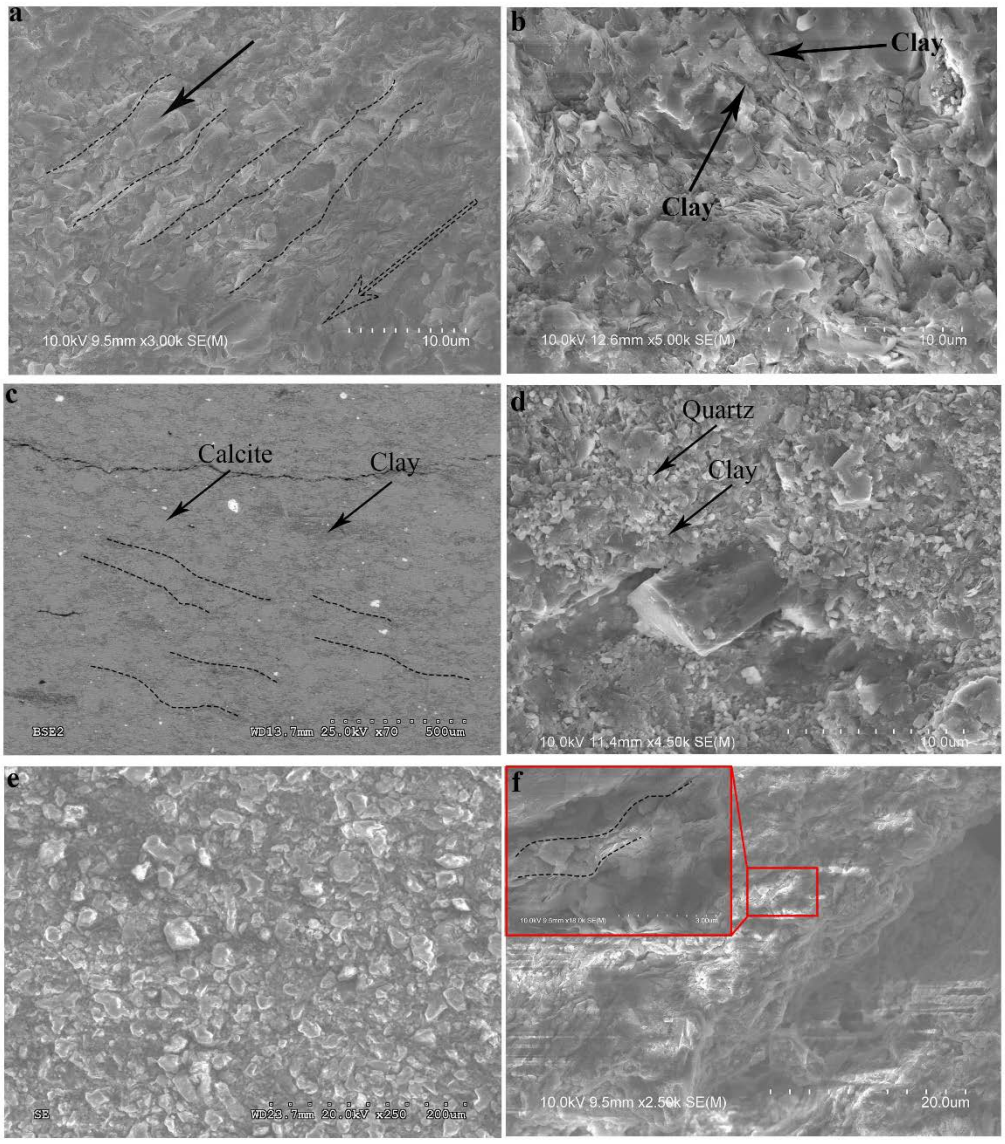
a
10.0kV 9.5mm x3.00k SE(M)
10.0um
b
Clay
Clay
10.0kV 12.6mm x5.00k SE(M)
10.0um
c
Calcite
Clay
BSE2
WD13.7mm 25.0kV x70
500um
d
Quartz
Clay
10.0kV 11.4mm x4.50k SE(M)
10.0um
e
SE
WD23.7mm 20.0kV x250
200um
f
10.0kV 9.5mm x2.50k SE(M)
20.0um

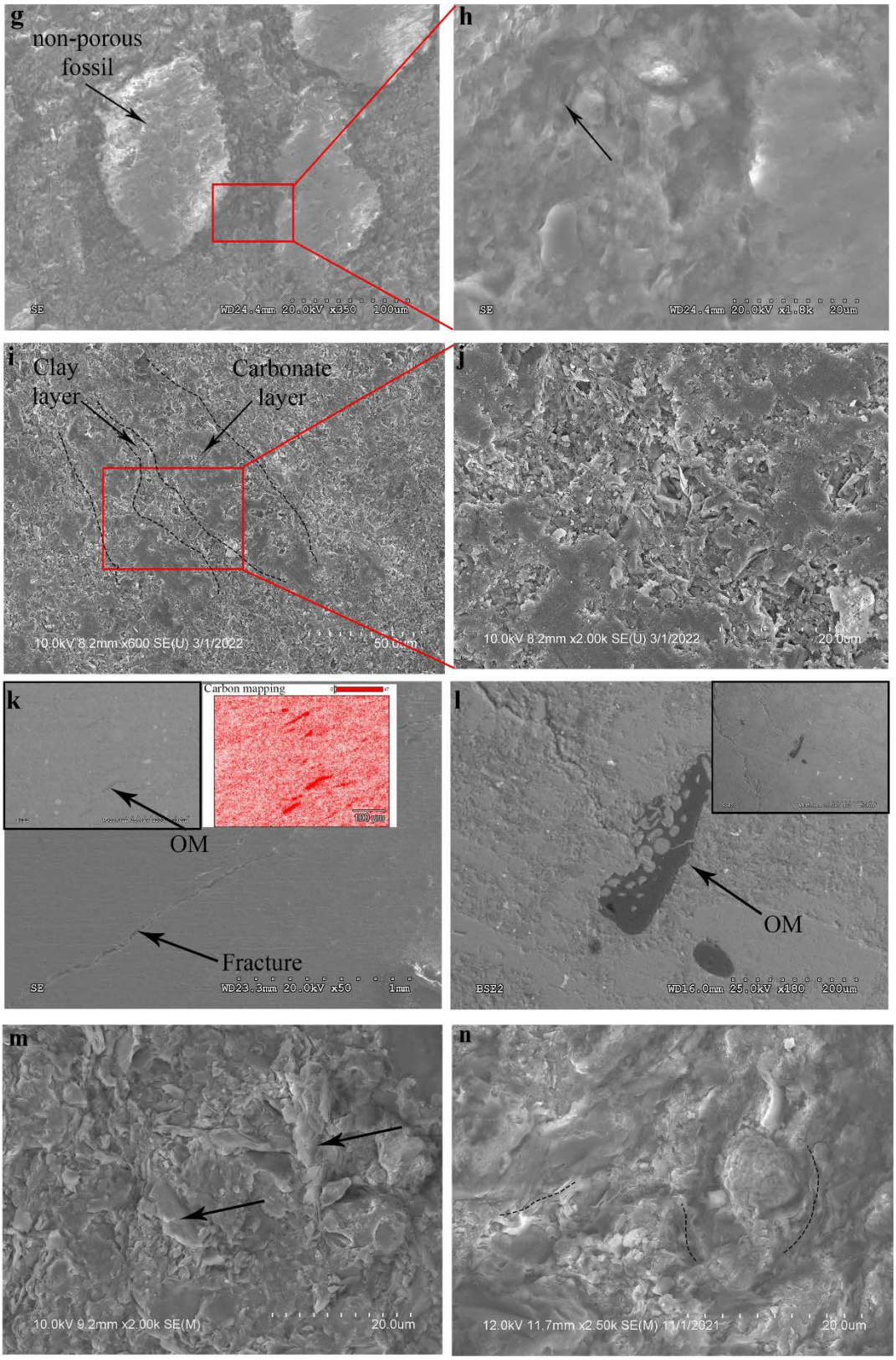
g
non-porous fossil
SE
WD24.4mm 20.0kV x350 100um
h
SE
WD24.4mm 20.0kV x1.8k 20um
i
Clay layer
Carbonate layer
10.0kV 8.2mm x600 SE(U) 3/1/2022
50.0um
j
10.0kV 8.2mm x2.00k SE(U) 3/1/2022
20.0um
k
Carbon mapping
100 um
OM
Fracture
SE
WD23.3mm 20.0kV x50 1mm
l
OM
BSE2
WD16.0mm 25.0kV x180 200um
m
10.0kV 9.2mm x2.00k SE(M)
20.0um
n
12.0kV 11.7mm x2.50k SE(M) 11/1/2021
20.0um

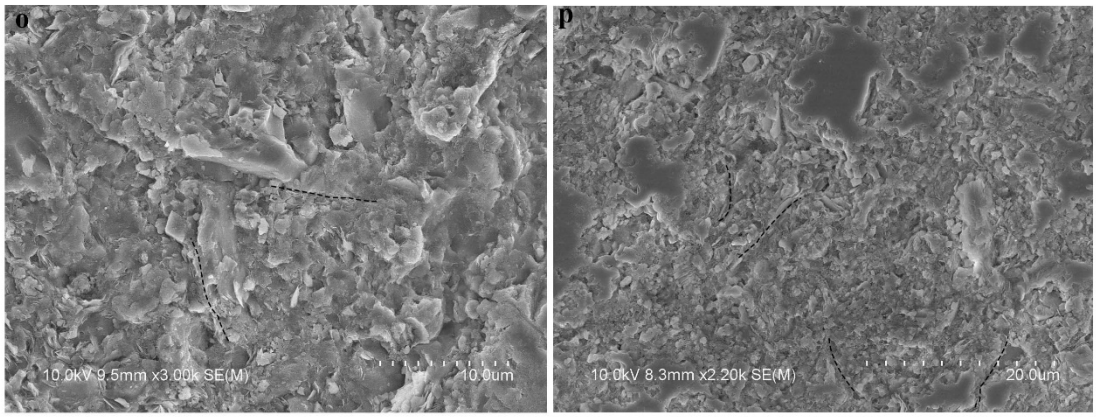

Figure 5. SEM images of the Wolfcamp Shale; a. UR-7630 shows the sandwich structure, dashed line shows clay positions and dashed arrow clay orientation direction; b. SL-9268 shows the squeeze of clays; c. PB-8668 shows interbedded clays and calcite; d. PB-8907;

4.3. Spontaneous imbibition and wettability

The volumes of imbibed liquid in three groups are higher in P direction than in T direction for both DIW and 2DT fluids with 24 hr and 8 hr duration, except for SL-9268, SR103-9857, and UR-7630 (Table 3). The imbibed volume of both liquids in two directions in SR103-9857 and UR-7872 are similar, and SL-9268 had higher imbibed volume in T direction. In DIW test with 24 hr duration, most samples have similar values of fitted imbibition slopes in P and T directions (Fig. 6; Table 4). In DIW with 8 hr duration, the imbibition slopes in T direction in some samples are higher than in P direction. In 2DT with 8 hr duration, samples in T direction started later than in P direction, and samples in T direction imbibed faster with greater imbibition slope values. By comparing the volume of imbibed liquids with DIW and 2DT in 8 hr, samples BM-9675 & SL-9268 and PB-8889 & PB-8668 imbibe similar volumes of two liquids in P and T directions. The other samples imbibe more DIW than 2DT. In summary, samples in T direction imbibe faster but less liquid than samples in P direction.

Contact angle was measured with DIW on polished sample surface. To better classify the wettability of the Wolfcamp Shale samples, we plot the contact angle again the wettability index of water which is the ratio of imbibed DIW volume over total

imbibed volume of DIW and 2DT with 8 hr duration (Fig. 7) (Wang et.al., 2020). Most samples are intermediately mixed-wet. BM-9675, UR-7872, and WL-8839 are strongly mixed-wet, SR103-10003 is strongly water-wet, and SR103-9857 is slightly mixed-wet with a water-wet preference.

Table 3. Imbibed volume of DIW and 2DT fluids with respect to P and T testing directions

Sample ID	Imbibed volume (cm^3)					
	8 hr 2DT		8 hr DIW		24 hr DIW	
	T	P	T	P	T	P
BM-9403	0.005	0.018	0.010	0.012	0.018	0.020
BM-9675	0.010	0.023	0.014	0.023	0.032	0.038
PB-8668	0.009	0.009	0.009	0.011	0.016	0.018
PB-8780	0.028	0.047	0.024	0.055	0.046	0.055
PB-8889	0.009	0.009	0.009	0.009	0.018	0.018
PB-8907	0.024	0.070	0.030	0.067	0.054	0.072
SL-9268	0.028	0.023	0.030	0.023	0.045	0.034
SL-9449						
SR103-9857	0.008	0.006	0.012	0.011	0.018	0.017
SR103-10003	0.005	0.033	0.028	0.049	0.043	0.052
UR-7630	0.002	0.010	0.011	0.011	0.019	0.018
UR-7872	0.013	0.031	0.017	0.037	0.036	0.046
WL-8649	0.004	0.011	0.006	0.012	0.012	0.020
WL-8839	0.038	0.098	0.035	0.086	0.061	0.092

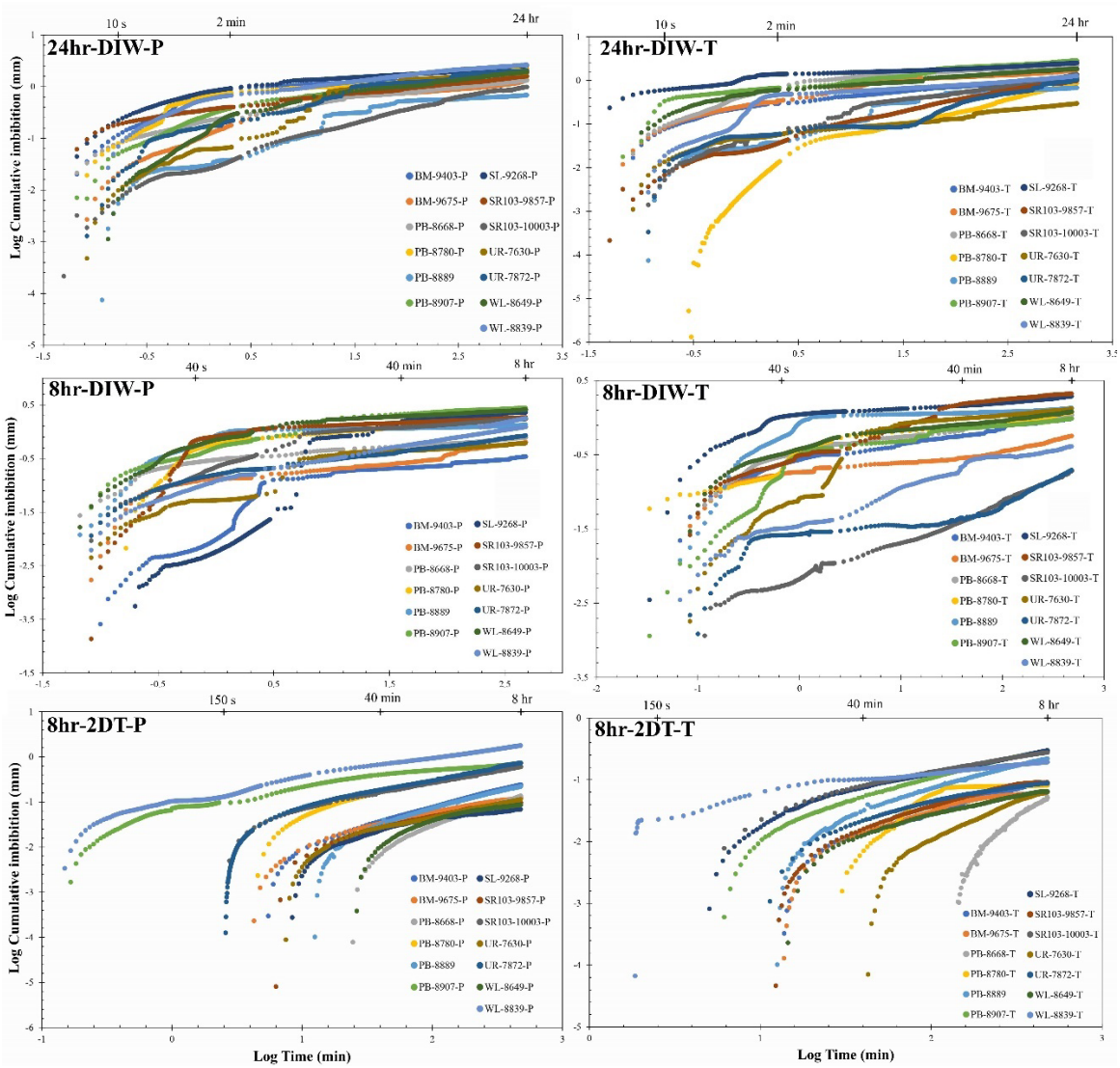

Figure 6. SI plots of 13 samples with DIW and 2DT

Table 4. Imbibition slopes of DIW and 2DT fluids and P & T testing directions .

Sample ID	Fitting slope					
	8 hr 2DT		8 hr DIW		24 hr DIW	
	T	P	T	P	T	P
BM-9403	0.853	0.752	0.221	0.185	0.137	0.110
BM-9675	0.233	0.480	0.279	0.268	0.200	0.182
PB-8668	2.303	0.727	0.185	0.146	0.138	0.182
PB-8780	0.053	0.576	0.131	0.165	0.518	0.224
PB-8889	0.805	0.805	0.032	0.032	0.144	0.144
PB-8907	0.631	0.233	0.168	0.114	0.221	0.108
SL-9268	0.551	0.322	0.084	0.118	0.126	0.215
SL-9449						
SR103-9857	0.714	0.286	0.138	0.120	0.150	0.215
SR103-10003	0.513	0.530	0.621	0.134	0.370	0.481
UR-7630	1.202	0.590	0.110	0.112	0.254	0.201
UR-7872	0.465	0.536	0.601	0.261	0.468	0.172
WL-8649	0.603	0.560	0.140	0.110	0.179	0.221
WL-8839	0.287	0.160	0.222	0.375	0.139	0.136

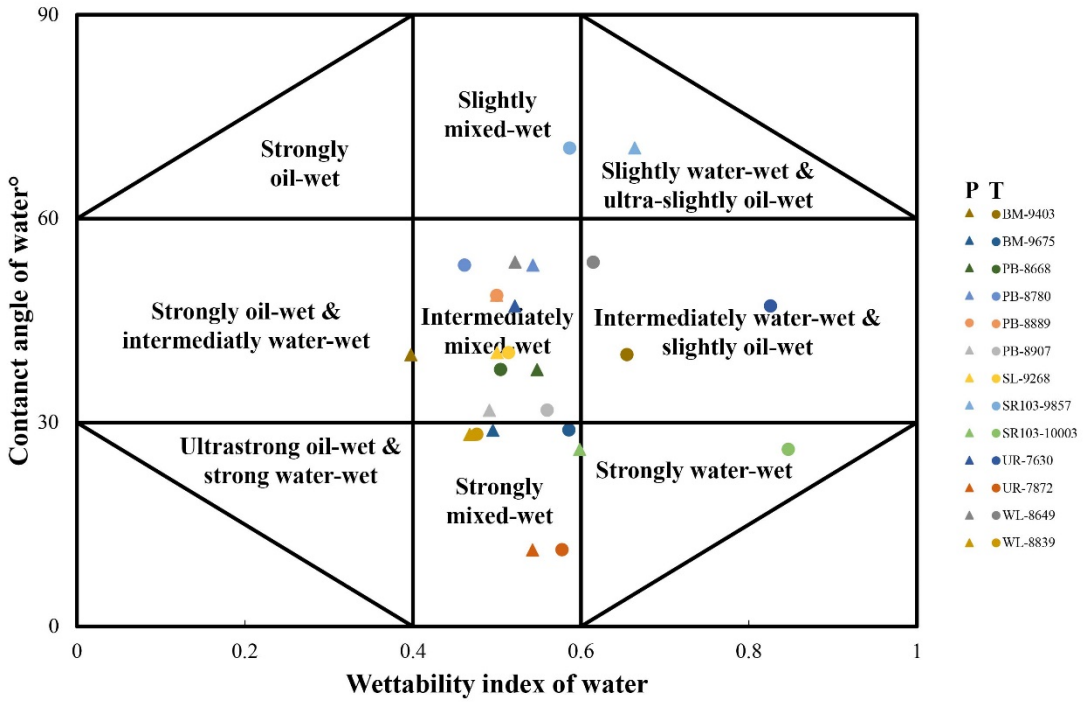

Figure 7. Wettability of 13 Wolfcamp Shale samples with contact angles in P (triangles) and T (circles) direction surfaces

4.4. Vacuum-assisted LIP and MIP tests

The porosities by LIP-DIW vary in 1.30% to 9.61% with an average of 4.73%. The porosities by LIP-2DT are similar to the LIP-DIW with an average of 4.69% in the range of 1.45% to 8.58%. Most samples have similar porosity in DIW and 2DT, except for PB-8889 that has a high 2DT porosity (Table 5).

The average porosity obtained from MIP method for 13 samples is 3.84% in the range of 0.296% (SR103-9857) to 7.86% (WL-8839). The pore volume varies with an average value of 0.018 cm^3/g in the range of 0.001 cm^3/g (SR103-9857) to 0.044 cm^3/g (SR103-10003). Fig. 8 shows pores with diameters of 4 nm and 5 nm dominate the samples that have increments smaller or equal to 1 mm^3/g. For samples with large increments, such as PB-8780, PB-8889, PB-8907, and WL-8839, pores with greater diameter at 5-10 nm dominate the samples. Pore sizes over 10 μm are also present in most samples. Pore sizes in 13 samples within 10 nm in diameters contribute over 70% of the total pore volume, except for UR-7630 and SL-9449 which only contribute 50%.

The range of pore specific surface area is 0.778 m^2/g to 24.0 m^2/g with an average of 9.60 m^2/g. Pore sizes within 10 nm provide over 90% of the pore area. For most samples, 3-5 nm-sized pores are the major contributor to pore area, while pore sizes over 20 nm almost have no contribution to pore area. Four samples, PB-8780, PB-8889, PB-8907, and WL-8839, with large cumulative pore volume and pore area create a gap in two plots (Fig. 8). The porosities of these four samples are the greatest among 13 samples, and the porosities of other samples are concentrated at 2-3%.

Table 5. Porosity results from LIP, MIP, GP, and SAXS methods.

Sample ID	Porosity (%)				
	LIP DIW	LIP 2DT	MIP	GP	SAXS
BM-9403	2.61	3.30	1.96	2.96	3.65
BM-9675	4.13	4.84	2.98	4.89	4.06
PB-8668	1.94	2.19	1.40	2.31	2.25
PB-8780	9.22	8.47	7.28	7.30	4.21
PB-8889	2.56	5.97	6.90	4.46	5.48
PB-8907	7.98	6.74	6.60	6.67	4.02
SL-9268	4.32	4.29	3.37	3.60	3.61
SL-9449			4.60	8.68	4.42
SR103-9857	1.30	1.45	0.30	1.35	2.40
SR103-10003	8.94	6.10	4.22	4.82	2.48
UR-7630	1.92	1.71	1.10	2.16	2.94
UR-7872	5.08	4.77	2.94	4.70	4.05
WL-8649	1.95	2.60	2.24	2.29	2.53
WL-8839	9.61	8.58	7.86	7.43	8.50

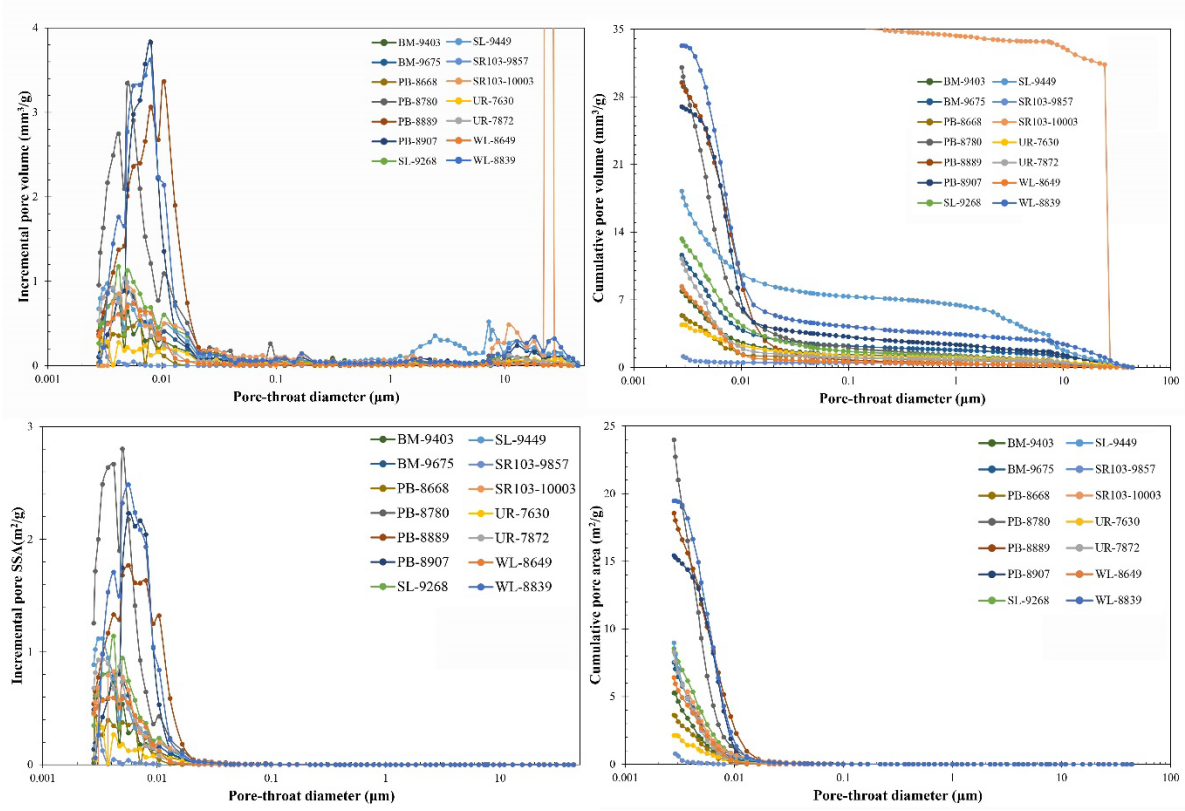

Figure 8. Pore size distribution and pore surface area distribution obtained from MIP methods

4.5. Gas physisorption

GP tests use granular samples at 500-841 μm, and the porosity calculated with MIP-derived bulk density (for 1 cm sided cubic sample) varies from 1.35% to 8.68%, with an average of 4.56%. The pore size distributions (PSD) of most samples are dominated by pores with diameters at 2-3 nm (Fig. 9a). Samples BM-9675, SL-9449, and SR103-10003 have unimodal distributions with peaks at 3 nm, 2.7 nm, and 2.2 nm, respectively. For the cumulative pore volume, SL-9449 has the largest pore volume of 0.034 cm^3/g, and SR103-9857 has the smallest value of 0.005 cm^3/g (Fig. 9b).

The average BET surface area ranges from 1.46 to 23.3 m^2/g with an average of 8.46 m^2/g, with the largest for sample SL-9449 and the smallest for SR103-9857. The isothermal plots of adsorption and desorption of 14 samples can be classified into two groups based on the shape of hysteresis loops (Fig. 10). Group 1 consists of samples BM-9403, BM-9675, SR103-9867, SR103-10003, SL-9268, SL-9449, and UR-7630

with a sudden decrease at relative pressure of 0.5 in the desorption branch. Group 2 consists of samples PB-8668, PB-8780, PB-8889, PB-8907, UR-7872, WL-8649, and WL-8839. The desorption branch in Group 2 is similar to Group 1, but before the sudden decrease, there was a gentle decrease between relative pressures of 0.5 and 0.7.

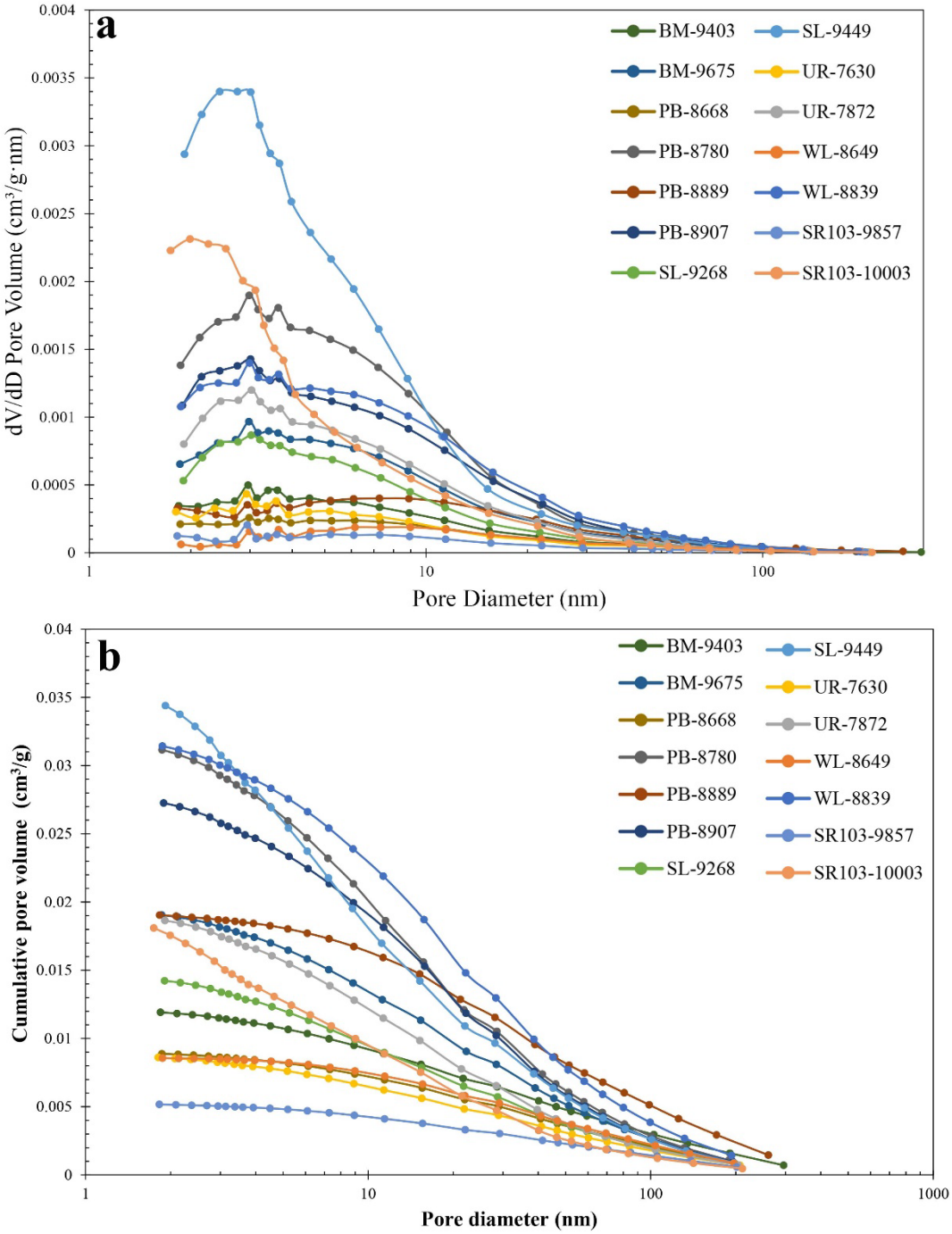

Figure 9. a. GP incremental pore volume distribution; b. GP cumulative pore volume

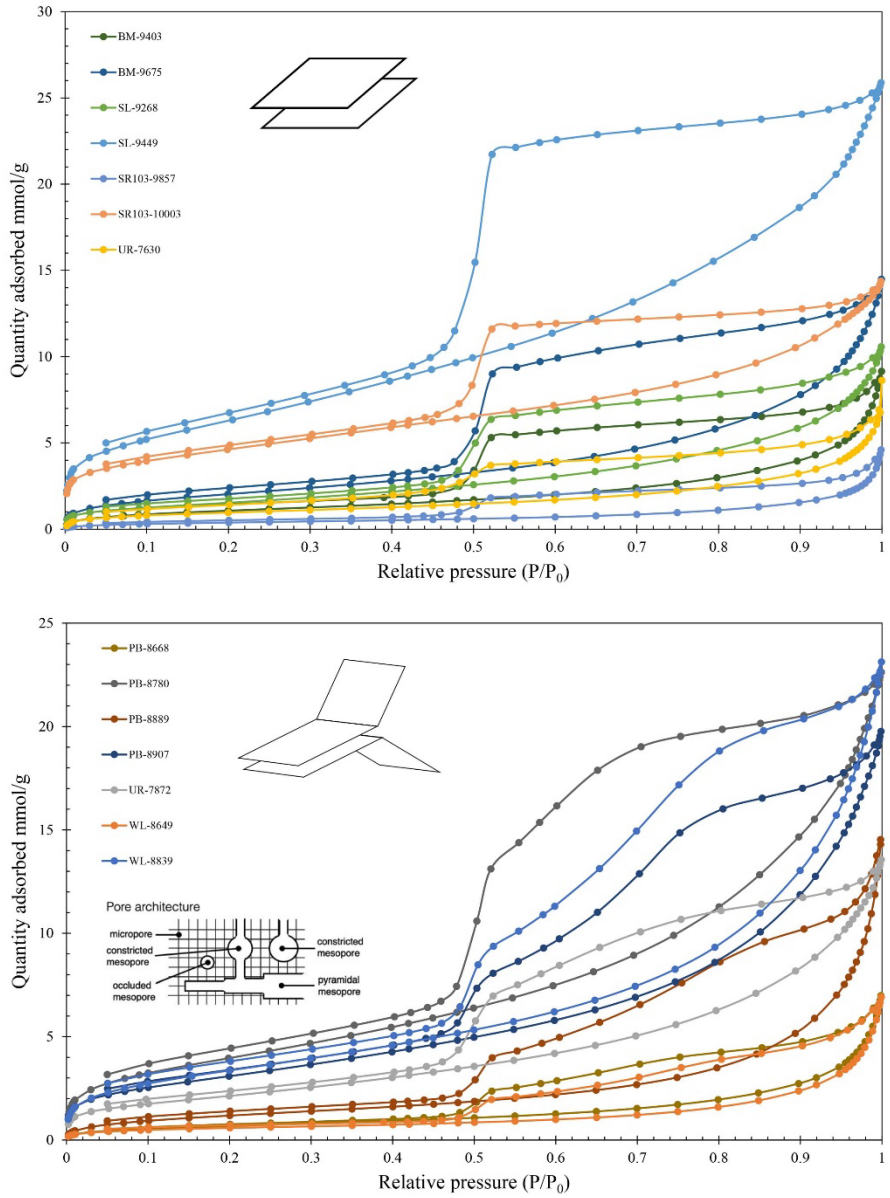

Figure 10. GP hysteresis loops of 13 Wolfcamp Shale samples (modified from Taheri et al., 2021)

4.6. SAXS tests

The porosity range of SAXS in 13 samples is 2.25% (PB-8668) to 8.50% (WL-8839) with an average of 3.90%. In the incremental porosity distribution plot, the samples are dominated by multiple pore sizes (Fig. 11a-b). Multiple peaks appear at the ranges of mesopores and macropores. Peak clusters formed by these multiple peaks show a dominance of mesopores and macropores in the Wolfcamp Shale. According to the different pore size dominance in PSD data, these 13 samples can be divided into

two groups. Group 1 is dominated by mesopores at 5-20 nm and 50 nm with a minor amount of pores at 2-4 nm (Fig. 11a). Group 2 is dominated by macropores of 100-600 nm with a minor contribution of micropores at 2-3 nm (Fig. 11b). The average specific surface area (SSA) is 36.4 m^2/g in the range of 14.1 m^2/g to 59.0 m^2/g (Fig. 11). As shown in Fig. 11c, micropores at 2 nm and mesopores at 4-20 nm contribute to the cumulative SSA. Over 50% of the SSA is provided by pores smaller than 10 nm, and over 90% by pores smaller than 50 nm.

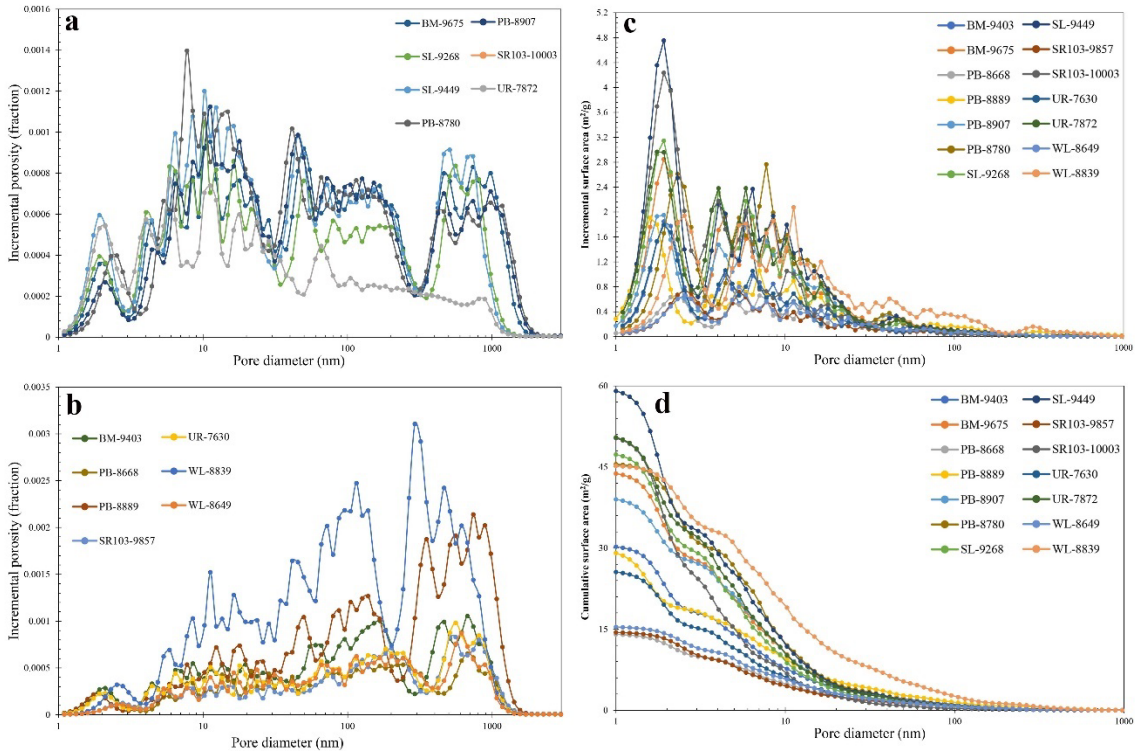

Figure 11. Pore volume distribution and pore surface area distribution of SAXS results: a. Group 1 pore volume distribution; b. Group 2 pore volume distribution; c. Incremental pore surface area distribution; d. Cumulative pore area.

5. Discussion

5.1. OM Maturity, mineralogy, and visualization analysis

The data from Rock-Eval pyrolysis indicate that the Wolfcamp Shale is both gas and oil prone and in oil window with an averaged HI value of 225 mg HC/g TOC (Fig. 12) (Waples, 2013; Jackson et al., 1985). An increase of HI with TOC contents indicates that S2 increases with TOC values, because HI is calculated from S2. The

increase of S2 with TOC indicates that the kerogen ready for hydrocarbon production compose the OM in the Wolfcamp Shale (Peters, 1986). This high S2 content also shows the high potential of HC generation in the Wolfcamp Shale though the maturity is not very high (Peters, 1986). The averaged $\%R_o$ value of 0.828% also proves the low maturity of the Wolfcamp Shale. Mixed kerogen Type II and Type III point out that the kerogen in the Wolfcamp Shale was originated from both marine and terrestrial environments, while only UR-7630 and SR103-10003 are Type III originated from terrestrial deposition (Fig. 13). Therefore, the Wolfcamp Shale in the Midland Basin has a high potential for hydrocarbon generation.

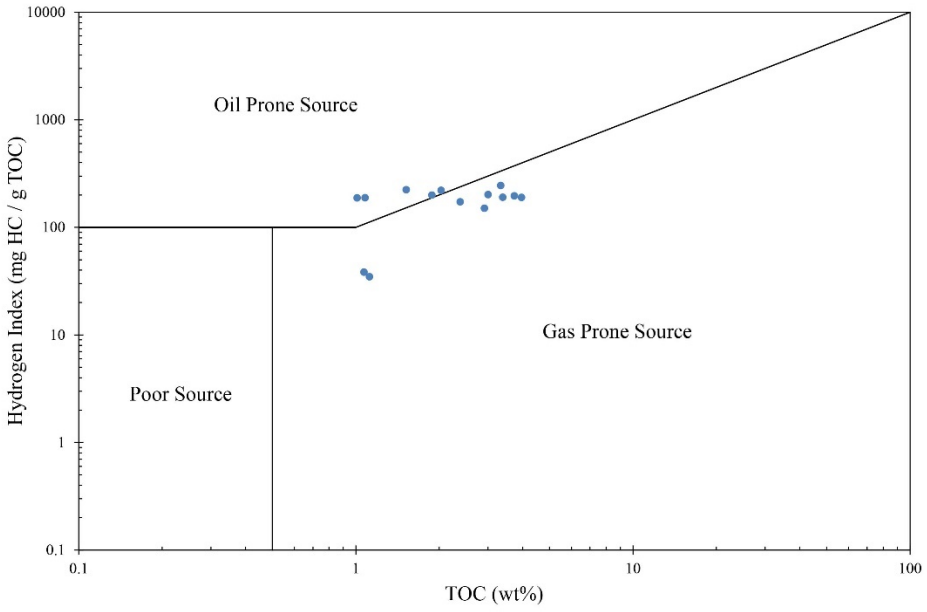

Figure 12. HI vs. TOC plot of the Wolfcamp Shale.

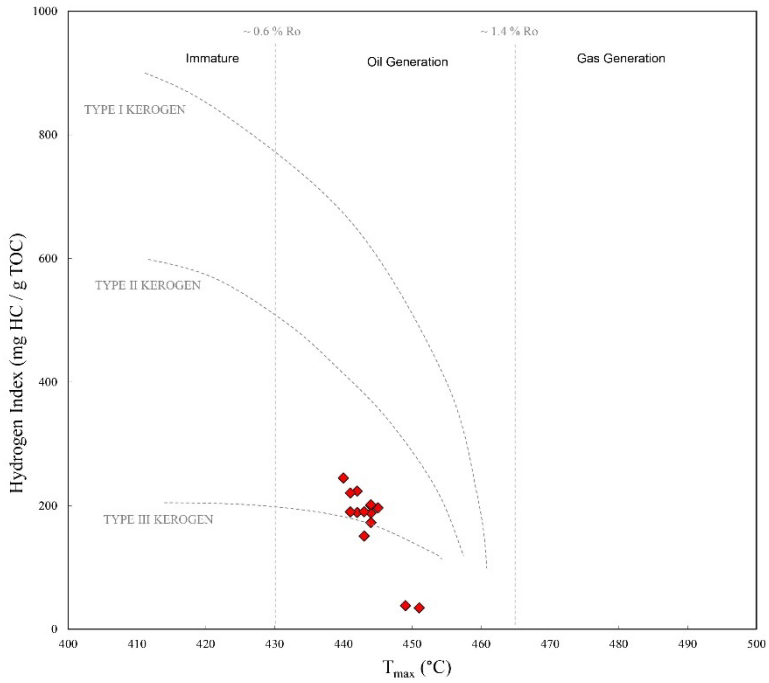

Figure 13. Kerogen type and maturity of 13 Wolfcamp Shale samples.

Through the thin-section petrographic observations, two lithofacies are identified in 13 Wolfcamp Shale samples, mudrock and calcareous mudrock which could be formed in a hemiplegic environment (Hamlin and Baumgardner, 2012). The lithologic ternary plot of XRD data shows that 13 Wolfcamp Shale samples are siliceous- and carbonate-dominated mudstone with clay contents less than 50% (except for SL-9449), which is consistent with the data published by Hamlin and Baumgardner (2012) (Fig. 3). According to XRD data (Table 1), clay contents decrease as carbonate contents increase. “Quartz + feldspar” and carbonate contents are various, which may affect the porosity in the Wolfcamp Shale. Porosity tested by LIP and MIP methods show a good consistency, which indicates good accuracy of test results from both methods. Porosity slightly increases with siliceous (quartz + feldspar) content and decreases with carbonate contents (Fig. 14). Carbonate cement filling interparticle pores could be the reason of porosity decrease with carbonate contents increase (Chen et al., 2017). For clay contents, the trend is unclear; however, if we include the eight samples from the Woodford Shale, then the trend will be an increase first then followed

with a decrease after 30% of clay contents (Fig. 14). In consideration of the TOC values, TOC tends to increase with porosity (Fig. 15a). But there is not a relationship between TOC and “quartz + feldspar” or clays contents. TOC shows a slight decrease with an increasing carbonate contents (Fig. 15b). Therefore, we speculate that OM concentration has no preference on mineralogy but pore space. The higher the porosity is, the more OM is concentrated in the samples.

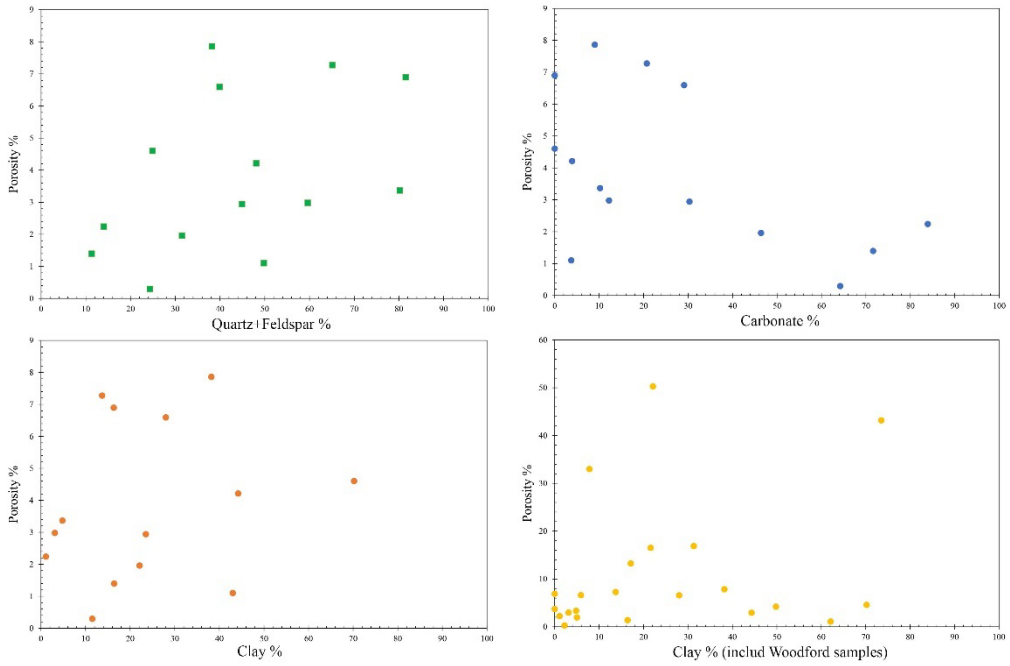

Figure 14. Plots of “quartz + feldspar”, carbonates, and clays with MIP porosity.

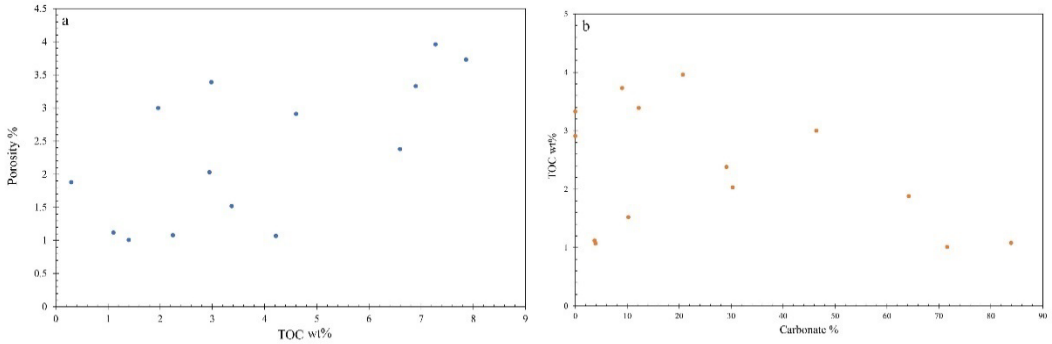

Figure 15. a. Plot of MIP porosity vs. TOC; b. plot of TOC vs. carbonates.

As shown in SEM images, grain sizes are in 10-30 μm which are consistent with the results from thin section petrography. Smaller grain sizes also exist in some samples. The quartz grains at sizes of 1-2 μm are aggregated and surrounded by clay clusters in

PB-8907, which could be resulting from the illitization of smectite under temperatures over ~85°C (Peltonen et al., 2009). The illitization of smectite is common in clay-rich sediments which could make clays more orientated. Temperature is not the only condition of illitization, and potassium is also required (Equation 1). The major source of K^+ is K-feldspar, such as albite (Thyberg et al., 2010; Peltonen et al., 2009).

$$\text{Smectite} + K^+ = \text{Illite} + \text{Silica} + H_2O \qquad \text{(Equation 1)}$$

However, the XRD data show that sample PB-8907 does not have albite; therefore, the fluid with potassium could be from other source(s) (Awwiller, 1993).

From the combined results of SEM images, XRD analyses, and porosity from MIP, orientated clay clusters could contribute to the porosity with clay contents at 20-30% (Fig. 14). In SEM images for UR-7630 and PB-8907, grains are sandwiched between clay clusters (Fig. 5a; 5f). Though the clay is soft, it is not soft enough to fully cover the grains. Therefore, the interparticle pores are created. Such "sandwich" structure is pervasive in the Wolfcamp Shale. The presence of clays may help to generate fractures and further increase the porosity, since most fractures are parallel to clays (Fig. 5k). Fractures could be the pathway for hydrocarbon migration, and intraparticle pores in clays could provide space for migrated hydrocarbons for samples UR-7630 and SR103-9857 (Fig. 5k; 5i). However, when clay contents are larger than 40%, the porosity will dramatically decrease (Fig. 14). A diminishing of pores with more clays under compaction and less support from quartz could be the reason for porosity decrease (Crawford et al., 2008).

Carbonate contents show a negative correlation with porosity values (Fig. 14), because the non-porous calcitic fossils cannot provide pore space and also carbonate cements can block the pores (Fig. 5g). Intraparticle pores in clays surrounding the fossils and interparticle pores between clay and quartz or feldspar provide a primary

pore volume in samples dominated by calcitic fossils (Fig. 5h). The rigid quartz and feldspar grains help to create pore spaces (Zhao et al., 2017; Desbois et al., 2009). The interparticle pores formed between rigid grains probably were prevented from a compaction. Comparing the samples that are rich in carbonate, the more quartz the sample contains, the higher porosity it may have (Tables 1 & 5; Fig. 14). However, not all the pores can be protected by rigid grains. In sample SL-9268, the intraparticle pores in clay clusters seem to be squeezed down by tightly compacted grains, which could be the reason of low porosity in this quartz-dominated sample (Fig. 5b).

5.2. Pore structure characterization

The GP hysteresis loops show two groups for 13 samples, according to the five types of hysteresis loops classified by De Boer (1958). Group 1 is type B with slit-shapes formed by two parallel sheets (Fig. 16). Group 2 seems like the combination of type B and type D. Compared with data of Taheri at al. (2021), such loop could be caused by pyramidal mesopores or the combination of both slit- and wedge-shaped pores (Fig. 10). The large BET surface and small pore volume in GP tests indicates that the average pore size should be small. From Fig. 9a, mesopores with diameters of 3-4 nm is the major pore size. In Fig. 17, the volume of micropores and mesopores show linear positive relationships with BET surface area, in which mesopores are the primary BET surface area contributor. Therefore, from GP results mesopores contribute both to pore volume and pore surface area.

From incremental pore volume plot of MIP tests, mesopores of 3-5 nm and 7-10 nm are the major pore types, which shows a good consistency with GP results (Fig. 8). The bimodal distribution from MIP may indirectly prove the existence of wedge-shaped pores with two dominant sizes, such as in samples PB-8889 and PB-8907 which

have wedge-shaped pores dominated by 3-4 nm and 7-10 nm in diameters. The pores >10 μm may be caused by fractures which are common in SEM images. In Fig. 8, samples with large porosities tend to have greater pore volume increment in mesopores and high cumulative pore surface area. MIP data indicates that mesopores provide both cumulative pore volume and pore surface area. SAXS results show a dominance of mesopores at 10 nm and macropores at 100 nm, which are consistent with MIP data. Because of the underestimation of pore size in narrow mesopores (<10 nm) by 20-30% in GP method, the peaks around 3 nm in GP's incremental pore volume plot could be corrected to 4 & 5 nm (Thommes et al., 2015). The corrected peaks and peaks over 10 nm correspond to the results from MIP and SAXS methods.

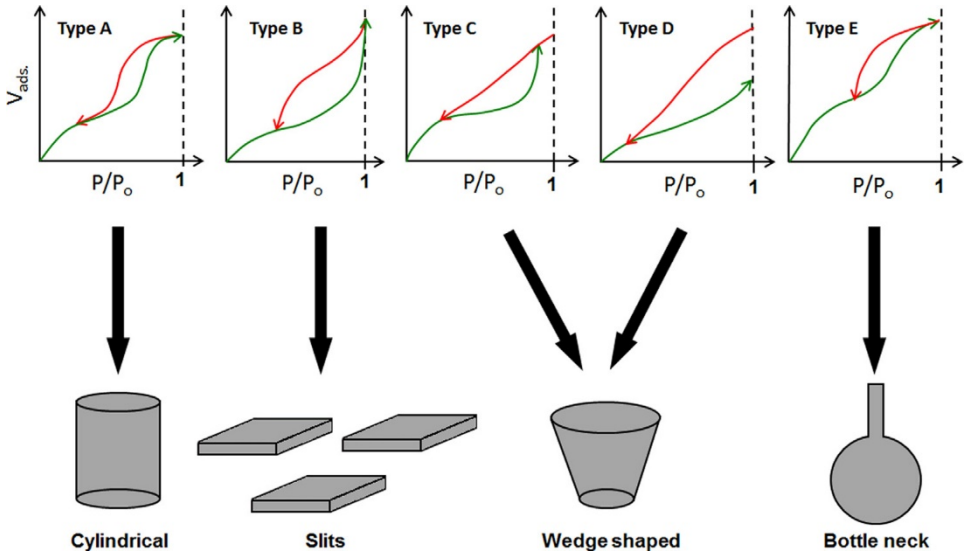

Figure 16. GP hysteresis loops with corresponding pore shapes (modified from Labani et al., 2013).

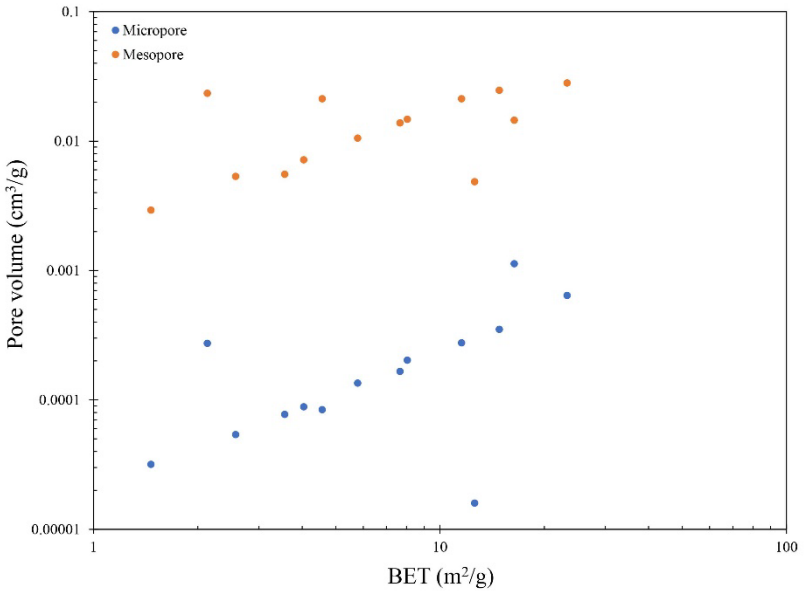

Figure 15. BET vs. pore volume from GP results.

Samples with slit-shaped pores from the GP method highly overlap with those from SAXS which are dominated by mesopores, and these samples are BM-9675, SL-9268, SL-9449, and SR103-10003. Coupling with the intraparticle pores in clays in SEM images, we believe that slit-shaped pores generated by clay minerals could contribute to the mesopores in the Wolfcamp Shale (Fig. 5b; 5m). Samples dominated by mesopores and macropores from SAXS results show slit- and wedge-shaped pores in the GP method. Coupling the pore shape info from GP and pore size data from MIP methods, these 13 samples could be assigned into four types: 1) slit-shaped mesopores (BM-9675, SL-9268, SL-9449, and SR103-10003), 2) slit-shaped macropores (BM-9403, SR103-9857, and UR-7630), 3) wedge-shaped mesopores (PB-8780, PB-8907, and UR-7872), and 4) wedge-shaped macropores (PB-8668, PB-8889, WL-8649, and WL-8839). Samples with slit-shaped pores tend to have pore sizes of 4-5 nm, in compassion with samples with wedge-shaped pores at 8-10 nm.

Samples with slit-shaped pores are featured by a large percentage of fossils, layered structure, and less dominance of carbonates. Except for the carbonates from the calcitic fossils, most carbon will act as a cement to block and seal pores. The carbonates

in BM-9403 and SR103-9857 mainly come from the calcitic radiolarian fossils that only cortical shell preserved (Fig. 4a; 4n). Plate-shaped clay minerals and spherical quartz grains/cortical shells tend to deposit as "sandwich" structure in which quartz grains stuck between parallel clay clusters (Fig. 18) (Eckert et al., 2022; Seelen et al., 2018). Finally, the clay minerals are compacted as parallel bundles to produce slit-shaped pores (Fig. 5a, b, f, j, m). In SEM images, samples BM-8675, SL-9268, SL-9449, SR103-10003, and UR-7630 have layered structures which may be inherited from deposition. “Sandwich” structure is common in these samples, such as UR-7630 (Fig. 5a). In lithologic ternary plot, these five samples are shown near the line of clay and “quartz + feldspar” as the end members, which indicates the lack of carbonates (Fig. 3). A large amount of rigid quartz grains could protect the pores from over-compaction in quartz-dominated samples.

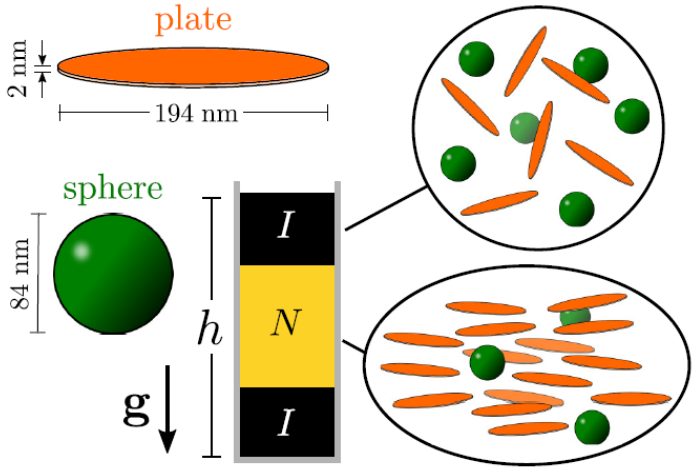

Figure 16. Stacking patterns of plate and sphere mixture (modified after Eckert et al., 2022).

Being compared with samples with slit-shaped pores, the samples with wedge-shaped pores have less extent of clay orientation and more carbonate cementations. Clay orientations in PB-8780 and UR-7872 are not very well and wedge-shaped mesopores could form in such disordered clay intraparticle and interparticle pores (Fig. 5n-o). In PB-8907, quartz grains with diameters of 500 nm appear in clay bundles,

which could create wedge-shaped pores. These nano-quartz grains could be the by-product of the transition of smectite to illite (Fig. 5d) (Thyberg et al., 2010). Compared with SL-9268 with dominant large grain sizes, both samples PB-8907 and SL-9268 are dominated by mesopores. This may indicate that grain size may not be the primary factor affecting pore sizes.

The macropores and wedge pore shape in samples PB-8668, PB-8889, WL-8649, and WL-8839 could be caused by carbonate cement and clay orientation. PB-8668 and WL-8649 are dominated by carbonates with over 70% in contents. However, in thin sections, the calcitic fossils in these two samples are not as many as BM-9403. In other words, carbon cementation may exist in PB-8668 and WL-8649. SEM images prove this interpretation, that the carbonate cement seals the intraparticle pores in clay bundles (Fig. 5i-j). Samples PB-8889 and WL-8839 have enough clay contents, however, these two samples have less clay orientation and clay bundles in SEM images (Fig. 5p).

In summary, four types of pores can be classified in the Wolfcamp Shale samples: silt-mesopores, silt-macropores, wedge-mesopores, and wedge-macropores. Regardless of the grain sizes, the dominance of “quartz + feldspar” and orientated clays could help in forming the “sandwich” structure to generate slit-shaped mesopores. Increasing the mesopore percentage could enhance total pore volume and pore surface area. The presence of carbonates may not decrease the porosity unless it acts as cementation.

5.3. Fluid-rock interaction

The layered structure and “sandwich” structure inherited from depositional laminations could form fluid pathway (Backeberg et al., 2017), as a reason why P

direction testing imbibes more liquid than in T direction. In P direction, samples with nearly half “quartz + feldspar” and half clays tend to imbibe faster in DIW tests, and samples with less clays tend to imbibe 2DT faster. The fitted imbibition slope reflects the rate of imbibition; the higher the value, the faster the imbibition. By comparing the imbibition in two directions, P direction imbibes more liquid but a little bit slower than in T direction. This faster imbibition in T direction may be due to the capillary pressure (Hu et al., 2001). The sandwich structure and layered structure that parallel to the P direction may act as barrier to prevent the fluid from moving upward in T direction.

By coupling the spontaneous imbibition behavior with the results of TOC, porosity, and lithology, samples with high TOC and high porosity tend to imbibe more 2DT in P direction, such as BM-9403, PB-8907, and WL-8839 (Fig. 19). However, porosity in BM-9403 is not as high as in other samples. Maybe as the only sample that is more oil-wet is the reason why sample BM-9403 imbibes more 2DT than DIW. Most Wolfcamp Shale samples are mixed-wet in terms of wettability. Compared to the porosity, the effect of wettability in imbibed liquid volume seems not as much as porosity. However, not all the samples imbibe more liquid in P direction. The imbibed liquid volumes in two directions of SR103-9857 and UR-7630 are very similar. Especially, the imbibed DIW volumes are very close in two samples, though these two samples have different lithologic compositions. From the plots of carbonate content and clay content respectively against imbibed volume of DIW, the imbibed volume decreases with an increasing carbonate contents (Fig. 20). The imbibed volume first increase with clay contents then decreases when clay contents are over 30% (Fig. 20). SR103-9857 contains carbonates at over 70% and UR-7630 contains clays over 40%. Therefore, the excess carbonate and clays may make the imbibition volume similar in these two samples. Samples dominated by quartz tend to show no preference of

imbibing liquid with relatively equal amounts of imbibed volumes for DIW and 2DT, such as BM-9675, PB-8889, and SL-9268. With clay contents lower than 30%, clay swelling may open the pathway for liquid flow. However, the swelling effect with clay contents over 30% may block the pathway and decrease the imbibed liquid volume (Dong et al., 2019; Sharifipour et al., 2017). Another note is that both illite and illite-smectite mixed layer, detected for deep shales, have much lower water swelling capabilities than montmorillonite.

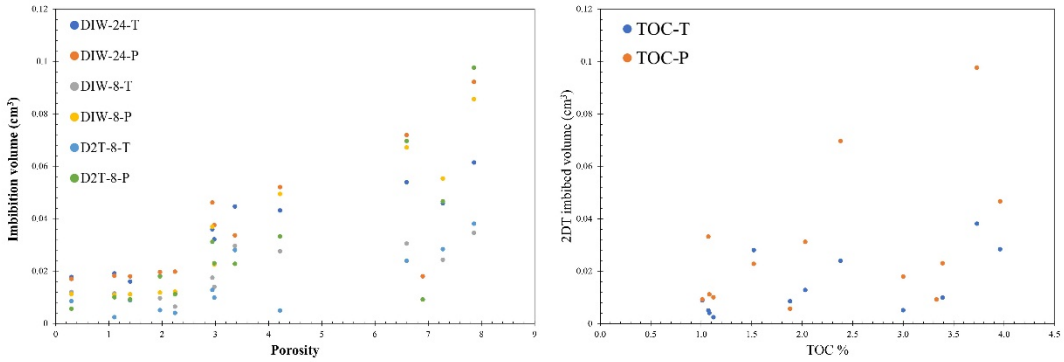

Figure 17. Imbibed volume vs. MIP porosity and TOC contents.

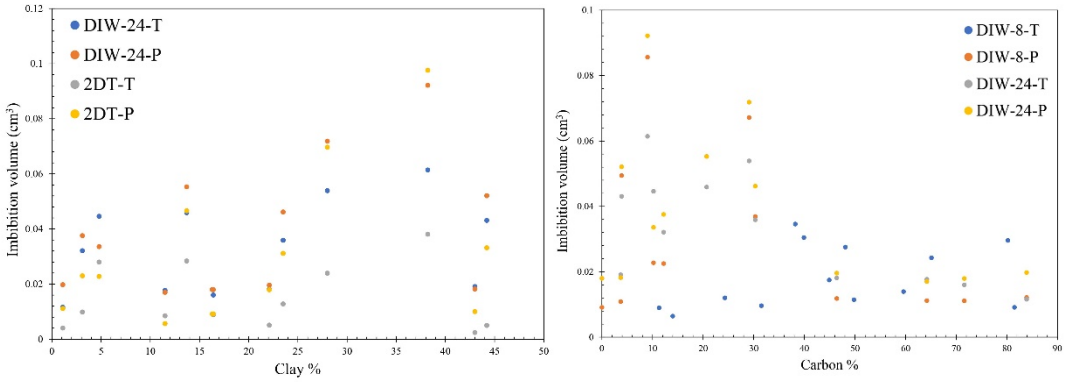

Figure 18. Plots of imbibition volume of DIW vs. clays and carbonate contents.

6. Conclusions

A total of 13 Wolfcamp Shale core samples from six wells were studied and the results showed a high heterogeneity in mineralogy, lithology, maturity, pore structure, and fluid-rock interaction. Wolfcamp Shale is dominated by siliciclastic and carbonate with various clay contents. The porosity is highly heterogenous with average of 3.84%.

The two lithofacies of mudrock and calcareous mudrock indicate the hemiplegic depositional environment of the Wolfcamp Shale. The primary wettability is intermediately mixed-wet with several slightly oil-wet preferred samples. The Wolfcamp Shale is in oil window with mixed Type II and Type III kerogen with a good indication of hydrocarbon generation.

Pore structure including porosity, pore shape, and pore size distribution has a close relationship with mineralogy in the Wolfcamp Shale. Porosity has a positive relationship with quartz contents and negative relationship with carbonate contents. As clay contents increase, the porosity increases first and then decrease. Four type of pores were identified based on MIP, GP, SEM, and SAXS results: slit-shaped mesopores, slit-shaped macropores, wedge-shaped mesopores, and wedge-shaped macropores. Both compaction and carbonate cementation could limit the porosity and diminish mesopores, while the fractures could increase the porosity and act as pathways for fluid migration. The layered/bedding structures create pathways for hydrophilic water to move along the layers in fluid-rock interactions. The spacial relationship of grains (sandwich structure) inherited from the deposition may be the primary reason of the layered structure and pore shapes.

Acknowledgment

We thank the financial support from the Nuclear Energy University Program managed by the Office of Nuclear Energy at U.S. Department of Energy (award number DE-NE0008797), and Lowell Waite of Pioneer Resources for his efforts of procuring the samples used in this work. The X-ray scattering data were collected at the X-ray Science Division beamline of 9-ID, a resource of the Advanced Photon Source, a U.S. Department of Energy (DOE) Office of Science User Facility operated for the DOE Office of Science by Argonne National Laboratory under Contract No. DE-AC02-

06CH11357.

References

Awwiller, D. N. (1993). Illite/smectite formation and potassium mass transfer during burial diagenesis of mudrocks; a study from the Texas Gulf Coast Paleocene-Eocene. Journal of Sedimentary Research, 63(3), 501-512.

Backeberg, N. R., Iacoviello, F., Rittner, M., Mitchell, T. M., Jones, A. P., Day, R., ... & Striolo, A. (2017). Quantifying the anisotropy and tortuosity of permeable pathways in clay-rich mudstones using models based on X-ray tomography. Scientific Reports, 7(1), 1-12.

Bangia, V. K., Yau, F. F., & Hendricks, G. R. (1993). Reservoir performance of a gravity-stable, vertical CO_2 miscible flood: Wolfcamp Reef Reservoir, Wellman Unit. SPE Reservoir Engineering, 8(04), 261-269.

Baumgardner, R. W., Hamlin, H. S., & Rowe, H. D. (2014). High-resolution core studies of Wolfcamp/Leonard basinal facies, southern Midland basin, Texas. AAPG Search and Discovery, 10607, 1-4.

Bhandari, A. R., Flemings, P. B., Ramiro-Ramirez, S., Hofmann, R., & Polito, P. J. (2019). Gas and liquid permeability measurements in Wolfcamp samples. Fuel, 236, 1026-1036.

Casey, B., Wehner, M., Richards, B., & Moore, C. (2018, September). Wolfcamp Geologic Reservoir Modeling Challenges. In Unconventional Resources Technology Conference, Houston, Texas, 23-25 July 2018 (pp. 270-280). Society of Exploration Geophysicists, American Association of Petroleum Geologists, Society of Petroleum Engineers.

Chen, Q., Kang, Y., You, L., Yang, P., Zhang, X., & Cheng, Q. (2017). Change in composition and pore structure of Longmaxi black shale during oxidative dissolution. International Journal of Coal Geology, 172, 95-111.

Colborne, J. (2020). A Multi-Scale Approach to Reservoir Characterization of the Wolfcamp A, Delaware Basin, Texas. Colorado School of Mines.

Crawford, B. R., Faulkner, D. R., & Rutter, E. H. (2008). Strength, porosity, and permeability development during hydrostatic and shear loading of synthetic quartz‐clay fault gouge. Journal of Geophysical Research: Solid Earth, 113(B3).

Desbois, G., Urai, J.L., Kukla, P.A., 2009. Morphology of the pore space in claystones: evidence from BIB/FIB ion beam sectioning and cryo-SEM observations. eEarth Discussions 4, no. 1 (2009): 1-19.

Dong, B., Meng, M., Qiu, Z., Lu, Z., Zhang, Y., & Zhong, H. (2019). Formation damage prevention using microemulsion in tight sandstone gas reservoir. Journal of Petroleum Science and Engineering, 173, 101-111.

Eckert, T., Schmidt, M., & de las Heras, D. (2022). Sedimentation of colloidal plate-sphere mixtures and inference of particle characteristics from stacking sequences. Physical Review Research, 4(1), 013189.

Fairhurst, B., Ewing, T., & Lindsay, B. (2021). West Texas (Permian) Super Basin, United States: Tectonics, structural development, sedimentation, petroleum systems, and hydrocarbon reserves. AAPG Bulletin, 105(6), 1099-1147.

Hamlin, H. S., and Baumgardner, R. W., Jr., 2012, Wolfberry (Wolfcampian-Leonardian) Deep-Water Depositional Systems in the Midland Basin: Stratigraphy, Lithofacies, Reservoirs, and Source Rocks: The University of Texas at Austin, Bureau of Economic Geology, Report of Investigations No. 277, 61 pp.

Jackson, K. S., Hawkins, P. J., & Bennett, A. J. R. (1980). Regional facies and geochemical evaluation of the southern Denison Trough, Queensland. The APPEA Journal, 20(1), 143-158.

Hu, M. Q., Persoff, P., & Wang, J. S. (2001). Laboratory measurement of water imbibition into low-permeability welded tuff. Journal of Hydrology, 242(1-2), 64-78.

Labani, M. M., Rezaee, R., Saeedi, A., & Al Hinai, A. (2013). Evaluation of pore size spectrum of gas shale reservoirs using low pressure nitrogen adsorption, gas expansion and mercury porosimetry: A case study from the Perth and Canning Basins, Western Australia. Journal of Petroleum Science and Engineering, 112, 7-16.

Liu, K., Ostadhassan, M., Zhou, J., Gentzis, T., & Rezaee, R. (2017). Nanoscale pore structure characterization of the Bakken shale in the USA. Fuel, 209, 567-578.

Li, L., & Sheng, J. J. (2017). Nanopore confinement effects on phase behavior and capillary pressure in a Wolfcamp shale reservoir. Journal of the Taiwan Institute of Chemical Engineers, 78, 317-328.

Ojha, S. P., Misra, S., Sinha, A., Dang, S., Tinni, A., Sondergeld, C., & Rai, C. (2018). Relative permeability and production-performance estimations for Bakken, Wolfcamp, Eagle Ford, and Woodford shale formations. SPE Reservoir Evaluation & Engineering, 21(02), 307-324.

Peng, S., Liu, Y., Ko, L. T., & Ambrose, W. (2019). Water/Oil Displacement by Spontaneous Imbibition Through Multiscale Imaging and Implication on Wettability in Wolfcamp Shale. In SPE/AAPG/SEG Unconventional Resources Technology Conference. OnePetro.

Perry, S. E., Walls, J., & Rider, T. (2017, April). Comparing and contrasting analytically quantified porosity and pore size distributions in the Wolfcamp Formation from SEM imaging, nuclear magnetic resonance (NMR), and crushed rock core analysis. In Nuclear Magnetic Resonance (NMR), and Crushed Rock Core Analysis, AAPG Annual Conference and Exhibition, Houston, TX.

Peters, K. E. (1986). Guidelines for evaluating petroleum source rock using programmed pyrolysis. AAPG Bulletin, 70(3), 318-329.

Peltonen, C., Marcussen, Ø., Bjørlykke, K., & Jahren, J. (2009). Clay mineral diagenesis and quartz cementation in mudstones: The effects of smectite to illite reaction on rock properties. Marine and Petroleum Geology, 26(6), 887-898.

Ramiro-Ramirez, S., Bhandari, A. R., Flemings, P. B., & Reed, R. M. (2020, July). Porosity and permeability heterogeneity in the Upper Wolfcamp, Delaware Basin, West Texas: implications for production. In SPE/AAPG/SEG Unconventional Resources Technology Conference. OnePetro.

Seelen, L. J. H., Padding, J. T., & Kuipers, J. A. M. (2018). A granular discrete element method for arbitrary convex particle shapes: method and packing generation. Chemical Engineering Science, 189, 84-101.

Sharifipour, M., Pourafshary, P., & Nakhaee, A. (2017). Study of the effect of clay swelling on the oil recovery factor in porous media using a glass micromodel. Applied Clay Science, 141, 125-131.

Taheri, P., Lang, J. C., Kenvin, J., & Kroll, P. (2021). Differential hysteresis scanning of non-templated monomodal amorphous aerogels. Physical Chemistry Chemical Physics, 23(9), 5422-5430.

Tang, X., Jiang, Z., Li, Z., Gao, Z., Bai, Y., Zhao, S., & Feng, J. (2015). The effect of the variation in material composition on the heterogeneous pore structure of

high-maturity shale of the Silurian Longmaxi formation in the southeastern Sichuan Basin, China. Journal of Natural Gas Science and Engineering, 23, 464-473.

Thyberg, B., Jahren, J., Winje, T., Bjørlykke, K., Faleide, J. I., & Marcussen, Ø. (2010). Quartz cementation in Late Cretaceous mudstones, northern North Sea: Changes in rock properties due to dissolution of smectite and precipitation of micro-quartz crystals. Marine and Petroleum Geology, 27(8), 1752-1764.

Thommes, M., Kaneko, K., Neimark, A. V., Olivier, J. P., Rodriguez-Reinoso, F., Rouquerol, J., & Sing, K. S. (2015). Physisorption of gases, with special reference to the evaluation of surface area and pore size distribution (IUPAC Technical Report). Pure and Applied Chemistry, 87(9-10), 1051-1069.

United States. U.S. Energy Information Administration report. (2018). Permian Basin Wolfcamp Shale Play Geology review. https://www.eia.gov/maps/pdf/PermianBasin_Wolfcamp_EIAReport_Oct2018.pdf.

United States. U.S. Energy Information Administration EIA (2020a), Permian Basin Part 2 Wolfcamp Shale Play of the Midland Basin Geology review. https://www.eia.gov/maps/pdf/Permian_Wolfcamp_Midland_EIA_reportII.pdf.

United States. U.S. Energy Information Administration EIA (2020b), https://www.eia.gov/todayinenergy/detail.php?id=49076.

Wang, Q., Zhou, W., Hu, Q., Xu, H., Meendsen, F., Shu, Y., & Qiao, H. (2020). Pore Geometry Characteristics and Fluid–Rock Interaction in the Haynesville Shale, East Texas, United States. Energy & Fuels, 35(1), 237-250.

Waples, D. W. (2013). Geochemistry in petroleum exploration. Springer Science & Business Media, 107-108.

Wilson, R. D., Chitale, J., Huffman, K., Montgomery, P., & Prochnow, S. J. (2020). Evaluating the depositional environment, lithofacies variation, and diagenetic processes of the Wolfcamp B and lower Spraberry intervals in the Midland Basin: Implications for reservoir quality and distribution. AAPG Bulletin, 104(6), 1287-1321.

Wickard, A. K., Elmore, R. D., & Heij, G. (2016, August). A diagenetic study of the wolfcamp shale, midland basin, west texas. In SPE/AAPG/SEG Unconventional Resources Technology Conference. OnePetro.

Yang, C., Zhang, J., Tang, X., Ding, J., Zhao, Q., Dang, W., Chen, H., Su, Y., Li, B., Lu, D. (2017). Comparative study on micro-pore structure of marine, terrestrial, and transitional shales in key areas, China. International Journal of Coal Geology, 171, 76-92.

Yuan, Y., Rezaee, R., Al-Khdheeawi, E. A., Hu, S. Y., Verrall, M., Zou, J., & Liu, K. (2019). Impact of composition on pore structure properties in shale: implications for micro-/mesopore volume and surface area prediction. Energy & Fuels, 33(10), 9619-9628.

Zhang, T., Fu, Q., Sun, X., Hackley, P. C., Ko, L. T., & Shao, D. (2021). Meter-scale lithofacies cycle and controls on variations in oil saturation, Wolfcamp A, Delaware and Midland Basins. AAPG Bulletin, 105(9), 1821-1846.

Zhao, J., Jin, Z., Jin, Z., Wen, X., & Geng, Y. (2017). Origin of authigenic quartz in organic-rich shales of the Wufeng and Longmaxi Formations in the Sichuan Basin, South China: Implications for pore evolution. Journal of Natural Gas Science and Engineering, 38, 21-38.

Chapter IV

Porosity measurement of granular rock samples by improved bulk density analyses

C. Zhao[1], W. Zhou[2], Q.H. Hu[1*], H. Xu[2], and C. Zhang[3]

[1] Department of Earth and Environmental Science, the University of Texas at Arlington, TX 76019, USA

[2] State Key Laboratory of Oil and Gas Reservoir Geology and Exploitation, Chengdu University of Technology, Chengdu, 610059, China.

[3] Key Laboratory of Unconventional Oil and Gas Geology, China Geological Survey, Beijing, 100083, China.

Published at:

Marine and Petroleum Geology

*Corresponding author: maxhu@uta.edu

Abstract

Interest in assessing the extent of isolated pores in the total (both effective and isolated) porosity of tight rocks has increased in recent years due to the development of unconventional shale reservoirs. Porosity measurements of crushed granular and whole rock samples can be used to assess the proportion of isolated pores in the total porosity, which will help with reservoir characterization and understanding petroleum production. This study aims to measure the porosities of granular samples by independent measurements of bulk density (i.e., the density of the matrix and pore space combined) and particle density (i.e., the density of the matrix alone) provided by a modified bulk density method and helium pycnometry. The modified/improved bulk density method uses quartz powder (<75 μm) to substitute for the original larger- and uniform-sized DryFlo of the GeoPyc 1365 method to measure the density of granular rock samples in the size range 75-850 μm, thereby extending the sample size range for bulk density analysis of granular samples to 75-8000 μm. Using four rock samples as examples, the bulk density and particle density of crushed Woodford Shale (two samples with different pore connectivity), Paluxy Sandstone, and Austin Chalk were measured for the porosity calculation and assessment of isolated pores. The results show that (1) the improved bulk density measurement of granular crushed-rock could provide semi-quantitative results with good repeatability and reproducibility, and (2) the changes in effective porosity as a function of sample size are related to the primary grain size for well-connected sandstone and chalk, and the extent of isolated pores for shales with poor pore connectivity.

1. Introduction

The petrophysical properties of fine-grained rocks are not always constant for different sample sizes due to their poor pore connectivity as a result of the significant presence of “isolated” pores, which are not absolutely isolated but rather not easily measurable due to their small size (typically at sub-10 nm), testing duration, and resulting experimental/instrumental limitations (Hu, 2018). Analyses on coal by Chen et al. (2018), as well as shale by Davudov and Moghanloo (2016), show a negative relationship between porosity and sample size due to the opening of isolated pores in smaller-sized samples after crushing. For example, Busch et al. (2017) and Fu et al. (2019) reported that over 40% of the pores in shales are isolated, and a decrease in granular size can cause the isolated pores to become accessible to the sample surface.

The common laboratory methods for porosity measurement use fluids (e.g., helium, water, mercury, and nitrogen) that invade and/or submerge samples, to obtain both pore and bulk volumes from which porosity is calculated (Flint and Flint, 2002; Hu, 2018). The methods of water immersion porosimetry (WIP) assisted by vacuum saturation, and mercury intrusion porosimetry (MIP) with the help of high pressure, have been developed based on these principles (e.g., Flint and Flint, 2002; Kuila et al., 2014; Hu, 2018). However, WIP is only applicable to whole rock samples of >2 mm in linear dimension, and not to crushed granular samples of smaller sizes. For MIP, which can cover a wide range of sample sizes from a few μm to 2.54 cm (cylindrical core plug), the granular crushed-rock samples will introduce a porosity (and pore-throat size distribution) peak due to the inter-granular space, which may be indistinguishable from the intra-granular porosity (Hearn and Hooton, 1992; Webb, 2001; Hu, 2018). These fluid-occupying approaches can only investigate pores connected to the sample surface (thus, effective porosity), and do not include isolated pores. The newly developed

SANS (small angle neutron scattering) and SAXS (small angle X-ray scattering) technique can measure total porosity, including both edge-accessible and isolated pores, in granular samples (e.g., Radlinski et al, 2004; Zhang et al., 2020). However, SANS instrumentation is costly and only available at a few national facilities.

The commonly-used density method for porosity calculation utilizes independent measurements of both particle density$\rho_{particle}$ (i.e., the density of a rock or mineral matrix excluding the pore space, in units of g/cm^3) and bulk densityρ_{bulk} (the mass of a bulk solid that occupies a unit volume of a bed/rock, including the volume of all interparticle voids, g/cm^3). The porosity is then 1- $\frac{\rho_{bulk}}{\rho_{particle}}$. The particle density can be obtained by the standard approach of helium pycnometry, for μm-cm sized samples. While the terms particle density and grain density can be used interchangeably in the literature, we follow the convention of Flint and Flint (2002) by defining the particle density for a rock with multiple minerals (e.g., quartz and feldspar), while the grain density applies to individual minerals (e.g., quartz or feldspar). While it is trivial to obtain the bulk density for samples larger than ~2 mm (either geometrically calculated for regularly-sized samples or submerged in a fluid using Archimedes' Principles for irregular samples), it is challenging to obtain the bulk density values of smaller-sized granular samples, which can still possess significant pore spaces in fine-grained shale (Hu, 2018). Many authors have measured the porosity of crushed-rock samples in granular form with the density method, assuming (probably incorrectly) a constant bulk density for different granular samples by using the value obtained from a whole rock sample (Klaja et al., 2015; Sun et al., 2016; Fu et al., 2019; Gaus et al, 2020). However, several studies have reported that the bulk density of different-sized (from 1-2 mesh to >300 mesh) granular samples is not constant (Davudov et. al., 2016; Chen et al., 2018; Hu, 2018). It has been well documented that there is more variation in the

bulk density than particle density among a range of sample sizes, and this is related to the presence of isolated pores, especially for tight rocks (Hu et al., 2015; Yang et al., 2017; Hu, 2018). Therefore, the porosity calculated by assuming a “constant” bulk density among different-sized rock samples could be inaccurate, which leads to an uncertainty in reservoir characterization.

Direct laboratory methods for bulk density measurement of crushed granular rocks are rare in previous research, while there are some reports from pharmaceutical and engineering studies using the GeoPyc 1365 bulk density analyzer (Patel et al., 2005; Acevedo et al., 2012; Bi et al., 2014). GeoPyc 1365 (GP) uses tiny solid spheres (commercially named DryFlo) as the enveloping material to surround the sample grains to obtain volumes, and then uses mass over volume to obtain bulk density. GP with DryFlo could test bulk densities for granular samples with sizes 850-8000 μm)

In this study, we propose an improved bulk density method using finer-sized and poorly-sorted powder (<75 μm) of crushed solid quartz (no porosity) as a new enveloping material to extend the GP’s low limit of measurable grain sizes to 75 μm. Using four rock samples with three different lithologies, analyzed by X-ray diffraction (XRD), this work presents a detailed study of the improved bulk density analysis for small-sized granular samples (75-8000 μm) and demonstrates that the variable patterns of porosity as a function of sample sizes are related to geological factors and pore structure.

2. Samples and Methods

2.1. Samples

Four outcrop rock samples were used in this work. Two Woodford (WFD)

samples were collected from Ardmore, southern Oklahoma, and Paluxy Sandstone and Austin Chalk were obtained from southern Dallas, Texas (Table 1). These samples were cored, saw-cut, and crushed & sieved into six granular sizes: 2360-8000 μm, 1700-2360 μm, 841-1700 μm, 500-841 μm, 177-500 μm, and 75-177 μm. Granules smaller than 75 μm were saved but not involved in the experiments. For all the sample sizes, from 2.54 cm dia. cylindrical plugs down to >75 μm granular samples, the accompanying particle density measurement was achieved using helium pycnometry, described in the next section. Prior to the measurements of both particle and bulk densities, all the samples were dried in an oven at 60°C for 48 hours to remove the moisture. In addition, WIP and MIP analyses were applied to 1-cm^3 cubic samples to compare the porosity results with those from GP (Hu et al., 2012; 2017).

Table 1. Sample information

Sample ID	Sample Location	Mineralogy (%)					MIP Porosity (%)	WIP Porosity (%)	
		Quartz	Carbonate	Feldspar	Gypsum	Clay	1-cm^3 Cube	1-cm^3 cube	1-in dia. core plug
WFD-4-6L	Ardmore, OK	14	86	0	0	0	3.12	3.94	1.85
WFD-9	Ardmore, OK	68	0	0	13	19	12.48	13.85	7.17
Paluxy Sandstone	Glen Rose, TX	95	0	5	0	0	11.12	NA	NA
Austin Chalk	Ellis County, TX	1	96	0	0	3	29.05	NA	NA

2.2. Methods

2.2.1. AccuPyc 1340 pycnometer

A helium gas displacement pycnometer [AccuPyc 1340 (AP) by Micromeritics] was used to determine the particle density for all sample sizes of the four rocks. The AP apparatus is composed of two cells with known volume, a reference (empty) cell and a sample cell, that are connected by a valve. Helium gas fills (expands) in the

reference chamber at 19.5 psi (Micromeritics, 2014). With the valve open, the pressure in the reference cell will decrease and equilibrate at a lower pressure with that of sample cell. Boyle's law in a closed system with a constant temperature states that:

$$PV = nRT \qquad (1)$$

where P is pressure, V is volume, n is the moles of helium gas, R is the universal gas constant, and T is the temperature (Danielson and Sutherland, 1986; API RP40, 1998; Flint and Flint, 2002). The gas volume is inversely proportional to the pressure at a fixed temperature. The particle density can be calculated using the mass over volume that is calculated with the pressure drop using Boyle's law. The AP technique is able to generate the particle densities with a reproducibility of ±0.01% (Micromeritics, 2014; Trippetta et al., 2020).

2.2.2. MIP and WIP

Both MIP and WIP were conducted on 1 cm^3 cubes for porosity measurement. Under pressure, the non-wetting mercury intrudes into the sample edge-accessible pores with increasing pressure, and the decrease in volume of mercury at every pressure step equates to the pore volume for a given pore-throat size corresponding to each pressure, while the cumulative volume of mercury intruded up to the highest intrusion pressure of 414 MPa is used for the total porosity calculation (Danelson and Sutherland, 1986; Hu et al., 2017). An AutoPore IV 9520 porosimeter by Micromeritics was used for the MIP analyses. WIP uses a similar principle to MIP but with vacuum saturation. Using our custom-designed apparatus, the vacuum saturation results in the invasion of the maximum volume of de-aired water into the evacuated (edge-accessible) pore space. The water-saturated sample was then submerged under de-aired water to obtain the bulk volume by the Archimedes' principle (Hu et al., 2012; 2015). Kuila et al. (2014)

presented a detailed study of WIP technique for porosity analyses of gas shales.

2.2.3. XRD

The minerology of each rock sample was measured by a Shimadzu XRD-7000 X-ray Diffractometer. a powdered sample (< 75 μm) was mounted in an aluminum holder and analyzed by CuKα radiation with angles from 2° to 70° at a speed of 2°/min. Weight percentages of minerals were estimated by JADE 9 Whole Pattern Fitting Software.

2.2.4. Grain size analyses

Several methods were used in this work to obtain grain sizes and grain size distribution of the rock samples and enveloping materials. Shimadzu SALD-7101 Laser Diffraction Nano Particle Analyzer was applied for the measurement of particle size distribution of quartz powder. The scattering angle of the diffracted laser light when passing through the particle is related to the particle size, and the particle size distribution related to the light intensity of the diffracted light (Jones, 2003; Stojanović et.al., 2012). With 375 nm UV wavelength, the range of measurable particle size range is from 10 nm to 300 μm, and the measurements were performed three times.

To assess the impact of grain size on porosity results for crushed-rock samples of different sizes, the primary sand grain sizes of the Paluxy Sandstone were measured using a Hitachi N-3000 scanning electronic microscope on a thin section whole sample (no coating) and a Leica M125C stereo microscope on crushed-granular samples. The images by back scattered electrons (BSE) that created by the interaction of the electron beam and near-surface region could reveal the compositional contrast of the sample (Vernon-Parry, 2000). In this paper, multiply scattered BSE (BSE2) signal was applied.

A total of 14 images were scanned on the thin section under 25 kV at BSE mode with 100× magnification, from which the sand sizes were counted by ImageJ (Schneider et al., 2012). A total of 4 images were obtained for DryFlo under 15 kV at SE mode with various magnifications, and the grain sizes were counted as well. The stereo microscope Leica M125C was applied for grain size observation on the Paluxy Sandstone.

2.2.5. Granular bulk density measurement by GP

As described earlier, the sample mass over bulk volume was applied to obtain the bulk density. The mass is measured by an electronic balance, and the bulk volume is measured by GP on rocks in glass cylinders with different inner diameters to accommodate different-sized samples (Fig. 1). Every cylinder has its own constant conversion factor for bulk volume measurement, which is obtained from the blank measurement. The bulk volume measurement procedure includes two steps: blank and sample measurements. For the blank measurement, only DryFlo is added into the cylinder. DryFlo is a proprietary product of incompressible spheres with a fairly uniform size of 127±40 μm (average ± standard deviation for 105-point count) with graphitic lubrication. During the process, the cylinder spins while the piston moves forward to compress the DryFlo with a pre-set consolidation force (38 or 45 N); this process (called the preparation cycle) is repeated five or ten times to increase the precision of the bulk volume measurement by obtaining the conversion factor of piston distance to volume. For the subsequent sample measurement, the weighed sample is added to the same cylinder and mixed with the existing DryFlo, and the system repeats the compression process with the same force, also for the same number of preparation cycles. Both blank and sample measurements require preparation cycles (for compression) and measurement cycles. The piston insert depth is only recorded in

measurement cycles. GP converts the recorded insert depth into the volume by multiplying the conversion factor of the cylinder. The bulk volume is then calculated from the volume difference between blank and sample measurements. Most tests use five preparation cycles and 38 N (as suggested by Micromeritics, 2017), and we also tested ten cycles and 45 N for steel balls and granular crushed-quartz to evaluate the possible impact on reproducibility and precision of the bulk density results.

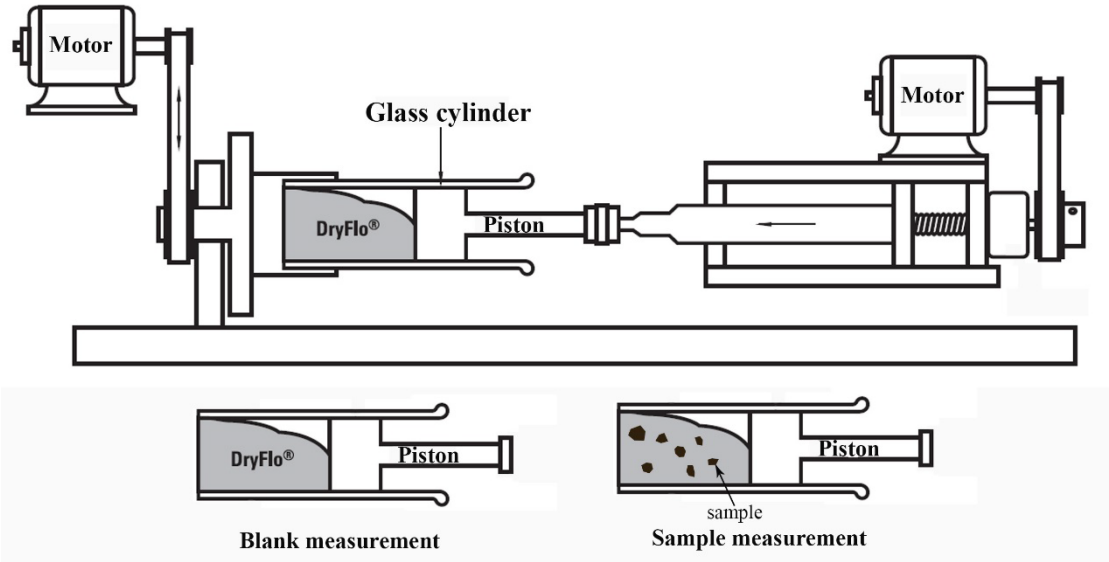

Figure 19. Schematic diagram of the GeoPyc 1365 bulk density analyzer

DryFlo is designed to enclose the whole rock and large-sized granular samples and move smoothly in the cylinder. The designed measurable sample size range for DryFlo is from 38 mm (whole rock) to 0.85 mm (granular) (Micromeritics, 2017). The void space generated by granular stacking is termed the packing pore volume (PPV) in this work. The PPV generated by DryFlo and samples (>850 μm) can be directly taken into account from the blank and sample measurements, because of the similarity of the PPV generated by DryFlo versus DryFlo & sample. Therefore, the volume difference of blank and sample measurements is the sample bulk volume. However, the smaller the size difference between DryFlo and samples, the less accurate the results will be. With smaller size differences of granules (DryFlo and samples) in the cylinder, the sorting of granules becomes better. Well-sorted granules have more porosity than

poorly-sorted ones after artificial compaction (Rogers and Head, 1961; Beard and Weyl, 1973). The PPVs are not similar anymore before and after adding the sample to the cylinder. Therefore, the PPV cannot be taken into account from the blank and sample measurements. Furthermore, Hu et al. (2015; 2018) reported a dual connectivity zone behavior for shales, with the well-connectivity surface zone located at ~400 μm from the sample surface under atmospheric pressure and temperature conditions; therefore, there is a need for a method to measure the bulk density, and hence effective porosity, of granular samples less than 400 μm. A new enveloping material with a size smaller than DryFlo needs to be introduced to extend the measurement limitation of bulk volume (density) towards smaller granular sizes. This is discussed in the next section.

2.2.6. Bulk density measurement by GP using a quartz-powder method

Quartz crystal from Ward's Science Co. is a non-porous material that should have very similar particle and bulk densities for any granular sizes. This was verified by the measurement of the bulk and particle densities by the AP and GP methods, thus showing it to be an ideal enveloping material. We introduced crushed quartz powder (<75 μm) to substitute DryFlo for bulk density measurements of small-sized granular samples (<850 μm). As the crushed quartz is more poorly sorted than the DryFlo particles, the PPVs are different from the simultaneous blank and sample measurements. Because well-sorted granular samples contain more PPV than poorly-sorted ones. Thus, the total packing pore volume (TPPV) generated by quartz powder and samples needs to be calculated, as described by Eqs. 2-3. The TPPV is the total intergranular pore volume resulting from the stacking of quartz powder and the tested granular samples. From whole solid quartz, we generated crushed granular samples and sieved them in the same way as four rock samples to obtain six granular size fractions, to be termed as

"quartz standards", for the calculation of TPPV.

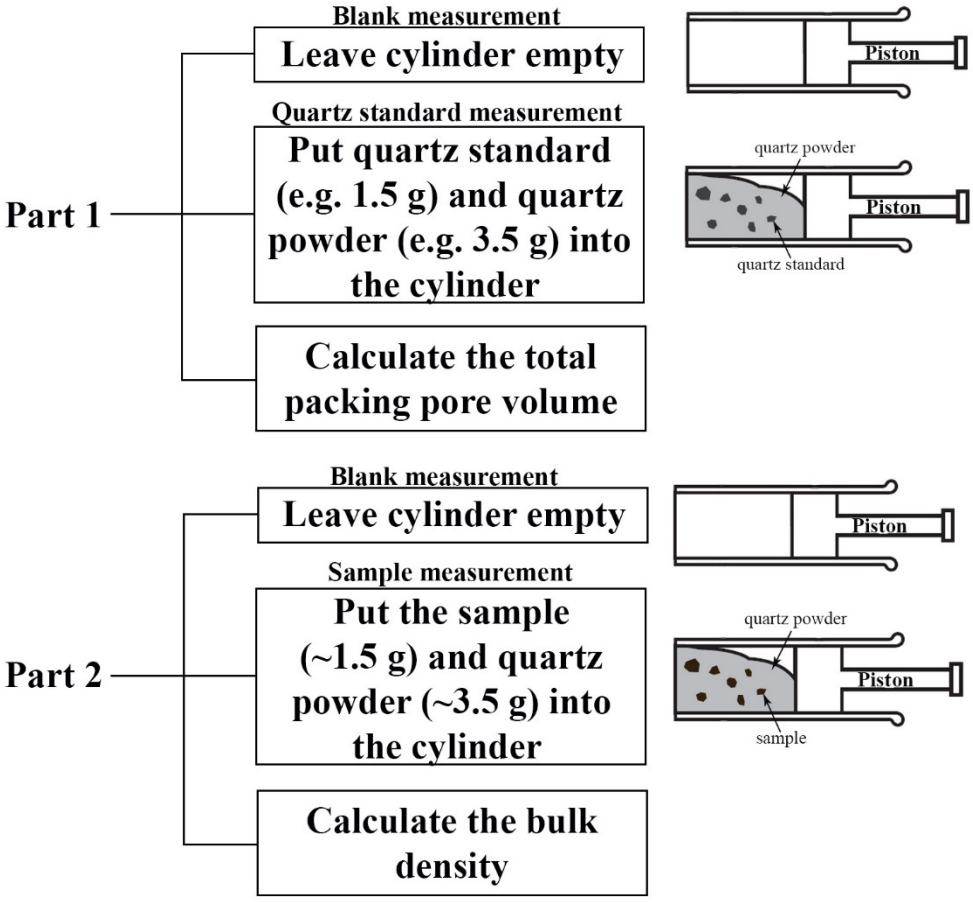

Figure 20. Workflow for the quartz-powder method for bulk density measurement.

The procedure of the quartz-powder/quartz standard method is similar to that of the DryFlo method and consists of blank and sample measurements (Fig. 2). In the blank measurement, the piston compresses with no granules in the cylinder. In the quartz standard sample measurement, the weighed quartz powder (~3.5 g) and quartz standard (~1.5 g) were added and mixed together inside the cylinder. The obtained volume (V_{GP}) from GP data report is the total volume of quartz powder ($V_{qtz\ powder}$), quartz standard ($V_{qtz\ standard}$), and TPPV. The volume of quartz powder and quartz standard can be calculated from their weights and the density, while Equation 2 calculates the TPPV.

$$TPPV = V_{GP} - V_{qtz\ powder} - V_{qtz\ standard} \quad (2)$$

After obtaining the TPPV for each size fraction of the quartz standards, the bulk density of rock samples can be measured with the same operation procedure. By replacing the quartz standard with an almost identical mass (standard deviation at ±0.002) and same size range of the rock sample and keeping the quartz powder mass constant, we can measure the bulk volume of the sample by Equation 3. By following these practices, we reasonably assume that TPPV is constant for almost identical weights of quartz powder and quartz standard or sample.

$$\text{Sample volume} = V_{GP} - V_{qtz\ powder} - TPPV \qquad (3)$$

3. Results and Discussion

Lithologies assessed by XRD and porosities measured by MIP and WIP of the four samples are shown in Table 1. Table 2 shows the bulk density (by the DryFlo method) and particle density (by the AP method) of the quartz standards. We take 2.650 g/cm^3, the average bulk density of the sizes at 2360-8000 μm and 1700-2360 μm, as the quartz standard bulk density (Table 2). The results from other smaller sizes start to show the limitation of DryFlo method with the measured apparent bulk density deviating from 2.650 (expected for solid quartz with nearly zero porosity) when the sample sizes become similar to DryFlo size of 130±40 μm; more importantly, it's the uniform size of DryFlo and samples generates more PPV than expected. The <75 μm quartz powder is measured to exhibit a poor-sorted grain size distribution by containing <0.1 μm grain

sizes at 35.7%, <1 μm at 63.6%, and <10 μm at 71.9% (Fig. 3).

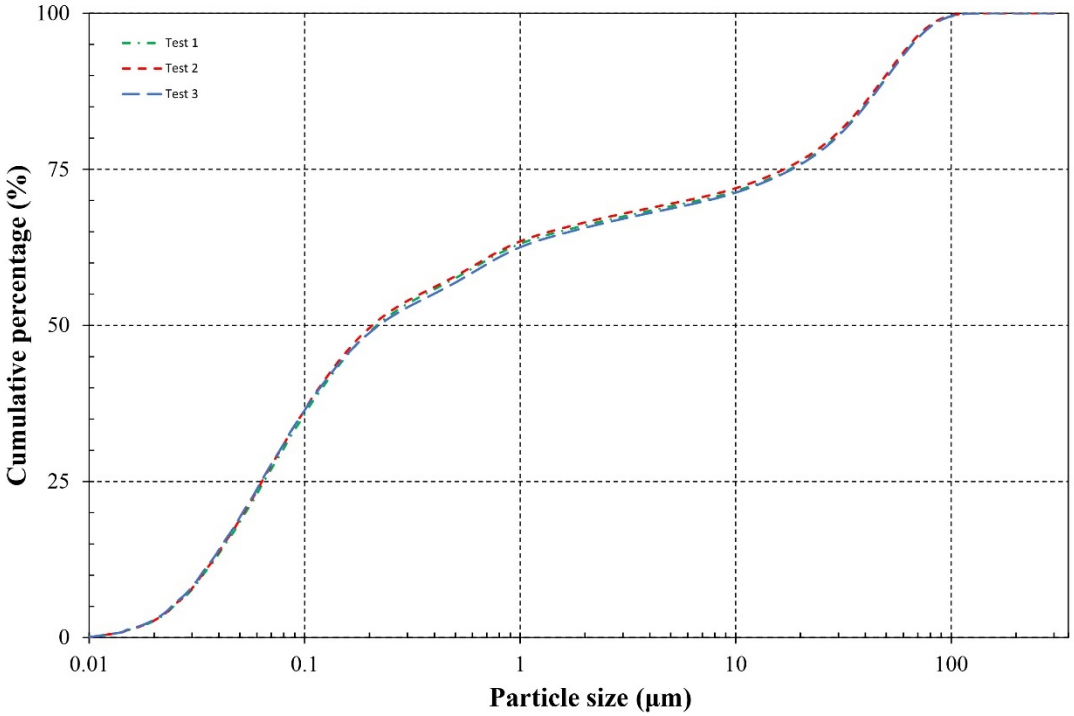

Figure 21. Particle size distribution measured for quartz powder by three tests.

To the contrary, the particle density values of all seven sizes for quartz are very consistent, with an average of 2.649 g/cm^3, as the literature value (Table 2). Particle density results of the four rock samples are presented in Table 3, and a slight variation is related to their mineral compositions.

Table 2. DryFlo-derived bulk density and particle density of quartz standards

Granular size (μm)	Bulk density g/cm^3	Particle density g/cm^3
2360-8000	2.637	2.643
1700-2360	2.663	2.644
841-1700	*2.476*	2.644
500-841	*2.102*	2.650
177-500	*1.751*	2.652
75-177	*1.428*	2.658
<75	NA	2.655

Table 3. Bulk density and particle density of four rock samples

Sample ID	Granular size (μm)	Particle density (g/cm^3)	Bulk density (g/cm^3)			Difference (%)	
			DryFlo 38N	Quartz powder 38N	Quartz powder 46N	Quartz-DryFlo	Quartz powder 38N-46N
WFD-4-6L	2360-8000	2.642±0.001	2.490±0.001	2.389±0.024	NA	-4.06	NA
	1700-2360	2.642±0.002	2.543±0.033	2.539±0.056	2.325±0.025	-0.16	-8.43
	841-1700	2.638±0.001	2.327±0.030	2.490±0.074	2.458±0.042	-1.05	-1.29
	500-850	2.640±0.000		2.410±0.058	2.444±0.018		1.41
	177-500	2.643±0.001	NA	2.359±0.015	2.410±0.008	NA	2.16
	75-177	2.645±0.000		2.363±0.045	2.362±0.015		-0.04
WFD-9	2360-8000	2.150±0.001	1.85±0.014	1.703±0.040	NA	-7.95	NA
	1700-2360	2.139±0.001	1.766±0.007	1.686±0.010	1.661±0.026	-5.83	-1.48
	841-1700	2.138±0.004	1.628±0.006	1.700±0.015	1.668±0.035	4.42	-1.88
	500-850	2.135±0.002		1.615±0.003	1.579±0.033		-2.23
	177-500	2.120±0.001	NA	1.610±0.008	1.589±0.001	NA	-1.30
	75-177	2.111±0.001		1.437±0.004	1.404±0.022		-2.30
Paluxy Sandstone	2360-8000	2.718±0.003	2.425±0.014	2.435±0.013	NA	0.41	NA
	1700-2360	2.728±0.000	2.304±0.059	2.349±0.078	2.370±0.092	1.95	0.89
	841-1700	2.725±0.001	2.298±0.027	2.352±0.043	2.272±0.011	-0.08	-3.40
	500-850	2.733±0.001		2.383±0.006	2.397±0.034		0.59
	177-500	2.740±0.001	NA	2.291±0.026	2.284±0.115	NA	-0.31
	75-177	2.746±0.013		2.632±0.033	2.852±0.091		8.36
Austin Chalk	2360-8000	2.696±0.001	1.825±0.017	1.810±0.037	NA	-0.82	NA
	1700-2360	2.726±0.001	1.761±0.003	1.783±0.008	1.728±0.016	1.25	-3.08
	841-1700	2.729±0.001	1.723±0.024	1.768±0.037	1.838±0.013	2.61	3.96
	500-850	2.724±0.001		1.783±0.016	1.809±0.003		1.46
	177-500	2.721±0.001	NA	1.768±0.008	1.760±0.083	NA	-0.45
	75-177	2.727±0.001		1.801±0.008	2.211±0.019		22.77

3.1. Sampling bias

Powder (< 75 μm) of four samples were saved but not involved in density measurements. Because there is no proper method to measure the bulk density on such small sized granular samples. Sampling bias could exist due to the crushing and different sieved fractions. Kuila and Prasad (2013) and Adesida (2011) point out that crushing and sieving may change pore structure and introducing sampling bias in nitrogen adsorption. Their data shows that the pore volume increases with granular sizes decrease. We use this sampling bias to prove that the pore structure changes by crushing and sieving could also affect the porosity. However, nitrogen adsorption can only be applied on pores smaller than 300 nm and cannot provide the changes in porosity. In

the following sections, the porosity changes in different granular sizes by crushing and sieving will be discussed.

Table 4. DryFlo-derived bulk density results for different-sized steel balls and granular quartz

Sample	Steel ball 2 mm		Steel ball 1 mm		Quartz 2360-8000 μm		Quartz 1700-2360 μm		Quartz 850-1700 μm	
Preparation cycle	5	10	5	10	5	10	5	10	5	10
Bulk density g/cm³	7.726	7.757	7.097	7.043	2.608	2.548	2.512	2.546	2.476	2.444
Difference (%)	0.40		-0.76		-2.32		1.34		-1.33	

3.2. Accuracy of the GP method

From the GP Operator Manual (Micromeritics, 2017), the reproducibility of the DryFlo method could reach ±1.1% with the optimal control of parameters, including sample mass, preparation cycles, and consolidation force. Two preparation cycles are recommended by the Operator Manual. In this study, we mostly used five, because the measured volume shows a better stability with five preparation cycles, and 10 preparation cycles were also tested as a comparison. The default consolidation force is 38 N, and four samples under 46 N were also tested because the increased consolidation force may affect the final density results. Tables 3 and 4 show that the increased consolidation force (from 38 N to 45 N) and preparation cycles (from five to ten) affected the bulk density results by less than ±10%. In this study, the data for rocks were measured with optimum settings of sample mass (e.g., with a volumetric ratio between 0.6 to 0.8 for sample to DryFlo/quartz powder), five preparation cycles and 38 N consolidation force.

However, the DryFlo method can only apply to three out of six sizes (2360-8000 μm, 1700-2360 μm, and 850-1700 μm), because of DryFlo's relatively large sizes (~200 μm). The results for small-sized samples (<850 μm) by DryFlo envelopment are unreliable. As shown in Table 2, the bulk densities of crushed quartz (<850 μm)

measured by DryFlo are much smaller than 2.650 g/cm^3, which is unreasonable; the reason lies in the unaccounted TPPV, the impact of which becomes apparent when the sample and DryFlo sizes become similar. For sample sizes less than 850 μm, the DryFlo particles could not thoroughly wrap the sample surface and the TPPV cannot be offset in blank and sample measurements. The excess TPPV will be counted as part of the bulk volume of the sample, and the measured bulk density will be less than the actual value.

Table 3 shows the densities of four rock samples measured by DryFlo and quartz powder. The bulk density differences between the DryFlo and quartz-powder methods are expressed as the percentage difference (Equation 3).

$$\text{Percentage difference} = (\rho_{b\text{-qtz powder}} - \rho_{b\text{-DryFlo}})/\ \rho_{b\text{-DryFlo}} \qquad (3)$$

For the granular size 2360-8000 μm, the percent difference is relatively large, compared with other sizes. This may be because, without the graphic lubricant in quartz powder, the greater total surface area of size 2360-8000 μm associated with the angular shape of quartz-powder particles increases the surface friction. This increased friction prevents the free movement of quartz powder and the sample during compression. Unexpected large PPV could exist due to the incomplete wrapping and so the final bulk volume will be greater than the value by DryFlo, and the bulk density will be lower. For other (smaller) sizes, the friction is not as much as that for size 2360-8000 μm. The low percentage differences prove the credibility of the modified GP quartz-powder method (Table 3). We believe that the results from sizes smaller than 850 μm are also credible, for the changing bulk density as shown with MIP approach, which can measure both bulk and particle densities in a single run, has been demonstrated for a Wolfcamp shale sample (Hu, 2018). Though the quartz-powder particles are not as spherical and smooth as the DryFlo, the smaller size and the TPPV calibration give

credible density results. The repeatability and reproducibility, shown statistically, of the quartz-powder method could reach 3.63% and 0.66% for a total of 360 measurements, respectively (Table 5). We have also tested two smaller quartz granular sizes of 40-75 μm and <20 μm as the quartz standards. The results are not as good as these for the <75 μm granular size, probably because relatively poorly-sorted grains can have a lower and more consistent PPV and the compressed volume of quartz <20 μm was unstable, which made the bulk density inaccurate.

Table 5. Repeatability-equipment variation (EV) and reproducibility-appraiser variation (AV) of the DryFlo and quartz-powder methods; both EV and AV are calculated by following the work of Vardeman (2014)

Sample ID	WFD-4-6L		WFD-9		Paluxy Sandstone		Austin Chalk	
EV & AV	EV %	AV %	EV %	AV %	EV %	AV %	EV %	AV %
By DryFlow	0.90	1.11	0.32	0.61	0.47	0.60	0.25	0.31
By Quartz powder	4.93	0	2.89	0	4.13	1.27	3.25	0.49

3.3. Porosity of four rock samples

The bulk densities applied for porosity calculation were acquired by the combination of DryFlo and quartz-powder methods. Granular samples greater than 850 μm were measured by the DryFlo method, and samples between 75 μm and 850 μm were measured by the quartz-powder method. The results for the four rock samples show two different patterns in their porosities as a function of granular sizes (Fig. 4). Woodford Shales and Paluxy Sandstone (before reaching its primary grain size) samples show an increase in porosity with decreasing granular size, while Austin Chalk exhibits a much smaller relative porosity change. In Woodford Shale samples, compared with WFD-4-6L, WFD-9 shows a dramatic porosity increase in 75-177 μm and a lower isolated pore percentage (Table 6). The crushing at small granular sizes in WFD-9 may expose/connect the isolated pores and increase the measured porosity, as

shown from the measured low values of bulk density. However, this increase does not occur in WFD-4-6L. With its lower presence of isolated pores (Table 6), the pore connectivity in WFD-9 is better than WFD-4-6L, and therefore the porosity increase for 75-177 μm size is dramatic in WFD-9. We expect that such porosity increase will be evident in sample sizes less than 75-177 μm for WFD-4-6L, if such an analysis could have been experimentally performed.

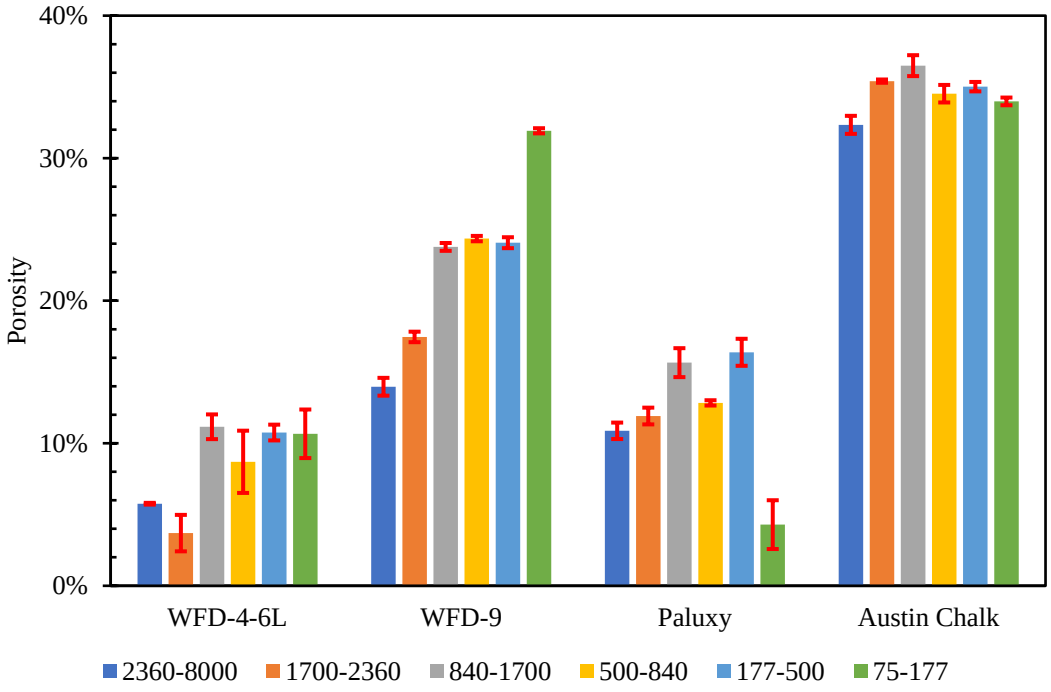

Figure 22. Porosities of four rock samples with six granular sizes; the measurement for bulk density of each size/sample was performed in triplicate, from which the error bar shown on the figure was calculated

Comparing with the porosity of core plugs and cubes, the porosities and isolated pore percentage of granular crushed samples of WFD-4-6L and WFD-9 show an increase with the decreasing granular size even though the increase was not obvious for WFD-4-6L at the granular range of 75-177 μm (Table 6) with the statistical analyses (Table 2). The largely increased porosity for WFD-4-6L could have been noticed at sample sizes smaller than 75-177 μm, but this is not easily achievable with available methodologies in the scientific community, even with the small angle neutron and x-ray scattering (Zhang et al., 2019).

Table 6. Porosity and isolated pore percentage* in the WFD shale samples for 1-inch dia. core plug, 1-cm3 cube, and granular size at 2360-8000 μm

Granular sample size (μm)	1-in dia. plug	1-cm^3 cube	2360-8000	1700-2360	841-1700	500-841	177-500	75-177
Porosity (%)	0.7±0.003	2.0±0.011	5.8±0.001	3.7±0.013	11.2±0.011	8.7±0.022	10.8±0.006	10.7±0.017
WFD-4-6L isolated pore percentage (%)	by plug	66.9	87.1	79.8	93.3	91.4	93.1	93.0
		by cube	65.2	45.8	82.0	77.0	81.4	81.2
			by 2360-8000	-55.8	48.4	33.8	46.4	46.0
Granular sample size (μm)	1-in dia. plug	1-cm^3 cube	2360-8000	1700-2360	841-1700	500-841	177-500	75-177
Porosity (%)	9.6±0.004	12.5±0.004	14.0±0.006	17.5±0.004	23.8±0.003	24.4±0.002	24.1±0.004	31.9±0.002
WFD-9 isolated pore percentage (%)	by plug	23.0	31.0	44.8	59.5	60.4	60.0	69.8
		by cube	10.4	28.4	47.4	48.7	48.0	60.8
			by 2360-8000	20.0	41.3	42.7	42.0	56.3

The porosity of Paluxy Sandstone shows a slight increase, but more likely stable values considering the measurement reproductivity, from size of 2360-8000 μm to size of 177-500 μm, and then shows a sudden drop at size 75-177 μm (Fig. 4). This porosity drop could be related to the primary grain sizes of the Paluxy Sandstone. A total of 430 grains were point-counted and measured by ImageJ on BSE2 images (Fig. 5). The grain size of Paluxy Sandstone is found to be 148±57 μm within the range from 11 μm to 373 μm. In Fig. 6, some sand grains in Paluxy Sandstone are disaggregated and become isolated non-porous sand grains (indicated by black arrows), which decreases the porosity. For 75-177 μm sample, this size is comparable to the primary grain sizes with negligible porosity, and hence a reduced porosity from a smaller volume of inter-granular pore space. In other words, when all sand grains are fully disaggregated, the measured bulk density will be close to particle density, with porosity approaching to zero; this is the case for the solid quartz used in this work.

The relative porosity changes with grain size in the Austin Chalk are minor compared with other three rock samples. This result agrees with the porosity results from calcarenitic carbonate rock reported by Vik et al. (2013), namely that the

petrophysical property fluctuation is less with the existence of the representative elementary volume (REV), the smallest volume over which a measurement can be made that will yield a value representative of the whole sample. The REV and pore connectivity with different granular sizes will be discussed in the following part. In Table 7, the P-value of analysis of variance (ANOVA) in evaluating the porosity difference among four granular sizes from 75-1700 μm for Austin Chalk is greater than 0.1, which indicate that the pore connectivity is the same in all six granular sizes. In other words, the Austin Chalk with well-connected pore space is relatively homogeneous compared with other three samples and has likely entered the REV regime in this sample size. The sample size scale for REV concept is 177-1700 μm for the Paluxy Sandstone, and the gradual increase of porosity for larger sizes of 1700-8000 μm could be related to the liberation of some isolated pores, as shown from the abundant presence of cementing materials (Fig. 5) which can lead to the poorly connected pore space (Hu et al., 2012). For organic-rich and fine-grained shale, the validity of REV is debatable, while two zones of connectivity are suggested (Hu et al., 2015; Hu, 2018). For both WFD-4-6L and WFD-9, two larger-sized grains (1700-8000 μm) shows a gradual increase of porosity with the associated liberation of isolated pores, corresponding to the extent of pore connectivity for the bulk zone. On the other hand, the surface zone behavior is evident for WFD-9 at 75-177 μm size, while not shown yet for WFD-4-6L in this smallest tested sample size.

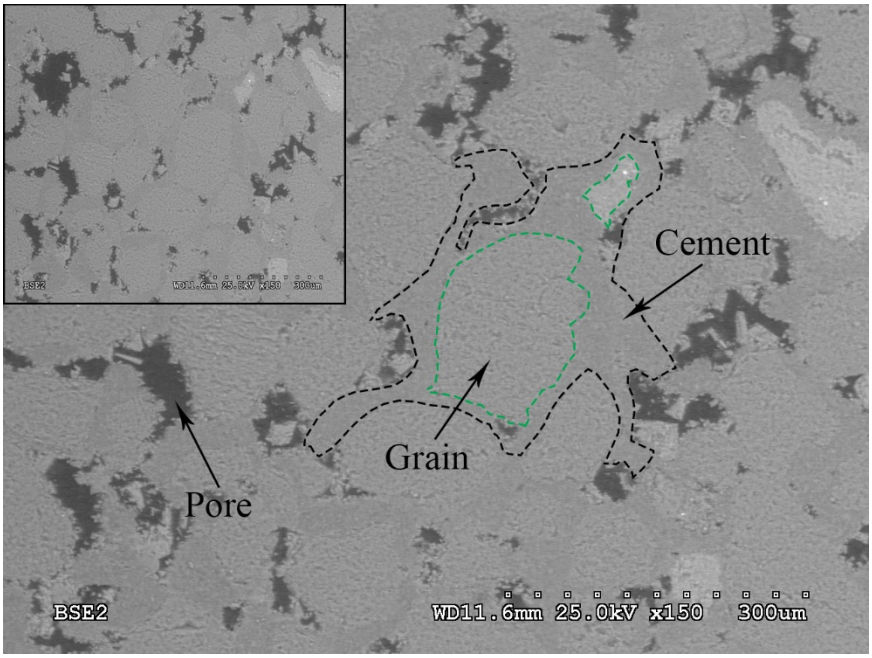

Figure 5. BSE2 image of the Paluxy Sandstone.

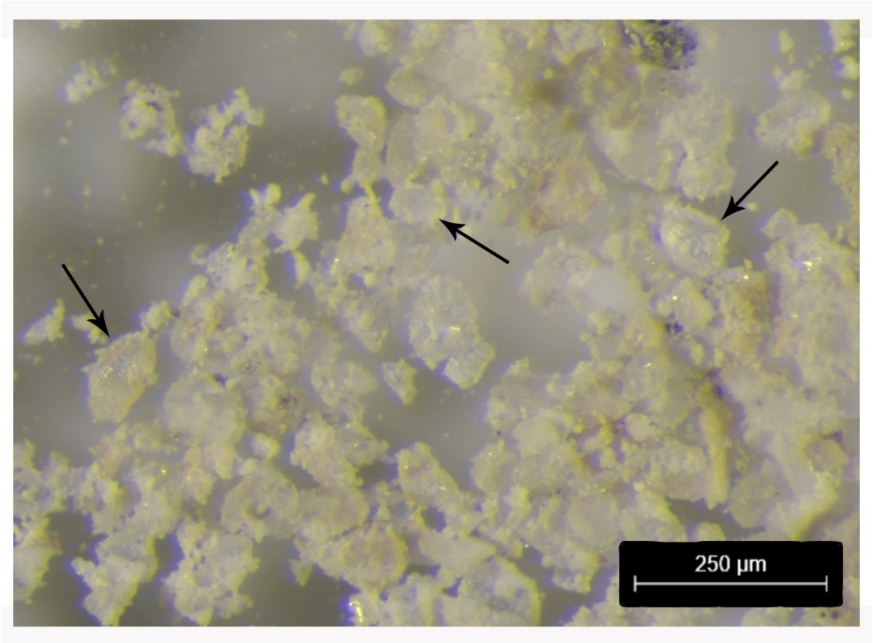

Figure 6. Paluxy sandstone at a granular size of 75-177 µm.

Table 9. P-value of analysis of variance (ANOVA; St and Wold, 1989) of porosity in crushed-rock samples

Granular size (μm)	2360-8000	1700-2360	841-1700	500-850	177-500	75-177
WFD-4-6L	←		3.38×10^{-4}			→
			←	0.30		→
WFD-9	←		7.90×10^{-14}			→
			←	0.22	→	
Paluxy Sandstone	←		4.20×10^{-7}			→
	←		6.61×10^{-5}		→	
			←	0.01	→	
Austin Chalk	←		6.66×10^{-5}			→
	←	8.06×10^{-4}	→			
				←	0.13	→

4. Conclusions

The porosity values for a range of different-sized granular crushed-rock samples were calculated from experimentally measured particle densities (by helium pycnometry) and a modified bulk density GeoPyc 1365 method on shale, sandstone, and chalk. The bulk density method was modified by using quartz powder (<75 μm) instead of the original larger-sized DryFlo, combined with total packing pore volume calibrations for each granular size, which extends the measurable sample size range from 850-8000 μm to 75-8000 μm. The bulk density data measured by GeoPyc 1365 using the combined DryFlo and quartz-powder methods exhibit high repeatability and reproducibility. From the porosity pattern of four samples in six granular sizes, the opening of isolated pores could be the reason for porosity increase in tight shale samples, while a decrease in the smallest size fraction is related to the relatively larger primary grain sizes of the Paluxy Sandstone. With this method improvement, the effective porosity for smaller granular sizes can be measured, which helps the scientific community to learn more about the pore systems and assess the REV. There are still limitations to this modified bulk density measurement, as it can only be applied to granular sizes greater than 75 μm.

Though the repeatability and reproducibility of quartz-powder method are acceptable, the accuracy of this modified method cannot yet support quantitative analysis in porosity studies but can provide a qualitative and semi-quantitative assessment of porosity change and isolated pore percentage in granular samples.

Acknowledgment

Financial assistance for this work was provided by the National Science and Technology Major Project of China (No. 2016ZX05034-002-006). We would like to thank the late Roger Slatt, and Jing Zhang, at the University of Oklahoma for their assistance in the sample collection of Woodford Shales.

References

API RP40. (1998). Recommended Practices for Core Analysis. Recommended Practice 40, Second Edition, American Petroleum Institute, 236 pp.

Acevedo, D., Muliadi, A., Giridhar, A., Litster, J. D., & Romañach, R. J. (2012). Evaluation of three approaches for real-time monitoring of roller compaction with near-infrared spectroscopy. AAPS PharmSciTech, 13(3), 1005-1012.

Adesida, A., 2011, Pore size distribution of Barnett Shale using nitrogen adsorption data: M.S. thesis, University of Oklahoma.

Beard, D. C., & Weyl, P. K. (1973). Influence of texture on porosity and permeability of unconsolidated sand. AAPG bulletin, 57(2), 349-369.

Bi, M., Alvarez-Nunez, F., & Alvarez, F. (2014). Evaluating and modifying Johanson's rolling model to improve its predictability. Journal of Pharmaceutical Sciences, 103(7), 2062-2071.

Busch, A., Schweinar, K., Kampman, N., Coorn, A., Pipich, V., Feoktystov, A., Leu, L., Amann-Hildenbrand, A. and Bertier, P. (2017). Determining the porosity of mudrocks using methodological pluralism. Geological Society, London, Special Publications, 454(1), 15-38.

Chen, Y., Qin, Y., Wei, C., Huang, L., Shi, Q., Wu, C., & Zhang, X. (2018). Porosity changes in progressively pulverized anthracite subsamples: Implications for the study of closed pore distribution in coals. Fuel, 225, 612-622.

Danielson, R. E., & Sutherland, P. L. (1986). Porosity. Methods of Soil Analysis: Part 1 Physical and Mineralogical Methods, 5, 443-461.

Davudov, D., Moghanloo, R. G. (2016). Upscaling of pore connectivity results from lab-scale to well-scale for Barnett and Haynesville Shale Plays. In SPE Annual Technical Conference and Exhibition. Society of Petroleum Engineers.

Flint, A. L., Flint, L. E. (2002). Particle Density. Methods of Soil Analysis: Part 4 Physical Methods, 5, 229-240, Soil Science Society of America, Madison, WI.

Forsmo, S. P. E., & Vuori, J. P. (2005). The determination of porosity in iron ore green pellets by packing in silica sand. Powder technology, 159(2), 71-77. Freeman, V. L. (1961). Contact of Boquillas flags and Austin chalk in Val Verde and Terrell counties, Texas. AAPG Bulletin, 45(1), 105-107.

Fu, Y., Jiang, Y., Wang, Z., Hu, Q., Xie, J., Ni, G., Lei, Z., Zhou, K. and Liu, X. (2019). Non-connected pores of the Longmaxi shale in southern Sichuan Basin of China. Marine and Petroleum Geology, 110, 420-433.

Gaus, G., Kalmykov, A., Krooss, B. M., & Fink, R. (2020). Experimental investigation of the dependence of accessible porosity and methane sorption capacity of carbonaceous shales on particle size. Geofluids, 2020.

Hearn, N., & Hooton, R. D. (1992). Sample mass and dimension effects on mercury

intrusion porosimetry results. Cement and Concrete Research, 22(5), 970-980.

Hu, Q. H. (2018). Quantifying effective porosity of oil and gas reservoirs. AAPG Search and Discovery Article #70376, 5 pages. DOI:10.1306/70376Hu2018.

Hu, Q. H., Ewing, R. P., & Dultz, S. (2012). Low pore connectivity in natural rock. Journal of Contaminant Hydrology, 133: 76–83.

Hu, Q. H., Ewing, R. P., & Rowe, H. D. (2015). Low nanopore connectivity limits gas production in Barnett Formation. Journal of Geophysical Research – Solid Earth, 120(12): 8073–8087.

Hu, Q. H., Zhang, Y. X., Meng, X. H., Li, Z., Xie, Z. H., & Li, M. W. (2017). Characterization of multiple micro-nano pore networks in shale oil reservoirs of Paleogene Shahejie Formation in Dongying Sag of Bohai Bay Basin, East China. Petroleum Exploration and Development, 44(5): 720–730.

Jones, R. M. (2003). Particle size analysis by laser diffraction: ISO 13320, standard operating procedures, and Mie theory. American Laboratory (Fairfield), 35(1), 44-47.

Klaja, J., Łykowska, G., & Przelaskowska, A. (2015). Helium porosity measurements for rocks from unconventional reservoirs performed on crushed samples. Nafta-Gaz, 71(11), 856-863.

Kuila, U., & Prasad, M. (2013). Application of nitrogen gas-adsorption technique for characterization of pore structure of mudrocks. The Leading Edge, 32(12), 1478-1485.

Kuila, U., McCarty, D. K., Derkowski, A., Fischer, T. B., & Prasad, M. (2014). Total porosity measurement in gas shales by the water immersion porosimetry (WIP) method. Fuel, 117, 1115-1129.

Micromeritics Instrument Inc. (2014). AccuPyc II 1340 Operator Manual, 254 pp.

Micromeritics Instrument Inc. (2017). GeoPyc 1365 Operator Manual, 92 pp.

Patel, N., R. A. Brooks, M. T. Clarke, P. M. T. Lee, N. Rushton, Iain Ronald Gibson, S. M. Best, and W. Bonfield. (2005). In vivo assessment of hydroxyapatite and silicate-substituted hydroxyapatite granules using an ovine defect model. Journal of Materials Science: Materials in Medicine, 16(5), 429-440.

Radlinski, A.P., Mastalerz, M., Hinde, A.L., Hainbuchner, M., Rauch, H., Baron, M., Lin, J.S., Fan, L. and Thiyagarajan, P. (2004). Application of SAXS and SANS in evaluation of porosity, pore size distribution and surface area of coal. International Journal of Coal Geology, 59(3-4), 245-271.

Rogers, J. J., & Head, W. B. (1961). Relationships between porosity, median size, and sorting coefficients of synthetic sands. Journal of Sedimentary Research, 31(3), 467-470.

Schneider, C. A., Rasband, W. S., & Eliceiri, K. W. (2012). NIH Image to ImageJ: 25 years of image analysis. Nature Methods, 9(7): 671-675.

St, L., & Wold, S. (1989). Analysis of variance (ANOVA). Chemometrics and Intelligent Laboratory Systems, 6(4), 259-272.

Stojanović, Z. S., Marković, S., & Uskoković, D. (2012). Determination of particle size distributions by laser diffraction. Technics–New Materials (Special Edition), 11-20.

Sun, J., Dong, X., Wang, J., Schmitt, D. R., Xu, C., Mohammed, T., & Chen, D. (2016). Measurement of total porosity for gas shales by gas injection porosimetry (GIP) method. Fuel, 186, 694-707.

Trippetta, F., Ruggieri, R., Brandano, M., & Giorgetti, C. (2020). Petrophysical properties of heavy oil-bearing carbonate rocks and their implications on petroleum system evolution: Insights from the Majella Massif. Marine and

Petroleum Geology, 111, 350-362.

Vardeman, S. B. (2014). Gauge Repeatability and Reproducibility (R & R) Studies. Wiley StatsRef: Statistics Reference Online.

Vernon-Parry, K. D. (2000). Scanning electron microscopy: an introduction. III-Vs Review, 13(4), 40-44.

Vik, B., Bastesen, E., & Skauge, A. (2013). Evaluation of representative elementary volume for a vuggy carbonate rock—Part: Porosity, permeability, and dispersivity. Journal of Petroleum Science and Engineering, 112, 36-47.

Webb, P. A. (2001). Volume and density determinations for particle technologists. Micromeritics Instrument Corp., 2(16), 01.

Yang, R., He, S., Hu, Q., Sun, M., Hu, D., & Yi, J. (2017). Applying SANS technique to characterize nano-scale pore structure of Longmaxi shale, Sichuan Basin (China). Fuel, 197, 91-99.

Zhang, Y. X., Hu, Q. H., Long, S. X., Zhao, J. H., Peng, N. J., Wang, H. T., Lin, X., & Sun, M. D. (2019). Mineral-controlled nm-μm-scale pore structure of saline lacustrine shale in Qianjiang Depression, Jianghan Basin, China. Marine and Petroleum Geology, 99: 347–354.

Zhang, Y. X., Hu, Q. H., Barber, T. J., Bleuel, M. K., Anovitz, L., & Littrell, K. (2020). Quantifying fluid-wettable effective pore space in the Utica and Bakken oil shale Formations. Geophysical Research Letters, 47, e2020GL087896.

Chapter V: Conclusions

In this dissertation, multiple approaches to petrophysical characterization were applied on Woodford Shale outcrop samples and Wolfcamp Shale well core samples to better understand how sedimentology and mineralogy affect the shale pore structure. Using the multiple-approach methodology, the aims of this dissertation research are to: 1) compare the application of several approaches, 2) find relationships between grain size, mineral composition, and pore structure; 3) and characterize the heterogeneity of the shale rocks. The results indicate that depositional processes and mineralogical composition could largely affect the pore structures and fluid-rock interactions of shale.

The results from Chapter II indicate that the dominance of slit-shaped macropores and mesopores in Woodford Shale outcrop samples. By performing the spontaneous imbibition, the Woodford Shale is intermediate to good connectivity towards DIW with a wettability characteristics of intermediate mixed-wet and intermediate water-wet. The natural weathering could dissolve minerals and cements to create macropores and increase the porosities. By comparing and integrating the pore structure results from all four approaches, the MIP method of fluid intrusion approach has outstanding advantages in pore structure characterization. With supporting information from GP and SEM, the combination of MIP, GP, and SEM could be a good experimental combination for pore structure characterization. The (U)SAXS could also provide information for nanopores if it is available.

Chapter III is a case study by using multiple approaches to examine 13 well core samples of Wolfcamp Shale. The results indicate that the slit-shape and wedge-shape in the ranges of mesopores in macropores are the major pore geometry. Through SEM imaging, “sandwich” structure composed by clay and quartz or feldspar control the pore shape and pore size, regardless of grain sizes. The “sandwich” structure and layered

structure could be inherited from the deposition of a hemiplegic environment. Porosity increases as quartz and feldspar content increases, and organic matters in Wolfcamp Shale are in oil window which is a good indication of hydrocarbon generation.

Chapter IV uses a modified GeoPyc 1365 bulk density technique to study the porosities of granular Woodford Shale samples. By using quartz powder (< 75 μm) as the media in bulk density analyzer, the measurable sample size range is extended from 850-8000 μm to 75-8000 μm. The bulk densities measured by quartz powder method and the DryFlo method show a high repeatability and reproducibility. The varying porosities of sandstone, shale, and chalk with sample sizes indicate that the opening of isolated pores could increase the porosity for smaller sized granular shale samples.

In summary, shale pore structures could be largely affected by mesopores which have close relationships with mineralogy and grain spacial relationships. The increase in “quartz + feldspar” content could increase the mesopores volume, and the increase in cement could decrease the mesopores volume. The layered structure or “sandwich” structure with quartz, feldspar, and clay, which inherited from deposition could help in forming mesopore which could contribute to the pore volume and pore surface area. The grain size has less effect on pore structure compared to mineralogy and grain assemblages. Heterogenity of the pore structures with different sample dimentions is also shown by the data from all three projects, which could affect the experimental selections and data interpretations.